

THE MAGNETIC AND CHEMICAL STRUCTURAL  
PROPERTY OF THE EPITAXIALLY-GROWN  
MULTILAYERED THIN FILM

by

HWACHOL LEE

GARY J. MANKEY, COMMITTEE CHAIR  
PATRICK R. LECLAIR  
JAMES W. HARRELL  
ARUNAVA GUPTA  
RICHARD H. TIPPING

A DISSERTATION

Submitted in partial fulfillment of the requirements  
for the degree of Doctor of Philosophy  
in the Department of Physics & Astronomy  
in the Graduate School of  
The University of Alabama

TUSCALOOSA, ALABAMA

2012

Copyright Hwachol Lee 2012  
ALL RIGHTS RESERVED

## ABSTRACT

$L1_0$  FePt- and Fe-related alloys such as FePtRh, FeRh and FeRhPd have been studied for the high magnetocrystalline anisotropy and magnetic phase transition property for the future application. In this work, the thin film structural and magnetic property is investigated for the selected FePtRh and FeRhPd alloys. The compositionally-modulated  $L1_0$  FePtRh multilayered structure is grown epitaxially on a-plane  $\alpha$ - $Al_2O_3$  with Cr and Pt buffer layer at 600°C growth temperature by DC sputtering technique and examined for the structural, interfacial and magnetic property. For the epitaxially grown  $L1_0$  [ $Fe_{50}Pt_{45}Rh_5$  (FM) (10nm) /  $Fe_{50}Pt_{25}Rh_{25}$  (AFM) (20nm)] $\times 8$  superlattice, the magnetically and chemically sharp interface formation between layers was observed in X-ray diffraction, transmission electron microscopy and polarized neutron reflectivity measurements with the negligible exchange bias at room and a slight coupling effect at lower temperature regime.

For FeRhPd, the magnetic phase transition of epitaxially-grown 111-oriented  $Fe_{46}Rh_{48}Pd_6$  thin film is studied. The applied Rhodium buffer layer on a-plane  $\alpha$ - $Al_2O_3$  (11 $\bar{2}$ 0) at 600°C shows the extraordinarily high quality of epitaxial film in (111) orientation, where two broad and coherent peak in rocking curve, and Laue oscillations are observed. The epitaxially-grown Pd-doped FeRh on Pt (111) grown at 600°C, 700°C exhibits the co-existing stable  $L1_0$  (111) and B2 (110) structures and magnetic phase transition around 300°C. On the other hand, the partially-ordered FeRhPd structure grown at 400°C, 500°C shows background high ferromagnetic state over 5K~350K temperature. For the reduced thickness of  $Fe_{46}Rh_{48}Pd_6$ , the ferromagnetic state becomes dominant with a reduced portion of the film undergoing a magnetic phase transition.

For some epitaxial FeRhPd film, the spin-glass-like disordered state is also observed in field dependent SQUID measurement. For the tri-layered FeRhPd with thin Pt spacer, the background ferromagnetic state is significantly reduced and spin-glass-like state also disappears. In polarized neutron reflectivity, magnetic depth profiles of tri-layered FeRhPd reveals the asymmetric magnetization between two FeRhPd layers. The asymmetric magnetic profile of FeRhPd tri-layered structure is closely related to the thickness dependent epitaxial film growth of B2 structure.

## DEDICATION

This dissertation is dedicated to all people who have been with me throughout my Ph.D years, in particular, my mother Heungnyun Jung, my father Kyounggho Lee in heaven, my brother, Jongsun Lee, and all colleagues and friends who support me to continue the research on Physics throughout the time.

## LIST OF ABBREVIATIONS AND SYMBOLS

<i>AFM</i>	Antiferromagnet
<i>BF</i>	Bright field
<i>FIB</i>	Focused ion beam
<i>FM</i>	Ferromagnet
<i>FWHM</i>	Full width of half maximum
<i>HAADF</i>	High angle annular dark field
<i>MAGIC</i>	Magnetic Advanced Grazing Incidence Spectrometer
<i>MPMS</i>	Magnetic property measurement system
<i>PNR</i>	Polarized neutron reflectivity
<i>QED</i>	Quantum electrodynamics
<i>RF</i>	Radio frequency
<i>RGA</i>	Residual gas analyzer
<i>SLD</i>	Scattering length density
<i>SQUID</i>	Superconducting quantum interference device
<i>STEM</i>	Scanning transmission electron microscopy
<i>TEM</i>	Transmission electron microscopy
<i>UHV</i>	Ultra high vacuum
<i>XRD</i>	X-ray diffraction
<i>XRR</i>	X-ray reflectivity

*VSM*

Vibrating sample magnetometer

## ACKNOWLEDGMENTS

I am really pleased to have an opportunity to thank all people who were involved in my Ph.D years. Physics is the great meaning of my life and I am really grateful for a given opportunity in the University of Alabama.

First, I would like to thank all professors and faculty members in the department of Physics and Center for Materials for Information Technology for their direct or indirect help for my Ph.D years. Especially, I would like to thank my research advisor, Dr. Gary J. Mankey for his great guidance and help to continue and finish my Ph.D research. I am highly influenced by his enthusiasm, dedication and openness to science. Also, I would like to thank Dr. Patrick R. LeClair for his great advice and support for all my Ph.D years. I have been motivated by his occasional encouragement, advice and concern. I would like to thank Dr. James W. Harrell for his earlier guidance and concern of my Ph.D years. I would like to thank Dr. Hideo Fujiwara for his great discussion and advice during my Ph.D years. I would like to thank Dr. William H. Butler, Dr. Arunava Gupta, Dr. Subhadra Gupta, Dr. Yang-Ki Hong, Dr. William D. Doyle for their educational support, help and advice throughout my Ph.D years. I would like to thank Dr. Tim Mewes for my earlier experimental experience. In my Ph.D years, most of work has been done with the great collaboration with my colleagues. In the early experience of epitaxial film growth and X-ray characterization, I am indebted to Dr. Hideo Sato (in Tohoku University) for his great help and advice. I would like to thank Dr. Dipanjan Mazumdar for the help of SQUID measurement. I would like to thank Rob Holler for XRD, XPS training. Also, I would like to thank Jian Yu, Dr. Manjit Pathak (at Western digital), Dr. Zeenath Reddy Tadisina (at Intel),

Neha Pachauri, Sahar Keshavarz for their help and great collaboration during my entire Ph.D years. For the neutron experiments, I would like to thank Dr. Valeria Lauter and Dr. Hailemariam Ambaye for a nice discussion and helpful advice of the polarized neutron reflectivity experiment. Also, I would like to thank Dr. Dieter Lott and Jochen Fenske (at GKSS in Germany) for the nice collaboration for neutron experiment. I would like to thank Physics machine shop people Joe Howell, David Key, Danny Whitcomb (for electronics) for the help of the building, modification and troubleshooting of the lab setup. Also, I would like to thank MINT office staffs, Jamie Crawford, Carrie Martin, Casey McDow, Tabatha Jarnagin, John Hawkins (for lab work), Jason Foster (for computer work) for their support for the research.

Also, I would like to thank all my Korean friends, Dr. Donghyun Kim (in Northwestern University), Guihan Ko (in Temple University), Kyoungwoo Lee (in Korea), Dr. Younghwan Park (in Yeungnam University), Dongyop O (in UA), Gunwoo Kim (in UA), Dr. Gihan Kwon (in Argonne National Laboratory) for their encouragement and support.

The author gratefully acknowledges financial support from US-DOE award DE-FG02-08ER46499.

This research at Oak Ridge National Laboratory Spallation Neutron Source was sponsored by the Scientific User Facilities Division, Office of Basic Energy Sciences, U.S. Department of Energy.

## CONTENTS

ABSTRACT.....	ii
DEDICATION.....	iv
LIST OF ABBREVIATIONS AND SYMBOLS .....	v
ACKNOWLEDGMENTS .....	vii
LIST OF TABLES.....	xi
LIST OF FIGURES .....	xii
I. INTRODUCTION .....	1
II. EXPERIMENTAL TECHNIQUE.....	9
A. Magnetron sputtering technique.....	9
1. Thin film growth on the substrate.....	11
2. Epitaxial film growth.....	11
3. Vacuum system.....	12
B. Quantum design magnetic property measurement system.....	19
C. Transmission electron microscopy.....	23
III. X-RAY AND NEUTRON SCATTERING TECHNIQUE .....	26
A. X-ray and polarized neutron reflectivity for thin film.....	30

B.	Polarized neutron reflectometry .....	38
C.	X-ray diffraction.....	42
1.	High angle X-ray diffraction .....	42
2.	Rocking curve scan.....	44
3.	Pole figure measurement .....	47
IV.	FePtRh MULTILAYER SYSTEM.....	49
A.	Sample preparation.....	49
B.	X-ray characterization of FePtRh single - and bi-layered samples .....	51
C.	The epitaxial relation between FePtRh, Cr, Pt and Al <sub>2</sub> O <sub>3</sub> .....	54
D.	X-ray diffraction for superlattice samples.....	56
E.	Magnetic property of FePtRh superlattice structure .....	60
V.	FePhPd MULTILAYERED SYSTEM.....	65
A.	EXPERIMENTAL DETAILS.....	65
B.	RESULTS AND DISCUSSION .....	67
1.	Rh seed layer growth and characterization.....	67
2.	Single layer FeRhPd .....	75
3.	Trilayer FeRhPd .....	91
4.	Polarized neutron reflectivity .....	98
VI.	CONCLUSION.....	104
	REFERENCES .....	106

## LIST OF TABLES

Table I Scattering angle for each FeRhPd peak identified by Gaussian fitting of X-ray diffraction results and the calculated lattice constants for the centered tetragonal (CT) and B2. Each scattering angle and the corresponding calculated lattice constant are labeled with the same subscript number.....	80
---	----

## LIST OF FIGURES

FIG. 1 The magnetic phase diagram of (a) $\text{FePt}_x\text{Rh}_{1-x}$ with respect to Pt composition $x$ and temperature and (b) $\text{FeRh}_{1-x}\text{Pd}_x$ with respect to Pd composition $x$ and temperature (adapted from the reference [3, 11] .....	2
FIG. 2 The simplified schematic of the compositionally modulated multilayer system. To clarify the compositional difference, only Rh atom is designated in orange color. The slight different lattice spacing between $\text{Fe}_{50}\text{Pt}_{45}\text{Rh}_5$ and $\text{Fe}_{50}\text{Pt}_{45}\text{Rh}_5$ and any possible interface property is abbreviated for simplicity. ....	3
FIG. 3 The atomic structural arrangement (a) $L1_0 \text{Fe}_{50}\text{Pt}_{45}\text{Rh}_5$ , (b) $L1_0 \text{Fe}_{50}\text{Pt}_{25}\text{Rh}_{25}$ , and (c) $B2 \text{Fe}_{46}\text{Rh}_{48}\text{Pd}_6$ structure in $3 \times 3 \times 3$ atomic size, where each colored sphere represents the corresponding atom :white –Fe, green-Pt, blue –Rh, red– Pd. ....	5
FIG. 4 The schematic of DC magnetron sputtering technique. ....	10
FIG. 5 The schematic of ADAM sputtering chamber.....	13
FIG. 6 The schematic of RASCAL sputtering chamber. ....	14
FIG. 7 The mass spectrum of the unbaked vacuum chamber. ....	16
FIG. 8 The mass spectrum of the baked vacuum chamber. ....	17
FIG. 9 Pressure versus time graph during degassing of the chamber inside at $700^\circ\text{C}$ . ....	18
FIG. 10 MPMS SQUID system schematics of sample position (adapted from reference [44])... ..	20
FIG. 11 MPMS detection system schematics (adapted from reference [44]).....	21
FIG. 12 The schematic of transmission electron microscopy equipment (adapted from the reference [47] .....	24
FIG. 13 (a) Feynman diagram of elastic scattering of free electron and photon (b) the schematic of scattering of an incident particle by one atom and (c) by crystal .....	29
FIG. 14 Scattering case for the semi-infinite plane. $k_1$ and $k_2$ is the wavenumber at each medium. ....	33

FIG. 15 Scattering case at three (n-1)th,(n)th and ( n+1)th layers in the multilayered structure. The arrows in the figure indicate the transmitting and reflected wave direction with the wavenumber $k_{n-1}$ , $k_n$ , $k_{n+1}$ . $d$ is the thickness of the (n)th layer and $R_n$ , $R_{n-1}$ represent the reflectance at each boundary.....	34
FIG. 16 The diagram of the Parratt recursive relation for the reflectivity of the multilayered structure.....	37
FIG. 17 The schematic of the Spallation Neutron Source facility in Oak Ridge National Laboratory (adapted from the reference [61]) .....	40
FIG. 18 The schematic of the polarized neutron reflectometry setup in the beam line.....	41
FIG. 19 The schematic of the X-ray diffraction Philips setup.....	45
FIG. 20 The schematic of the rocking curve scan. The X-ray source and detector is placed on the XY plane. ....	46
FIG. 21 The schematic of the X-ray setup for pole figure measurement. The dotted line indicates the rotational axis of the sample. While X-ray source and detector is placed on the XY plane, the sample plane is tilted at $\psi$ angle from Z-axis. ....	48
FIG. 22 XRD result for (a) $\text{Fe}_{50}\text{Pt}_{45}\text{Rh}_5$ (10nm)/ $\text{Fe}_{50}\text{Pt}_{25}\text{Rh}_{25}$ (20nm) bilayer, (b) $\text{Fe}_{50}\text{Pt}_{45}\text{Rh}_5$ (50nm), (c) $\text{Fe}_{50}\text{Pt}_{25}\text{Rh}_{25}$ (50nm) single layered samples. The dotted line indicates the common peak observed for Pt(111), Cr(110), $\alpha\text{-Al}_2\text{O}_3$ (1120) and $\alpha\text{-Al}_2\text{O}_3$ (2240) from the common seed layer and the substrate. In (a), two (111) peaks from $\text{Fe}_{50}\text{Pt}_{45}\text{Rh}_5$ (10nm) and $\text{Fe}_{50}\text{Pt}_{25}\text{Rh}_{25}$ (20nm) appears as merged due to the close peak position.....	50
FIG. 23 Rocking curve scan for (111) peak of (a) $\text{Fe}_{50}\text{Pt}_{45}\text{Rh}_5$ (50nm) and (b) $\text{Fe}_{50}\text{Pt}_{25}\text{Rh}_{25}$ (50nm) sample. The full width of half maximum (FWHM) is indicated in the figure.....	52
FIG. 24 The pole figure scan results for (111) of (a) $\text{Fe}_{50}\text{Pt}_{45}\text{Rh}_5$ (50nm) and (b) $\text{Fe}_{50}\text{Pt}_{25}\text{Rh}_{25}$ (50nm) sample. The $\alpha\text{-Al}_2\text{O}_3$ (1120) measured at the tilted angle $\psi=60^\circ$ are plotted together in the red line.....	53
FIG. 25 The diagram for the lattice spacing of the plane of each layer (a) $L1_0$ FePtRh, (b) Pt (111), (c) Cr (110) and (d) $\alpha\text{-Al}_2\text{O}_3$ (1120) plane. ....	55
FIG. 26 The $\theta$ - $2\theta$ scan results around FePtRh 111 position for superlattice [ $\text{Fe}_{50}\text{Pt}_{45}\text{Rh}_5$ (10nm)/ $\text{Fe}_{50}\text{Pt}_{25}\text{Rh}_{25}$ (20nm)] $\times 8$ sample.....	57
FIG. 27 Transmission electron microscopy image for superlattice FePtRh sample measured by HAADF.....	59
FIG. 28 SQUID result for superlattice [ $\text{Fe}_{50}\text{Pt}_{45}\text{Rh}_5$ (10nm)/ $\text{Fe}_{50}\text{Pt}_{25}\text{Rh}_{25}$ (20nm)] $\times 8$ sample measured at 5K, 150K, 300K.....	62

FIG. 29 The polarized neutron reflectivity of $[\text{Fe}_{50}\text{Pt}_{45}\text{Rh}_5 (10\text{nm})/\text{Fe}_{50}\text{Pt}_{25}\text{Rh}_{25} (20\text{nm})] \times 8$ measured at 250K with 1.15T applied field during field cooling for two spin channels.....	63
FIG. 30 Scattering length density obtained from the fitting of the polarized neutron reflectivity of FePtRh superlattice structure for two spin channels.....	64
FIG. 31 X-ray diffraction $\theta$ - $2\theta$ scan for Rh(20nm) grown on m-plane $\alpha\text{-Al}_2\text{O}_3$ (1010), c-plane $\alpha\text{-Al}_2\text{O}_3$ (0001), and a-plane $\alpha\text{-Al}_2\text{O}_3$ (1120) substrate at 600°C.....	68
FIG. 32 X-ray reflectivity of Rh (20nm) on (1) m-plane $\alpha\text{-Al}_2\text{O}_3$ (0001) grown at 600°C (2) c-plane $\alpha\text{-Al}_2\text{O}_3$ (0001) grown at 600°C , (3) on a-plane $\alpha\text{-Al}_2\text{O}_3$ (1120) grown at 600°C and (4) 500°C .....	70
FIG. 33 The pole figure of Rh (20nm) sample grown on (a) a-plane and (b) c-plane $\alpha\text{-Al}_2\text{O}_3$ . Each peak is measured in the azimuthal angle scan for Rh (111) and $\text{Al}_2\text{O}_3$ (a) (1120), (b) (1012) at the tilted angle $\psi$ with respect to the perpendicular direction to the film plane as designated in the graph.....	72
FIG. 34 (a) X-ray diffraction (plotted in logarithmic scale) and (b) off-specular (rocking curve) scan result for Rh(111) of Rh (20nm) on (1) a-plane $\alpha\text{-Al}_2\text{O}_3$ (1120) and (2) c-plane $\alpha\text{-Al}_2\text{O}_3$ (0001) planes grown at 600°C. The dotted blue line in (b) is the integrated fitting line by two Gaussians (red and orange line).....	74
FIG. 35 (a) Off-specular (rocking curve) scan result for Rh(111) of Rh (20nm, 40nm, 80nm) on a-plane $\alpha\text{-Al}_2\text{O}_3$ (1120) grown at 600°C (X-ray source : $\text{Cu K}\alpha_{1,2}$ ) and (b) full width of half maximum of the broad peak in figure (a) with respect to Rh film thickness.....	76
FIG. 36 X-ray diffraction $\theta$ - $2\theta$ scan for FeRhPd(50nm) films on Pt(10nm) /Rh(10nm) / a-plane $\alpha\text{-Al}_2\text{O}_3$ (1120) substrate with Pt(6nm) capping grown at 400°C, 500°C, 600°C, 700°C. Each plot is shifted to clarify each diffraction pattern. The inset inside the figure shows the linear-scale plot of each diffraction peak at 83°~95° angle.....	78
FIG. 37 X-ray diffraction $\theta$ - $2\theta$ scan for FeRhPd (10nm, 20nm, 30nm, 40nm, 50nm) films on Pt(10nm) / Rh (10nm) on a-plane $\alpha\text{-Al}_2\text{O}_3$ (1120) substrate grown at 600°C. All samples are capped with Pt (6nm). Each plot is shifted in intensity to clarify each diffraction pattern. The inset inside the figure shows the linear-scale plot of each diffraction peak at 83°~95° angle. ....	82
FIG. 38 The integrated B2, B2'(220) peak area of XRD result (FIG. 37) plotted with respect to the thickness of FeRhPd. The total is the sum of the integrated B2 and B2' peak area. ....	83
FIG. 39 SQUID measurement result of magnetization M versus temperature T for FeRhPd (50nm) films grown at 400°C, 500°C, 600°C, 700°C. 1T external magnetic field is applied during the measurement.....	85

FIG. 40 SQUID measurement result of magnetization  $M$  versus temperature  $T$  for FeRhPd (50nm, 30nm, 10nm) grown at 600°C. The small arrow designates the heating and cooling direction. 1T external magnetic field is applied during the measurement. .... 87

FIG. 41 SQUID measurement results re-plotted in the smaller scales of magnetization for FeRhPd (50nm) films grown at 400°C, 500°C, 600°C, 700°C. In the figure, ZFC represents the zero field cooling and FC, 1T field cooling. The freezing temperature ( $T_f$ ) is indicated with arrows. .... 89

FIG. 42 SQUID measurement results re-plotted in the smaller scales of magnetization for FeRhPd (30nm, 10nm) and [FeRhPd(25nm)/ Pt(0.5nm)/ FeRhPd(25nm)] tri-layered film. In the figure, ZFC represents the zero field cooling and FC, 1T field cooling. .... 90

FIG. 43 X-ray diffraction  $\theta$ - $2\theta$  scan for FeRhPd (25nm) / Pt (0.5nm) / FeRhPd (25nm) films on Pt (10nm) / Rh (10nm) / a-plane  $\alpha$ -Al<sub>2</sub>O<sub>3</sub> (1120) substrate grown at 600°C with Pt (6nm) capping layer. The inset in (a) shows the linear plot of the diffraction peak at the angle 83~95° ..... 92

FIG. 44 X-ray reflectivity and fitting (red line) results for FeRhPd (25nm) / Pt (0.5nm) / FeRhPd (25nm) films on Pt (10nm) / Rh (10nm) / a-plane  $\alpha$ -Al<sub>2</sub>O<sub>3</sub> (1120) substrate grown at 600°C with Pt (6nm) capping layer. .... 93

FIG. 45 (a) pole figure measured for  $\alpha$ -Al<sub>2</sub>O<sub>3</sub>(1120) at the tilted angle 60° and Pt (111), FeRhPd (111) at the tilted angle 70.5°, (b) rocking curve measured for FeRhPd (111), FeRhPd (110). In (a), each pole figure of Pt and FeRhPd is shifted by 10 counts per second for clarity. .... 94

FIG. 46 The magnetization hysteresis loop of FeRhPd tri-layered sample measured by VSM. . 96

FIG. 47 SQUID measurement results of [FeRhPd(25nm)/ Pt(0.5nm)/ FeRhPd(25nm)] tri-layered film plotted with FeRhPd (50nm, 30nm) previous results for comparison. During the measurement, 1T external magnetic field is applied. .... 97

FIG. 48 PNR (left) measured for non-spinflip channels at 450K, 350K, 300K, 5K with 1T applied field along the cooling and its scattering length density depth profile (right) obtained from fitting by Parratt recursion relation. .... 101

FIG. 49 PNR (left) measured for non-spinflip channels at 350K with 1T, 0.005T applied field along the heating and its scattering length density depth profile (right) obtained from fitting by Parratt recursion relation. The inset (right) is the linear plot of PNR around the critical scattering vector. .... 102

## I. INTRODUCTION

Recently, the magnetic phase changing property of B2 structured FeRh, or  $L1_0$  FePtRh materials has been studied for a possible technical application – such as thermally-assisted recording media [1, 2]. The magnetic phase changing property of FePtRh in a bulk scale is already well-known that it depends on the compositional modulation of Pt and Rh [3].

FIG. 1 (a) shows the magnetic phase diagram of the FePtRh with respect to the composition and temperature. The  $FePt_xRh_{1-x}$  has the B2 and  $L1_0$  structure with respect to Pt composition where  $x < 0.17$  for B2 and  $L1_0$  structure for  $x > 0.17$ . The recent structural study of FePtRh thin film revealed the spin configuration of atoms at each magnetic state at different temperatures [4]. In spite of the recent numerous experimental results [4-6], many thin film properties such as the interface property, or exchange bias in the multilayered system has not been examined yet. In addition, temperature dependent property of magnetic materials is also expected to be of concern in the future spintronics and recording media [7-10]. Previously, (001)-oriented FePtRh thick film (100 nm) has been grown and studied for the structural and magnetic phase property with respect to temperature. In thin film state, one concern is the growth mechanism on the different epitaxial orientation. In the epitaxial film growth, the orientation plays a crucial role in the formation of the epitaxial film structure due to the layer-by-layer growth mode mechanism and the energetic preference with respect to the orientation. In this work,  $L1_0$  FePtRh thin film is investigated for new (111) orientation on Pt seed layer. In thin film application, the magnetic property is mainly concerned in the multilayered structure.

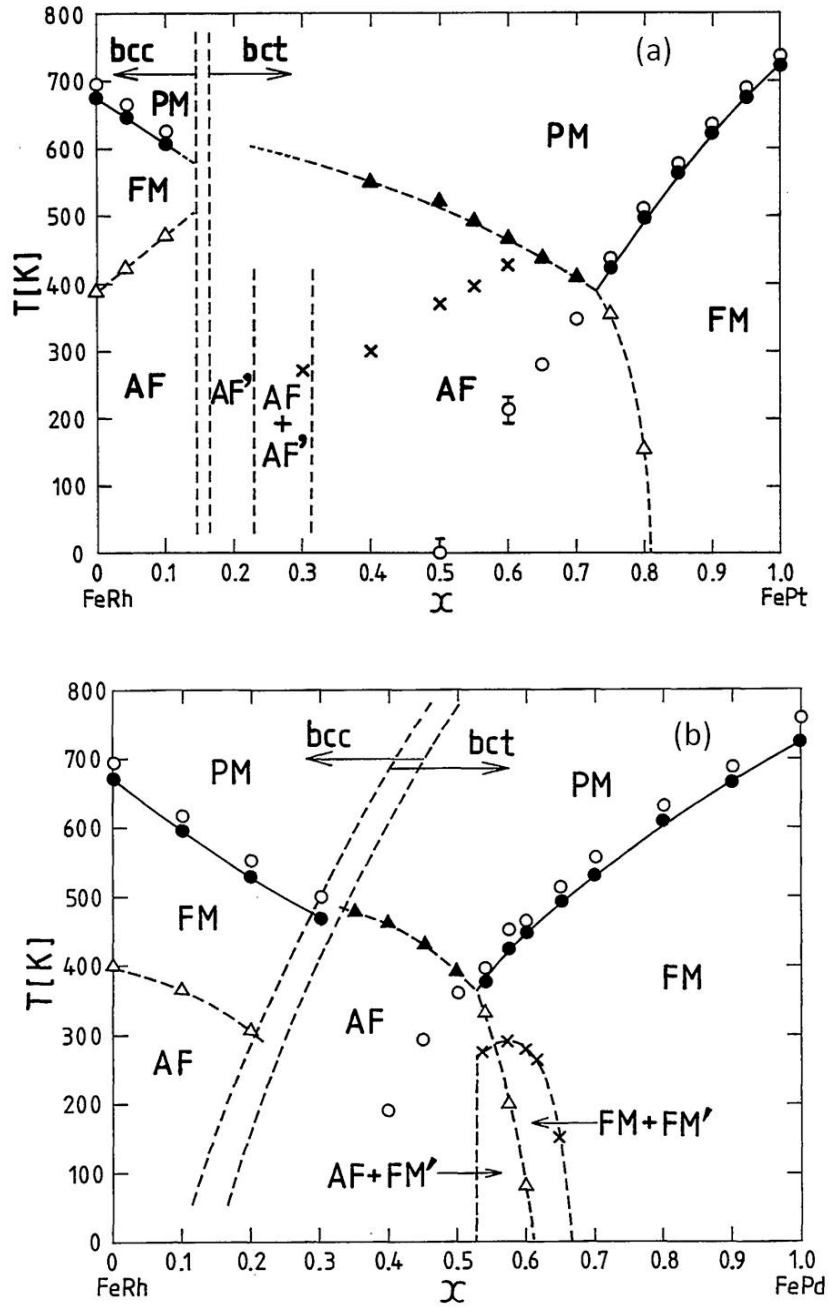


FIG. 1 The magnetic phase diagram of (a)  $\text{FePt}_x\text{Rh}_{1-x}$  with respect to Pt composition  $x$  and temperature and (b)  $\text{FeRh}_{1-x}\text{Pd}_x$  with respect to Pd composition  $x$  and temperature (adapted from the reference [3, 11])

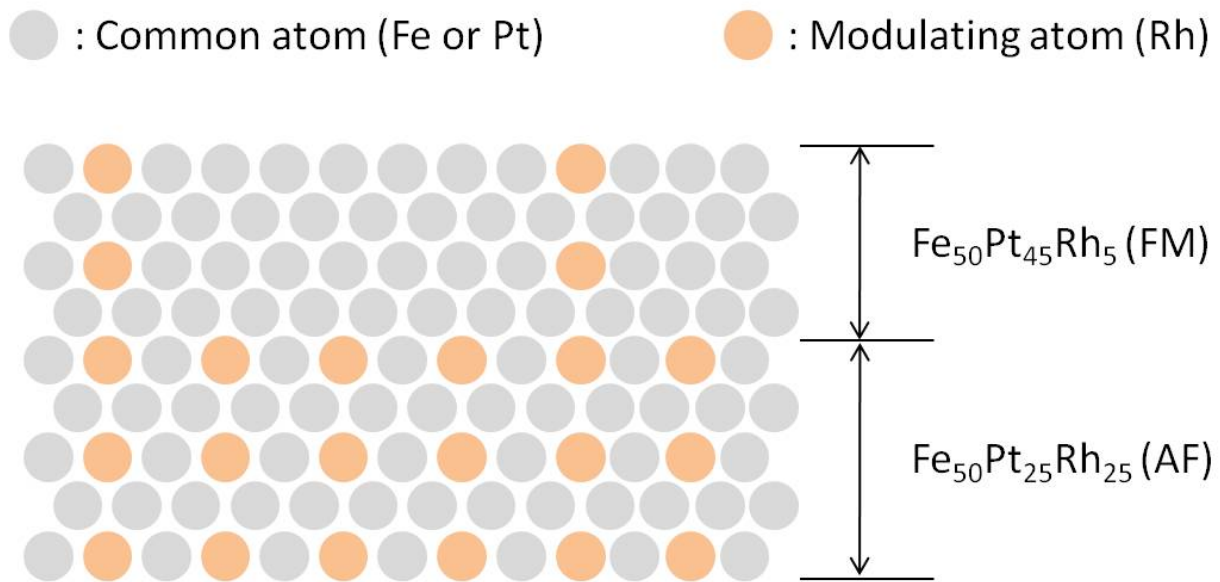


FIG. 2 The simplified schematic of the compositionally modulated multilayer system. To clarify the compositional difference, only Rh atom is designated in orange color. The slight different lattice spacing between  $\text{Fe}_{50}\text{Pt}_{45}\text{Rh}_5$  and  $\text{Fe}_{50}\text{Pt}_{25}\text{Rh}_{25}$  and any possible interface property is abbreviated for simplicity.

As studied in the bulk material state, the introduction of more elements cause slight lattice spacing change and different magnetic phase depending on the composition. In the growth of the multilayered structure, it is realized here that one kind of FePtRh system can be applied in the formation of the magnetically different multilayered structure. For example, ferromagnet (FM) / antiferromagnet (AFM) bilayered structure can be achieved from a single FePtRh alloy by changing the relative composition slightly. In other words, the different magnetic phase – ferromagnetic or, antiferromagnetic phase can be selected from the commonly structured FePtRh alloy system and stacked in the magnetic multilayered structure such as FM / AFM. The advantage of the selection of the magnetic phase from the same material system is the structural similarity which results in the least lattice mismatch between layers. The schematic of FePtRh FM / AFM bilayer system is described in FIG. 2. In this experiment, two FePtRh compositions,  $\text{Fe}_{50}\text{Pt}_{45}\text{Rh}_5$  for ferromagnet and  $\text{Fe}_{50}\text{Pt}_{25}\text{Rh}_{25}$  for antiferromagnet are selected which is known stable in bulk scale at room temperature, respectively [3].  $L1_0$  atomic structure for each FePtRh composition is also shown in FIG. 3 (a) and (b). In  $L1_0$  FePtRh structure, Fe atoms are positioned at the right position and some Pt atoms are replaced by doped Rh atoms with respect to the doping composition. When two different  $L1_0$  FePtRh are used in the construction of the bilayered structure as in FIG. 2, the expected difference between two compositional layers is only the number of Rh atoms (orange-colored spheres in the FIG. 2) placed at Pt atomic site with almost the same structure and lattice spacing. In the growth of such a multilayered structure, one concern is the interface property between two (FM and AFM) layers. The structural similarity between layers may result in the significantly diffusive or, highly intermixed state at the interface.

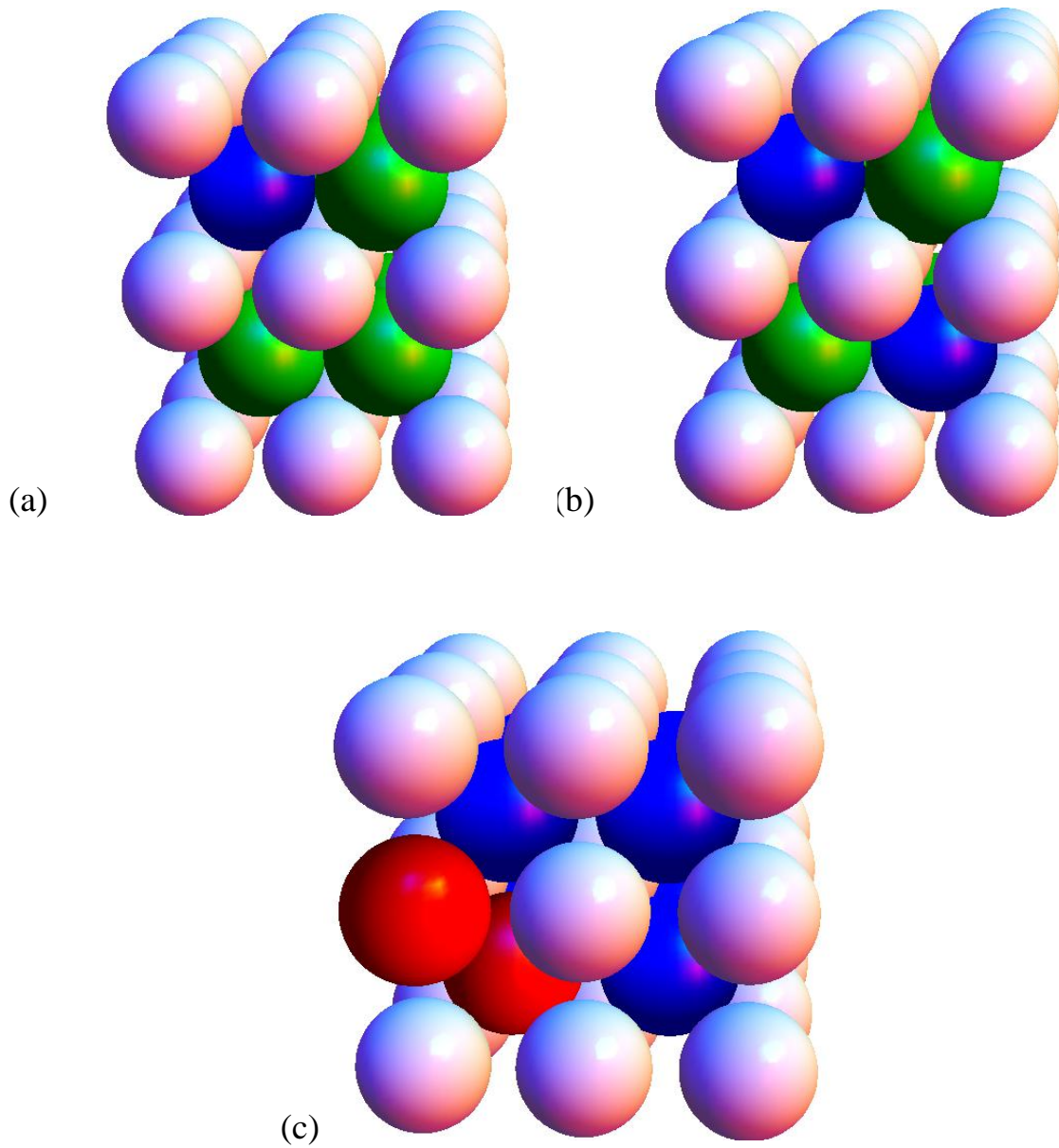


FIG. 3 The atomic structural arrangement (a)  $L1_0$   $Fe_{50}Pt_{45}Rh_5$ , (b)  $L1_0$   $Fe_{50}Pt_{25}Rh_{25}$ , and (c)  $B2$   $Fe_{46}Rh_{48}Pd_6$  structure in  $3 \times 3 \times 3$  atomic size, where each colored sphere represents the corresponding atom :white –Fe, green-Pt, blue –Rh, red– Pd.

To investigate the interface property of the system, FM / AFM repeated superlattice structure is grown and examined for the chemical structural and magnetic property by several techniques. The fundamental structural and magnetic properties between ferromagnet  $\text{Fe}_{50}\text{Pt}_{45}\text{Rh}_5$  and antiferromagnet  $\text{Fe}_{50}\text{Pt}_{25}\text{Rh}_{25}$  in superlattice structure is investigated by X-ray diffraction (XRD), transmission electron microscopy (TEM) and polarized neutron reflectometry (PNR). The static magnetic property of the superlattice with respect to the temperature is examined by superconducting quantum interference device (SQUID) magnetometer. In another perspective of the phase diagram of FePtRh or FeRhPd in the FIG. 1, it is noticed that the slight doping with third element (Pt for FePtRh, Pd for FeRhPd) near  $\text{Fe}_{50}\text{Rh}_{50}$  composition shows the modified magnetic phase transition behavior with respect to temperature. The magnetic phase transition phenomenon has been of great concern due to its possible application of the thermally assisted magnetic recording media, or energy related applications such as magnetic refrigerator which is operated by the magnetocaloric effect [12-14]. Especially, FeRh alloy system has been known for its interesting features - ultrafast magnetic phase switching, first order magnetic phase transition above room temperature, the largest magnetocaloric effect [15-18]. Recently, more attempts have been made in search of the possible application in spintronics [19, 20]. FeRh has a compositionally sensitive magnetic phase around the stoichiometric composition where highly ordered B2 structure ( $\alpha'$  phase) has the first order antiferro-ferromagnetic transition above room temperature. In FeRh, the Fe-rich composition has a single  $\alpha'$  phase with Fe composition 0.51 to 0.59 at.% while Fe-deficient composition ranging from 0.41 to 0.51 at.% shows the coexisting  $\alpha'$  + metastable  $\gamma$  phase [21]. In the modification of FeRh magnetic transition property, it has been realized that doping of FeRh with a third element stabilizes the magnetic phase and also shifts the magnetic phase transition temperature below room temperature, which enables low

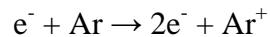
temperature research on the magnetic phase transition phenomena [16]. Pd-doped FeRh has the centered tetragonal structure of CuAu-type ( $L1_0$ ) and CsCl BCC (B2) structure with respect to the compositional ratio between Fe, Rh, and Pd and temperature [11, 22]. The main difference between  $L1_0$  and B2 structure is the elongated lattice spacing in one longitudinal direction in  $L1_0$  structure which results in the different stable magnetic states due to the change of magnetic coupling strength between the localized Fe magnetic moment. In B2 FeRh alloy case, it also has been revealed that the mediation of the induced magnetic moment of Rh atoms plays a crucial role in the formation of the magnetic stable states [23, 24]. For  $Fe_{46}(Rh_{0.89}Pd_{0.11})_{54}$ , the schematic of B2 structure is shown in the FIG. 3 (c) where the doped Pd atoms occupy Rh, or Fe atomic sites. A recent report on  $Fe_{49}(Rh_{0.93}Pd_{0.07})_{51}$  compound shows the field-induced magnetic phase and coexistence of antiferro-, ferro-magnetic phases at low temperatures [25]. In this work, we focus on the properties of Pd-doped FeRh thin film material. As noted in earlier FeRh research, FeRh thin films shows different magnetic phase transition properties from the bulk, such as the surface magnetic moment. In addition, strain at the interface becomes more important for the overall film property of the magnetic phase transition [21, 26-28]. For the compositional dependent feature, one concern of Fe-deficient FeRh alloy is the coexistence of  $\alpha'$ , metastable  $\gamma$  phase. Normally, the  $\gamma$  phase FeRh is not preferred due to its magnetic instability. Here, we dope Fe-deficient FeRh with Pd. Thus, the epitaxial thin film of  $Fe_{46}(Rh_{0.89}Pd_{0.11})_{54}$  composition is especially chosen and studied, here. For epitaxial film growth, the crystallographic orientation plays a crucial role in determining the structural and magnetic property. Most of the recent FeRh thin film research has been focused on acquiring the highly ordered B2 001-oriented FeRh thin film grown within the right composition range where the sharp and high meta-magnetic phase transition occurs, because the large off-stoichiometry, or

less ordered structure results in metastable  $\gamma$ -FeRh with a broadened magnetic phase transition. In this work, epitaxial  $\text{Fe}_{46}\text{Rh}_{48}\text{Pd}_6$  (just referred as FeRhPd in the later discussion) thin films are grown on the highly (111)-oriented Pt seed layer. To induce (111)-oriented epitaxial thin film growth, a rhodium thin layer on a-plane  $\alpha\text{-Al}_2\text{O}_3$  (11 $\bar{2}$ 0) substrate is applied. For the high quality of epitaxial film growth, many materials such as platinum or niobium has been reported for the good epitaxial relation with sapphire substrate and applied to many thin film research, until now [29-36]. In this work, we report the highly-matched epitaxial Rhodium thin layer on sapphire substrate. As will be discussed later, extraordinary (111)-oriented Rh on a-plane  $\alpha\text{-Al}_2\text{O}_3$  (11 $\bar{2}$ 0) and c-plane  $\alpha\text{-Al}_2\text{O}_3$  (0001) is achieved. In thin film structures, another concern is the magnetic exchange coupling effect between magnetic layers. Because of the possible applications, there have been many researches on magnetic coupling effects in bi-layered structures composed of two different kinds of magnetic layers [12, 37]. Here, in addition to the thickness dependent property of FeRhPd, we study FeRhPd epitaxial layers separated by a non-magnetic Pt spacer. The insertion of a very thin Pt spacer layer provides the coupling between two separate FeRhPd layers. In FeRh thin film case, it has been realized that the magnetic phase transition begins at the film surface and propagates towards the remaining part in the nucleation and growth mode [26, 38]. The revealed existence of the surface magnetic moment may play a crucial role of magnetic phase transition of thin film in the multilayered structure [27]. Based on the revealed mechanism and knowledge of magnetic phase transition, the coupled FeRhPd thin film layers are studied here. For all the prepared structures and films, the chemical, structural, and temperature-dependent magnetic properties are examined by X-ray diffraction, superconducting quantum interference device (SQUID). In addition, the polarized neutron reflectivity technique (PNR) is applied for the study of the magnetic depth profile of a trilayer structure.

## II. EXPERIMENTAL TECHNIQUE

### A. Magnetron sputtering technique

All metal thin film samples here are prepared by magnetron sputtering technique. The principle of the magnetron sputtering techniques is explained as below. In sputtering technique, thin metal films are grown inside the vacuum chamber where most of molecules at present in the air are removed. In deposition, the metals targets to deposit are positioned right on the opposite side of the substrate. When the inert Ar gas at a few millitorr pressure is introduced between two electrodes, a small number of electrons at the cathode are accelerated towards the anode. At a sufficient energy of the accelerated electrons, neutral Ar atoms are ionized by collision and the secondary electron is released.



The successive increase of the number of electrons enables the formation of the sustainable plasma. The steep potential difference between the cathode and the plasma in the sheath region accelerate the positively charged Ar ion to the cathode. At a sufficient energy attained, considerable amount of Ar ions impinge on the cathode and sputter the target materials on the cathode. The sputtered target material is finally deposited on the substrate located in the opposite side of the target. In DC magnetron sputtering, the magnetic field around the target is applied to confine the electrons movement around the cathode, which causes more efficient production of the plasma. The schematic of the sputtering is shown in the FIG. 4.

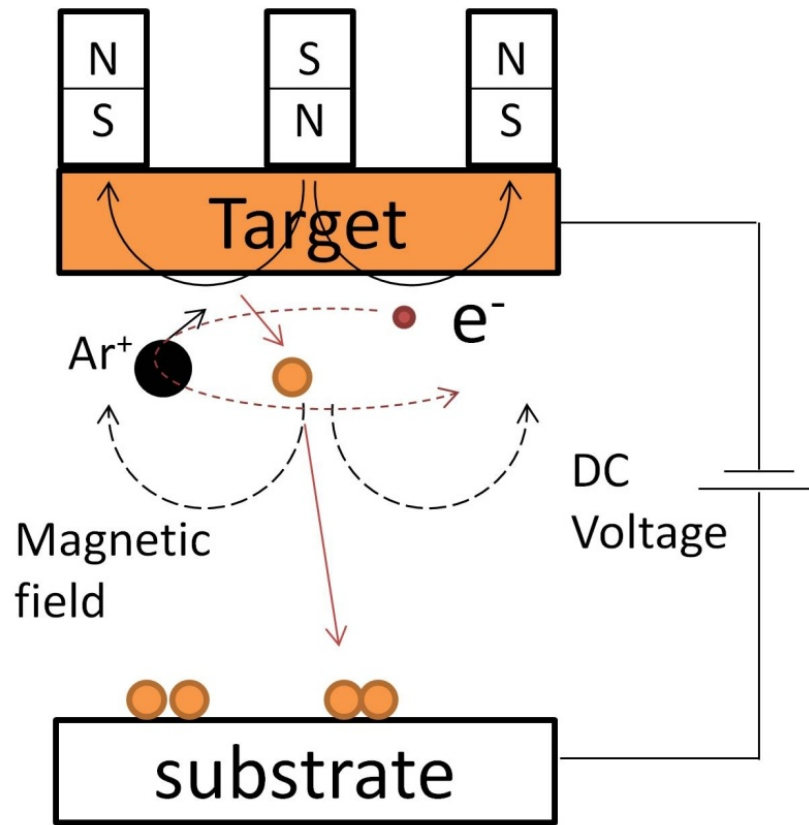


FIG. 4 The schematic of DC magnetron sputtering technique.

## 1. Thin film growth on the substrate

Thin film is grown on the substrate by DC magnetron sputtering technique.

Experimentally, it has been observed that the thin film grows on the substrate by nucleation and growth mode and can be explained by the basic three modes - island growth, layer-by-layer growth and island-layer growth modes. Theoretically, the characteristics of the growth mode have been considered with respect to the surface energy and kinetic process of the nucleation. In experiment, the growth mode of thin film on the substrate is mainly determined by substrate temperature and deposition rate. The basic understanding of the film morphology for sputtered thin film can be achieved by structure zone model by Thornton [39]. In this diagram, the morphology of thin film is determined by the substrate temperature, inert sputtering gas pressure [40-42].

## 2. Epitaxial film growth

For the epitaxial film growth by sputtering technique, the vacuum condition in the chamber plays an important role in addition to the previous thin film growth conditions. Especially, the contamination of the thin film is closely related to the process of the epitaxial film growth process – recrystallization and grain boundary migration by affecting the nucleation density of the deposited film [40]. The behavior of the gas molecules inside the chamber can be well understood by the kinematic theory of gas molecules at the atomic level. For the ideal gas molecules which obey the Maxwell-Boltzmann distribution, the contamination time  $t$  for the complete coverage of monolayer on the surface ( $10^{15}$  atoms/cm<sup>2</sup>) is given in the equation (1) as follows in the literature [42].

$$t = \frac{2.85 \times 10^{-8}}{P} (MT)^{1/2} \quad (1)$$

In equation (1), the time (t) is the second, M, the molecular weight, T, the absolute temperature (K) and P, the pressure (torr). According to the equation, the contamination time t in UHV condition is approximately several hours while the time is a few seconds at  $10^{-6}$  mbar [42]. In case that there exists large lattice mismatch and largely different thermal expansion between substrate and the film, the use of buffer layer can enhance the quality of the epitaxy [41].

### 3. Vacuum system

For the preparation of the thin film sample, two sputtering systems (ADAM, RASCAL) in Center for Materials for Information Technology (MINT), The University of Alabama are used. Each system is composed of several vacuum components as drawn in the FIG. 5 and FIG. 6. The ultra high vacuum (UHV) condition in the chamber is achieved by the rotary mechanical pump, turbo pump and cryopump. The rotary mechanical pump lowers the pressure down to  $10^{-2}$  mbar from atmosphere pressure. The turbo pump is used to reduce the pressure from  $10^{-2}$  to  $10^{-9}$  mbar. In turbo pump, the multi-bladed disks are rotated at the maximum rotational speed  $\sim 80,000$  rpm and removes molecules inside the chamber [43]. The turbopump and rotary vane pump is connected to the loadlock chamber in series and the chamber pressure is monitored by the thermocouple gauge and Bayard-Alpert gauge.

# ADAM sputtering chamber

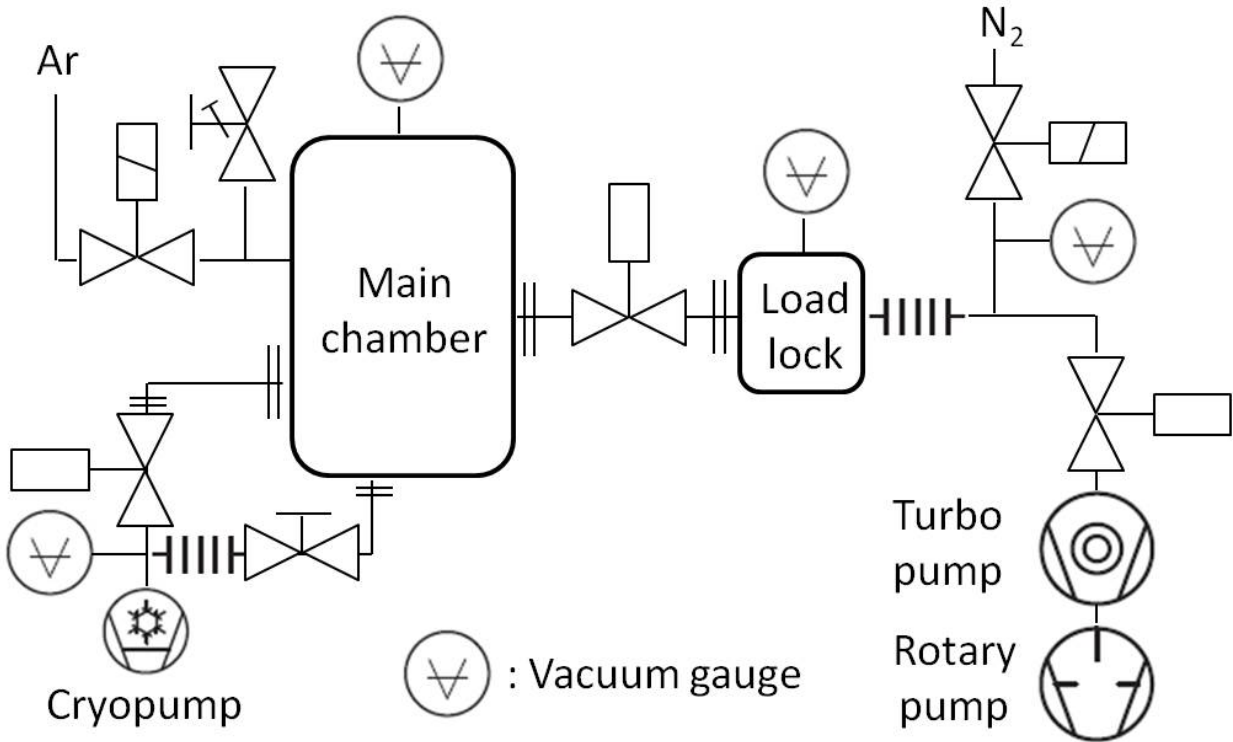


FIG. 5 The schematic of ADAM sputtering chamber.

## RASCAL sputtering chamber

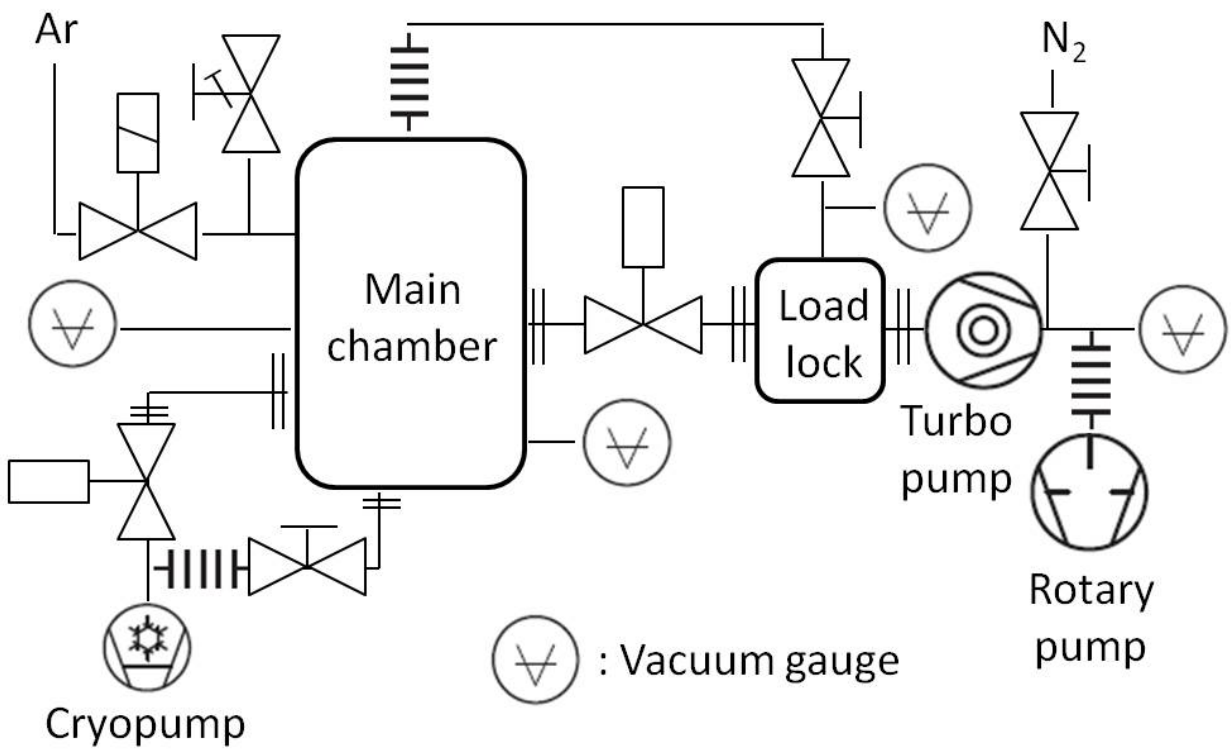


FIG. 6 The schematic of RASCAL sputtering chamber.

The load lock chamber which is used for the sample loading can be isolated from the main chamber by the pneumatically-controlled valve. The main chamber is directly connected to the cryopump with ion and thermocouple pressure gauge. Usually, the cryopump is operated within  $10^{-3}$ ~ $10^{-11}$  mbar range. At low temperature, the molecules in gas state are condensed due to Van der Waals force between molecules. From the inlet, hydrocarbon molecules, Ar, N<sub>2</sub>, O<sub>2</sub>, or most other molecules are condensed on the bare metal surface. The additional micro-porous charcoal in cryopump absorbs the additional light gases such as H<sub>2</sub>, He at 10-20K [43]. Under the high vacuum pressure, the vapor pressure (outgassing pressure) of metal is usually low with the exceptions for the high vapor pressure materials the such as Cd, Pb and Zn which is avoided in the initial vacuum system setting [43]. The permeated gases in the chamber are removed by the outgassing procedure - baking the chamber at around 150°C for 12 hours. FIG. 7 and FIG. 8 show the partial pressure versus mass spectrum of the unbaked and baked system measured by residual gas analyzer. In the unbaked case, the vacuum chamber contains various kinds of gases inside with a considerable partial pressure. After proper baking procedure, He, H<sub>2</sub>O, N<sub>2</sub>/CO, CO<sub>2</sub> gases are observed at the partial pressure less than  $2 \times 10^{-9}$  torr. In the actual sample deposition, it is necessary to heat the substrate inside the vacuum chamber for epitaxial film growth and the chamber inside is pre-heated for deposition. FIG. 9 shows the pressure change of the specific gases with respect to the heating time. As seen in the graph, mostly, H<sub>2</sub> gas pressure is increased dramatically due to its high permeability to the steel and titanium metals.

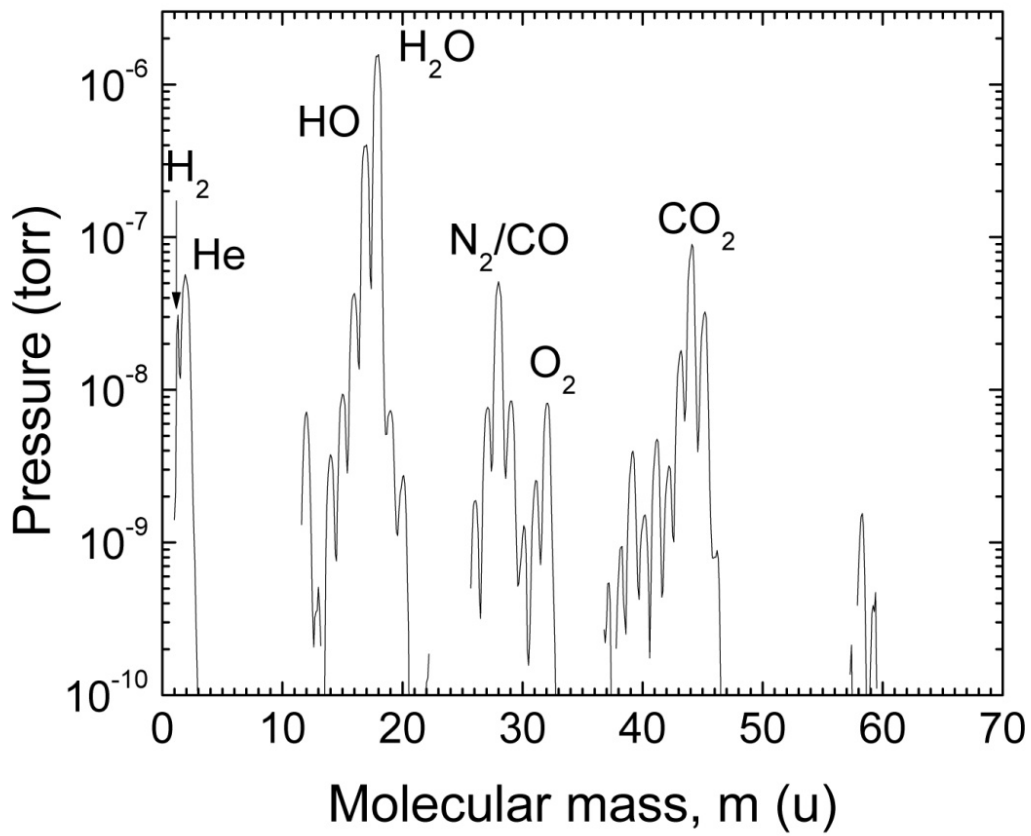


FIG. 7 The mass spectrum of the unbaked vacuum chamber.

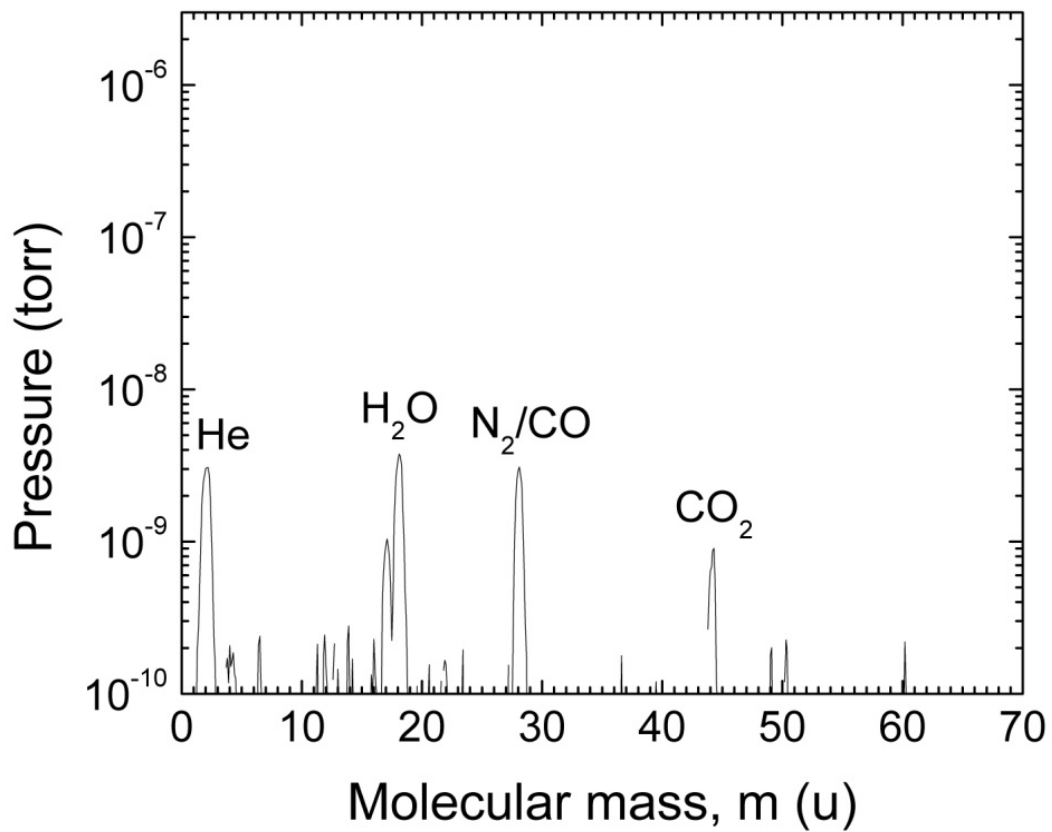


FIG. 8 The mass spectrum of the baked vacuum chamber.

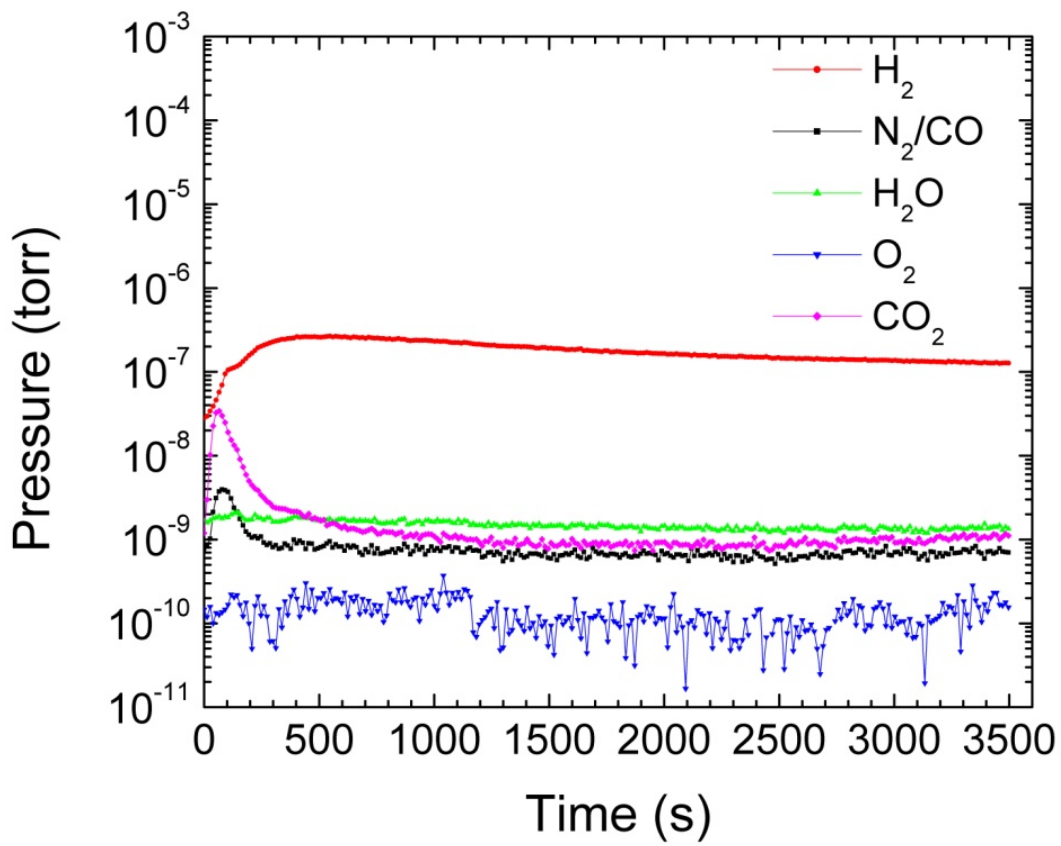


FIG. 9 Pressure versus time graph during degassing of the chamber inside at 700°C.

## B. Quantum design magnetic property measurement system

The temperature dependence of the magnetic property is measured by quantum design magnetic property measurement system (MPMS). In MPMS system, radio frequency (RF) superconducting quantum interference device (SQUID) is integrated with the cryogenic system and superconducting magnet [44]. In SQUID system, Josephson effect is applied. Josephson junction consists of two superconductors separated by the thin insulating (or metal) layer. For thin enough insulating layer, the Cooper pair wavefunctions in two superconducting layers can be correlated with the phase difference at the low temperature (below the critical temperature). Therefore, the tunneling supercurrent through the thin insulating layer is allowed in the insulating layer. The Josephson effect can be represented by the fundamental macroscopic relation of the phase difference [45].

$$I = I_c \sin\varphi, \frac{d\varphi}{dt} = \frac{2eV}{\hbar} \quad (2)$$

In equation (2),  $I_c$  is the critical current which is related to the temperature and the electrode material.  $\varphi$  is the difference between the phases of two wavefunctions.  $e$  and  $\hbar$  are the electron charge and the reduced Planck constant.  $V$  is the voltage across the junction. For  $V=0$  (dc Josephson effect), the constant supercurrent exists. For  $V > 0$  (ac Josephson effect), the phase  $\varphi$  of the current  $I$  is dependent on the voltage -  $\varphi = (2eV/\hbar)t = f \times t$  where  $f$  is the Josephson frequency. In MPMS system, RF SQUID is applied. RF SQUID has a superconducting ring shape with one Josephson junction. In RF SQUID, the phase difference  $\varphi$  is expressed by the magnetic flux ( $\varphi = 2\pi\Phi/\Phi_0$ ,  $\Phi_0 = h/2e$ ). Therefore, the flux sensitive property is applied to detect the induced current in the superconducting pick coils.

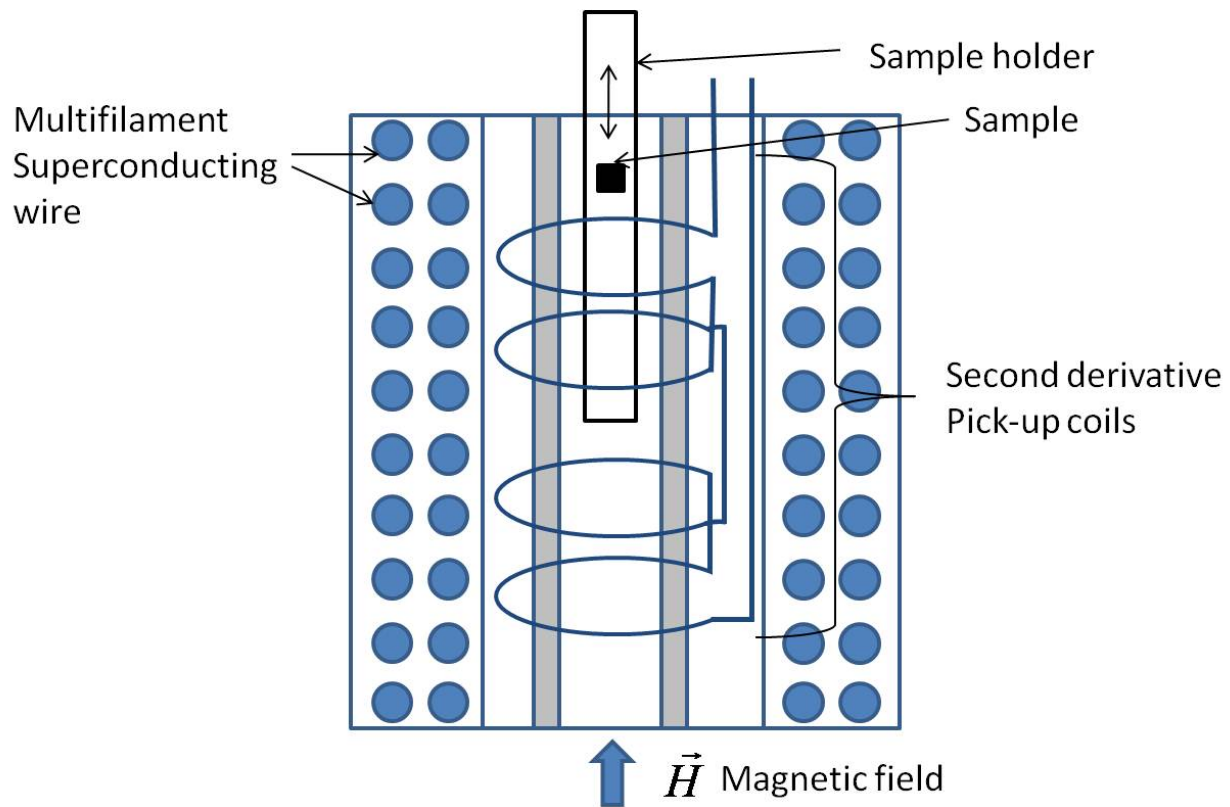


FIG. 10 MPMS SQUID system schematics of sample position (adapted from reference [44])

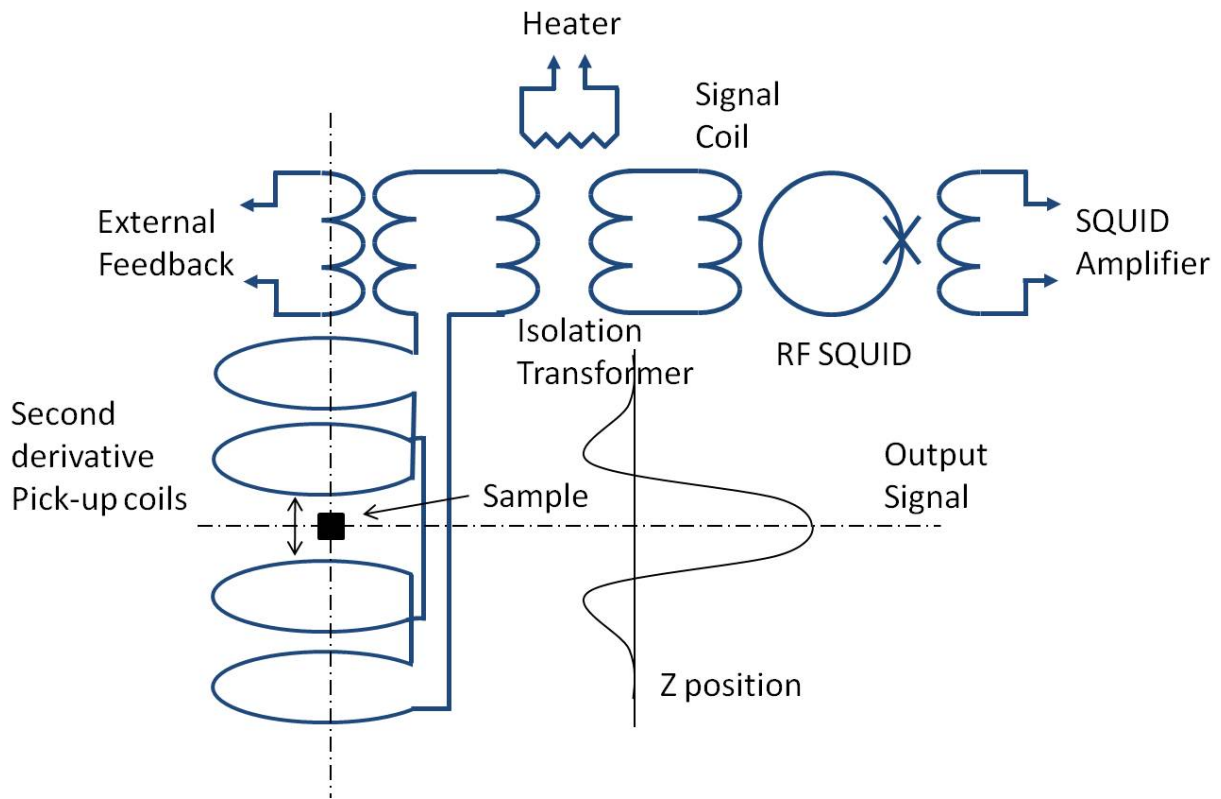


FIG. 11 MPMS detection system schematics (adapted from reference [44])

In operation, RF SQUID is weakly coupled by the current driving RF oscillator which sets the initial circuit current near the critical current  $I_c$  [46]. The FIG. 10 shows the superconducting magnet parts inside the MPMS system. In MPMS system, the superconducting magnet is placed in the liquid He. The superconducting magnet is composed of the inductive superconducting wires wound in the solenoid configuration. The superconducting wire loop is closed when the actual measurement is performed. The connection between the closed loop and the external power is controlled by the heater in the loop. In measurement, the superconducting magnet is initialized by the external power. When the desired magnetic field is reached, the circuit is alienated by turning off the heater in the loop [46]. The circulating current in the closed loop is preserved and sustained due to the superconducting property below the critical temperature. The magnetic field inside the superconducting solenoid is applied to the sample towards the upper direction due to the solenoid geometry. The signal from measurement is collected by four pick-up coils inside the superconducting magnet. Two pick-up coils on the top and the bottom are wound in the opposite direction to two other pick-up coils in the middle in a highly balanced position to shield the uniform field from the superconducting magnet. In FIG. 11, the schematic SQUID detection system is described. Second-derivative detective coil is coupled by the isolation transformer in the closed circuit form. The heater located between pick-up coil and isolation transformer is employed to remove the persistent current which is caused in the system operation process such as magnetic charging sequence. In measurement, the desired magnetic field and the temperatures is adjusted to the set values. When the condition above is satisfied, the sample is injected inside the pick-up coil from the top. At each step of z position, the induced current in the superconducting pick-up coil is transferred to SQUID by the isolation

transformer. In SQUID, the induced current is transformed to the voltage signal and finally, the output voltage signal from SQUID is amplified in the SQUID amplifier. In FIG. 11, the measured SQUID signal with respect to  $z$  position appears in the second derivative configuration. At each condition, the induced voltage signal is measured repeatedly and averaged [46]. The magnetic moment of the sample is calculated by multiplying the averaged voltage by the system calibration factor.

### C. Transmission electron microscopy

Transmission electron microscopy (TEM) is a well-developed technique to visualize the chemical structures of the sample by electron diffraction. In principle, the electron from the source is accelerated towards the specimen with several kV. The emitted electrons are carefully aligned by several magnetic lens parts as shown in the FIG. 12 [47]. The transmitted electrons are detected at the end of the electron passage. In this experiment, the High angle annular dark field (HAADF)-scanning transmission electron microscopy (STEM) technique was applied. In STEM, the convergent scanning electron beams is incident to the sample in the parallel direction to the optical axis of TEM. The electron beam transmitted through the sample can be detected by three different detectors placed in different positions. The detectors are located in the conjugate plane to the diffraction pattern. The bright field (BF) detector on the optical axis and annular dark field (ADF) detector intercept the transmitted electrons to form a bright field and dark field image, respectively. Here, HAADF detector is applied for high atomic number ( $Z$ ) contrast.

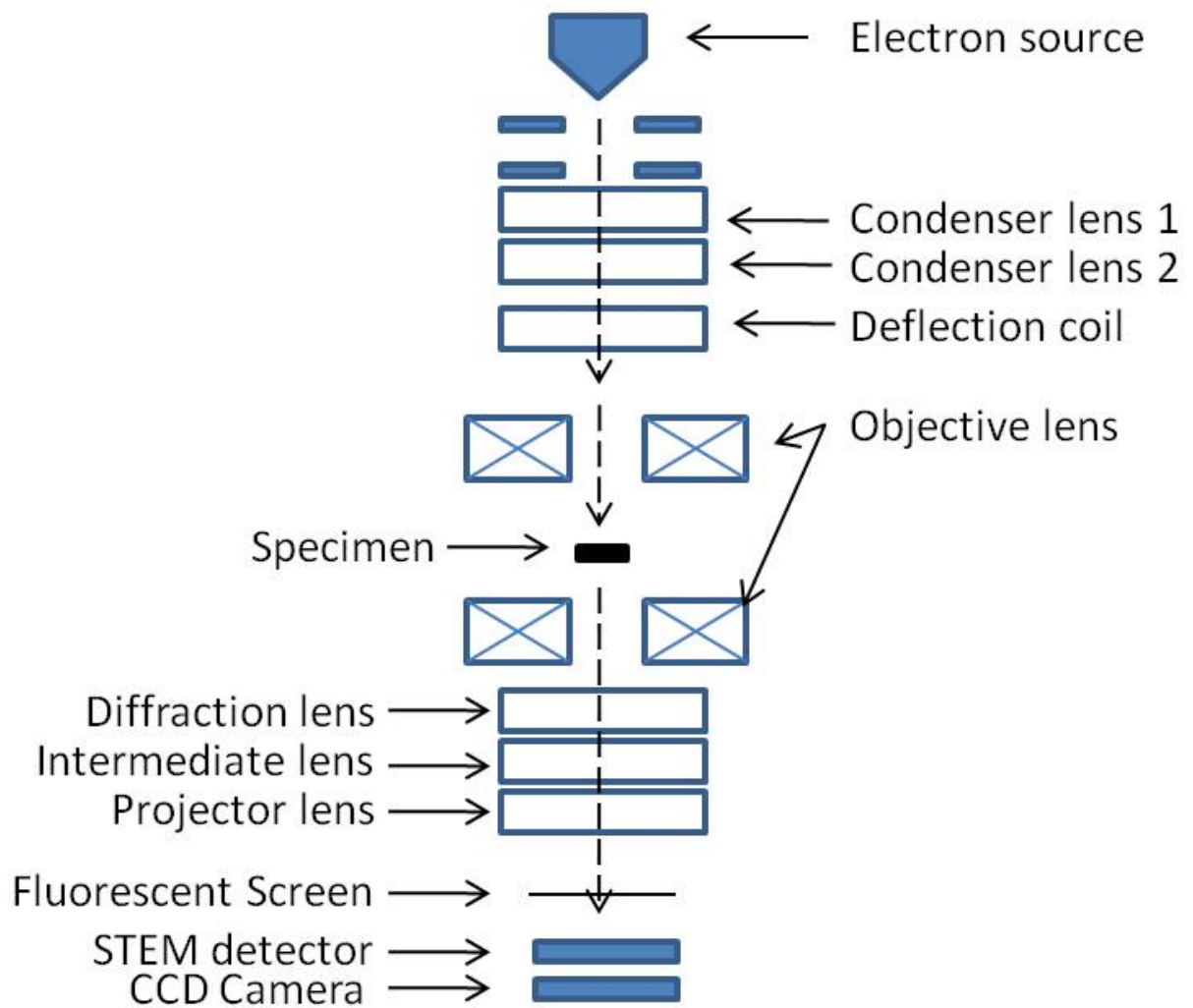


FIG. 12 The schematic of transmission electron microscopy equipment (adapted from the reference [47])

The high angle position of HAADF compared to the BF and ADF detectors enables the detection of highly scattered electrons by high Z elements. The specimen for TEM measurement is prepared by focused ion beam (FIB) technique.

### III. X-RAY AND NEUTRON SCATTERING TECHNIQUE

Scattering of particles and its related phenomena have been studied with the development of the 20th century's physics since the question of the origin of the matter has arisen. The wave-like and particle-like nature of the electromagnetic wave has been well-understood with the advent of the quantum mechanics. Many modern physics' principles such as the relativity, quantum mechanics, and quantum electrodynamics (QED) are associated with the property of electromagnetic wave and the discovery of fundamental particles in matter. The fundamental scattering phenomenon between particles is explained by the high energy particle physics theory under the consideration of the relativistic effect where the highly energetic particle whose speed is close to the speed of light is scattered by another particles. In the material science research, the scattering phenomenon is utilized in the low energy regime where the relativistic effect can be ignored and the elastic scattering is dominant. Quantum mechanically, the scattering between particles is described by their wavelike property. The incident free particle which has the momentum  $\hbar k$  (time  $t \rightarrow -\infty$ ) is described by the plane wavefunction  $\psi_{in}$  ( $= \psi_0 e^{ikz}$ ) which propagate towards one direction (defined as z coordinate) with the amplitude  $\psi_0$ . When this plane wave is incident on the scatterer particle, the scattered wave can be approximated around the scattering center by the local weak interaction assumption in the asymptotic form ( $r \rightarrow \infty$ ). The scattered wave  $\psi_{out}$  is expressed as  $\psi_0 b(e^{ikr} / r)$  where r is the distance from the scattering center and b is the scattering length which determines how much particles are scattered. The total scattering strength is represented by the cross section  $\sigma$  defined as in equation (3) [48].

$$\sigma = \frac{\text{number of scattered particles per second}}{\text{number of incident particles}} \quad (3)$$

According to the definition, the cross section is calculated for the scattered spherical wavefunction and written of the scattering length  $b$  as in equation (4).

$$\sigma = 4\pi b^2 \quad (4)$$

This general feature of scattering explained above can be applied in both X-ray and neutron scattering experiments. For the anisotropic scattering which shows the different scattering amplitude in a different angular direction, the differential cross section ( $d\sigma/d\Omega$ ) provides more useful expression, where  $\Omega$  is the solid angle.

X-ray is the electromagnetic wave which has the wavelength of around angstrom ( $10^{-10}\text{m}$ ) and mainly interacts with electrons. In X-ray scattering, the scattering length  $b$  for a free electron (Thompson scattering) is known as  $r_e = e^2 / (4\pi\epsilon_0 mc^2)$  [49]. The elastic scattering of X-ray by a free electron is designated by the quantum mechanical description - Feynman diagram as seen in the FIG. 13 (a). The FIG. 13 (a) shows one photon and one electron direct interaction in an elastic way. When X-ray is incident on an atom which possesses several bound electrons, X-ray is scattered by each electron. The FIG. 13 (b) shows the schematic of the scattering by the atom. Thus, the total intensity of the scattered X-ray beam can be calculated by the total sum of each electron's scattering. In this case, the scattering length  $b$  is determined by the density of the electrons as follows [49].

$$b = r_e f, f = \int \rho(r) e^{iq \cdot r} d^3x \quad (5)$$

In the equation (5),  $f$  is called the atomic form factor,  $q$ , the scattering vector. In X-ray scattering, it has been known that the elastic scattering and inelastic scattering (Compton, Raman), absorption and re-emission (fluorescence) occur, too. The inelastic scattering term in the scattering can be included by the additional dispersion term ( $f'$  and  $f''$ ) in the atomic form factor in the equation (6).

$$f = f^0 + f' + if'' \quad (6)$$

In a crystal structured material, atoms are arranged periodically as seen in the FIG. 13 (c). The total scattering amplitude by the crystal structure is calculated in the form of the structure factor  $F$ .

$$F = \sum_n f_n e^{-M_n} e^{iQ \cdot r_n} \quad (7)$$

In equation (7),  $Q$  is the scattering vector,  $r_n$ , the position of an atom in the unit cell and  $M_n = B \sin^2 \theta / \lambda^2$ . The exponential term  $e^{-M_n}$  is the Debye-Waller term which explains the temperature vibration of atoms.

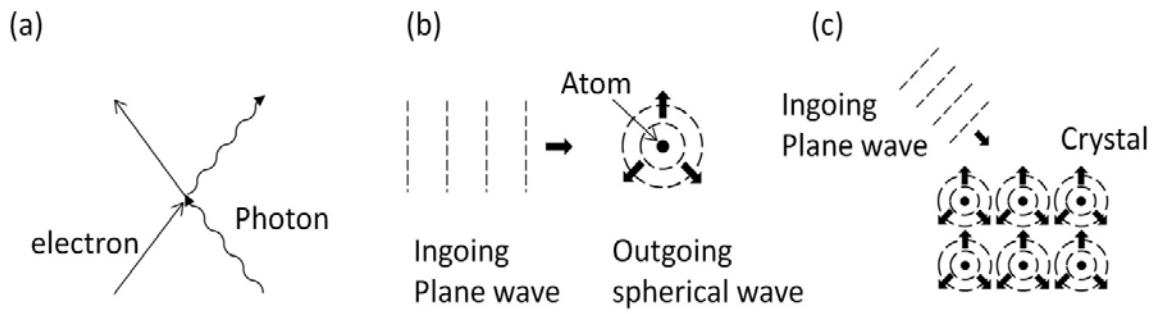


FIG. 13 (a) Feynman diagram of elastic scattering of free electron and photon (b) the schematic of scattering of an incident particle by one atom and (c) by crystal

Neutron scattering with a single nucleus in matter is represented by the Fermi pseudo potential which is an effective potential for the slow neutrons ( $\sim$  a few Å wavelength range) evaluated within the born approximation limit as in equation (8) [50].

$$V = \frac{2\pi\hbar^2}{m_n} b\delta(r) \quad (8)$$

For the slow neutrons, the potential by the nucleus can be treated as the point-like source represented by  $\delta$ -functional form in the above.

#### A. X-ray and polarized neutron reflectivity for thin film

The reflectivity has been useful technique for the characterization of multilayered thin film structure. First, in the neutron scattering for the homogeneous thin film, the scattering potential is expressed as  $V_N = \frac{2\pi\hbar^2}{m_n} \rho(z)$ , where  $\rho(z)$  is the neutron scattering length density .

For the ideal case, the multilayered thin film structure is assumed to be composed of the several homogeneous 2 dimensional slabs. Thus, the scattering length density is assumed to be dependent on the thickness direction ( $z$ ) of the axis.

In the single homogeneous thin film medium, the scattering length density  $\rho(z)$  is assumed as a constant value. Quantum mechanically, the wavelike behavior of a single incoming neutron particle from the source to the thin film structure can be explained by the Schrodinger wave equation (9) [51].

$$\left( \frac{\partial^2}{\partial z^2} + k_{0z}^2 - 4\pi\rho(z) \right) \psi(z) = 0 \quad (9)$$

In the equation (9),  $\psi(z)$  is the wavefunction of the neutron. In the Schrodinger equation above, only the perpendicular component (z axis direction) to the film surface is considered because the scattering potential depends only on the z component. The solution for the Schrodinger equation above is the free travelling wavefunction which has the wavevector k of z component in the equation (10) :

$$k_z = \sqrt{k_{0z}^2 - 4\pi\rho} = k_{0z} \sqrt{1 - \frac{4\pi\rho}{k_{0z}^2}} \quad (10)$$

First, let's consider the simple scattering case which has one boundary surface. When the neutron is incident to the thin film surface, the wavefunction in one medium can be expressed in the combination of the incoming and reflected beam :

$$\begin{aligned} \psi_2 &= \psi_{2in} e^{ik_2z} + \psi_{2re} e^{-ik_2z} \\ \psi_1 &= \psi_{1in} e^{ik_1z} + \psi_{1re} e^{-ik_1z} \end{aligned} \quad (11)$$

In the equation (11),  $\psi_1$ ,  $\psi_2$  are the wavefunctions of the neutron in the medium 1 and medium 2.

In each equation,  $\psi_{in}$  and  $\psi_{re}$  represents the amplitude of the incoming and reflected neutron wave. The FIG. 14 shows the scattering case for the semi-infinite plane. In the medium 2 which is infinite, only the transmitted wave exists ( $\psi_{2re} = 0$  in the equation (11)). At the boundary of

the medium 1 and 2, the wavefunction amplitude is decisively calculated by the continuity condition ( $\psi_1 = \psi_2, \partial_z \psi_1 = \partial_z \psi_2$  at  $z=0$ ) of the wavefunction. The reflectivity ( $r_{1,2} \equiv \frac{\psi_{1re}}{\psi_{1in}}$ ) at the boundary is easily obtained after the simple calculation as in equation (12) :

$$r_{1,2} \equiv \frac{\psi_{1re}}{\psi_{1in}} = \frac{k_{1z} - k_{2z}}{k_{1z} + k_{2z}} \quad (12)$$

In the N-multilayered structure, the scattered wave can be considered at the same condition. As shown in the FIG. 15, the three layers are considered. The wavefunction in the n th layer numbered from the top is written in equation (13) :

$$\begin{aligned} \psi_n &= \psi_{n,in} e^{ik_n z} + \psi_{n,re} e^{-ik_n z} \\ \psi_{n-1} &= \psi_{n-1,in} e^{ik_{n-1} z} + \psi_{n-1,re} e^{-ik_{n-1} z} \end{aligned} \quad (13)$$

The boundary condition at the interfaces directly produces the famous Parratt recursion relation in the equation (14) [52-54].

$$\begin{aligned} R_{n-1,n} &= \frac{r_{n-1,n} + R_{n,n+1} e^{i2k_n d}}{1 + r_{n-1,n} R_{n,n+1} e^{i2k_n d}}, \\ r_{n-1,n} &= \frac{k_{n-1} - k_n}{k_{n-1} + k_n}, \quad k_n = \sqrt{1 - \frac{4\pi\rho_n}{k_0^2}} k_0 \end{aligned} \quad (14)$$

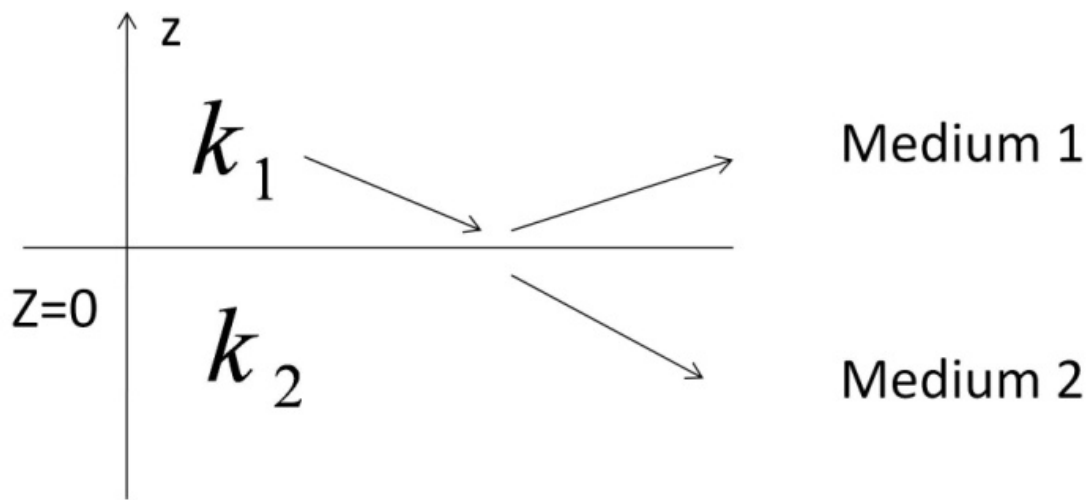


FIG. 14 scattering case for the semi-infinite plane.  $k_1$  and  $k_2$  is the wavenumber at each medium.

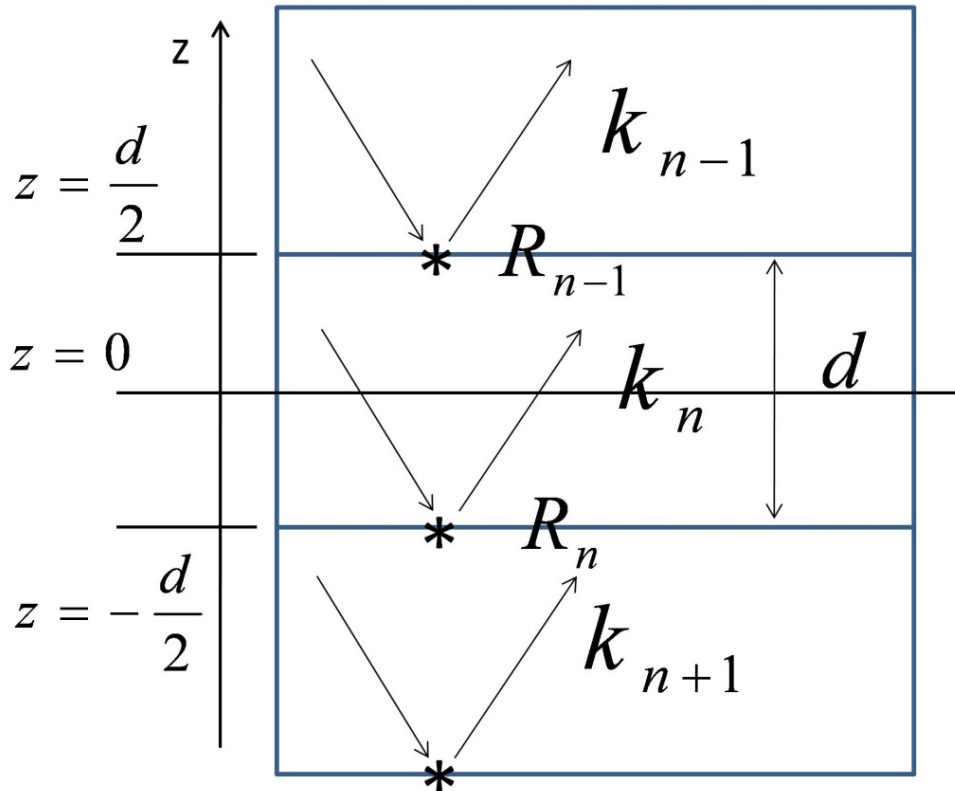


FIG. 15 Scattering case at three (n-1)th,(n)th and ( n+1)th layers in the multilayered structure. The arrows in the figure indicate the transmitting and reflected wave direction with the wavenumber  $k_{n-1}$ ,  $k_n$ ,  $k_{n+1}$ .  $d$  is the thickness of the (n)th layer and  $R_n$ ,  $R_{n-1}$  represent the reflectance at each boundary.

The polarized neutron reflectivity can be easily simulated by the Parratt recursion relation for the saturated in-plane magnetic thin film along the applied magnetic field for the two spin channel (spin++, spin--) while spinflip case is more investigated in the matrix formalism with more flexibility [55]. The polarized neutrons can be utilized to study the magnetic property of the multilayered films due to the interaction between the magnetic moment of the neutron and the magnetic induction in the film [55]. For the non-spinflip neutron scattering (two spin channel case), the potential difference  $V$  is expressed as in the equation (15) for the thin film magnetization parallel, or antiparallel to the neutron moment.

$$V = \mp \mu_N \cdot B = \mp \mu_N \mu_0 M \quad (15)$$

In the equation (15),  $\mu_N$  is the neutron moment,  $\mu_0$  permeability for free space, and  $M$ , the magnetization. In the normal polarized neutron scattering experiment, the external magnetic field is applied in the same direction as the neutron polarization direction. In the experiment, two polarizations of neutrons with respect to the guiding field are possible. By comparison between two cases, the magnetic states of the film are carefully examined. The total potential including the magnetization in the neutron scattering is expressed as in the equation (16) [53, 56].

$$V_{\text{total}} = V_N \mp \mu_N \cdot B = \frac{2\pi\hbar^2}{m_n} \rho(z) \mp \mu_N \mu_0 M \quad (16)$$

As presented in the previous Schrodinger equation formulation, the magnetic contribution term can be included as the additional scattering length density and therefore, the magnetization property can be obtained by comparing the parallel (spin++) and antiparallel (spin--) cases.

For X-ray reflectivity, the same procedure can be applied as the neutron scattering case. In the X-ray reflectivity, the additional absorption  $\beta$  term should be considered in the refractive index, that is,  $n=1-\delta+i\beta$ . The refractive index in X-ray reflectivity has the corresponding relations with scattering length  $b$  as in the equation (17).

$$\text{Re } b = \frac{2\pi}{\lambda^2} \delta, \quad \text{Im } b = \frac{2\pi}{\lambda^2} \beta \quad (17)$$

Therefore, the same formalism and source code is applied in neutron and x-ray reflectivity.

In reality, the thin film grown by sputtering technique has the rough surface at the interface due to its growth mechanism. The total roughness of the surface can be understood in the statistical methods. In the modeling of the roughness, the morphology of the rough surface is considered in the random fluctuation of the surface. In the macroscopic point of view, the height-height correlation can be considered as the statistical random variable [57]. The Nevot-Croce form has been derived and known that it explains the reflectivity data crossover region between near the critical angle and the large angle region where the Born approximation is valid [57-60]. Based on the explained theory above, the fitting program is coded by the LABVIEW program. The LABVIEW language has the advantage of the convenient modification and user-friendly interface. The FIG. 16 shows the schematic diagram for the program routine.

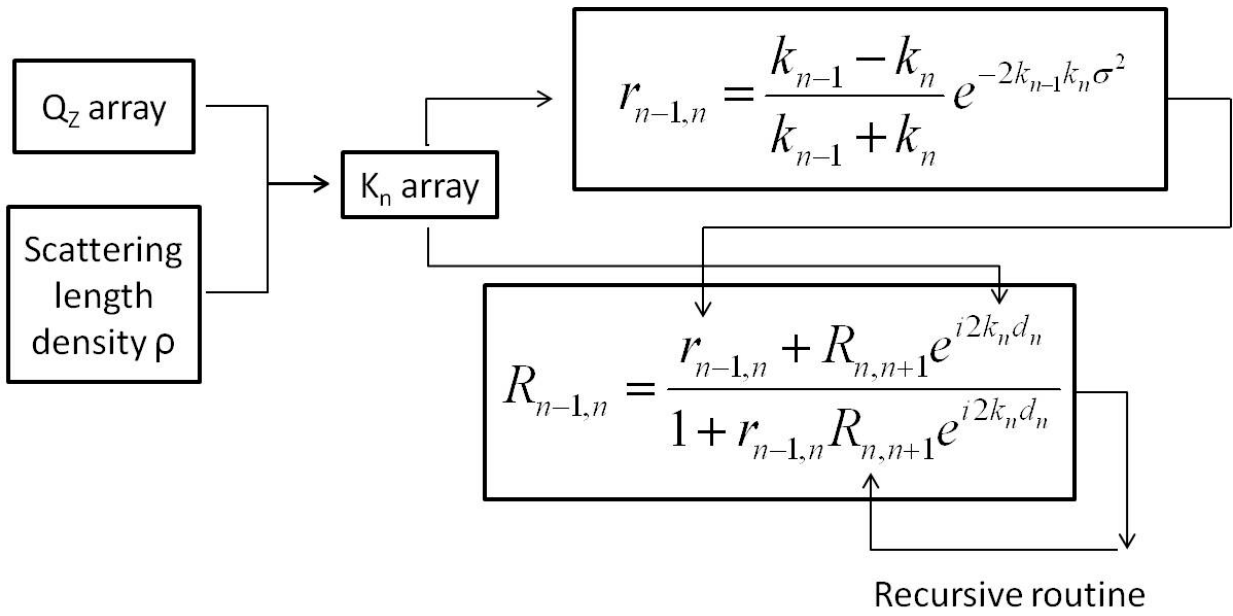


FIG. 16 The diagram of the Parratt recursive relation for the reflectivity of the multilayered structure

The scattering program receives the  $Q_z$  scattering vector perpendicular to the film surface and the scattering length density arrays. For a given  $Q_z$ , the wavenumber is calculated at each medium. The recursive calculation begins from the substrate and the first film medium. The reflectivity at the interface between the substrate and the first medium can be considered as the case of the semi-finite plane scattering. In this case, reflectivity is simply expressed as the Fresnel formula in the normal optics. For the next interface case, the Parratt recursion relation is applied to obtain the reflectivity in the second film medium. At each interface, the Nevot-Croce roughness term is included in the exponential form. The recursive routine is performed for the whole multilayers until it reaches the air.

#### B. Polarized neutron reflectometry

The polarized neutron reflectivity measurement is performed at the beam line 4A Magnetic Advanced Grazing Incidence Spectrometer (MAGIC) in the Spallation Neutron Source in Oak Ridge National Laboratory. The FIG. 17 shows the schematic of the Spallation Neutron Source operated at the 1.4MW beam power in Oak Ridge National Laboratory. As shown in figure, Spallation Neutron Source is composed of the linear accelerator, accumulation ring, and the target part. In the linear accelerator part, negatively charge Hydrogen ions are accelerated inside the normal metal Cu and Nb superconductor radio frequency cavity. Two-electron-stripped ion (proton) by a thin foil is accumulated to form the bunch of protons at the Accumulator Ring. Each bunch of protons is injected to the heavy metal (Hg) target at 60Hz frequency to produce the neutrons. The low energetic neutrons adjusted by Moderator  $H_2O$ , or liquid hydrogen are guided to each beam line which is located near the target.

The polarized neutron reflectivity experiment is performed in the beam line 4A which uses the 1.8~14Å wavelength and 98.5% polarized neutron beams, the applicable magnetic field 1.2T with 5cm gap between electromagnetic poles with  $10^{-8}$  minimum reflectivity [61]. The schematic reflectometer setup is described in the FIG. 18. From the moderator, the neutrons are guided into the beam line with the deflected beam path to avoid the fast neutron beam. The injected neutron beams are polarized by the Fe/Si supermirror polarizer which allows the transmission of one spin channel of neutrons selectively. The polarized neutrons through Polarizer are collimated with three slits and introduced to the sample with the weak applied guiding field which supports the neutrons to keep their polarization.

Once the neutron beam is polarized at one direction, the polarization direction can be controlled by the spin flipper which changes the initial spin polarization into the opposite direction adiabatically, or non-adiabatically. In the reflectivity experiment, two different spin polarizations of the neutrons are selected and applied for two spin channel measurements. Each spin channels of the neutrons (spin ++, +-, -+, --) is well controlled and detected independently by two spin flippers. In SNS, the continuous wavelength spectrum of the pulsed neutrons is resolved by time-of-flight (TOF) technique. In TOF method, the flight time of the neutrons between the production and the detection are recorded at each spallation period, which provides the information of the wavelength of each detected neutron. For the measured intensity and the time-of-flight data, the data reduction process such as the background subtraction, the integration for the dispersive signals is performed by the data reduction package provided in the ORNL web site.

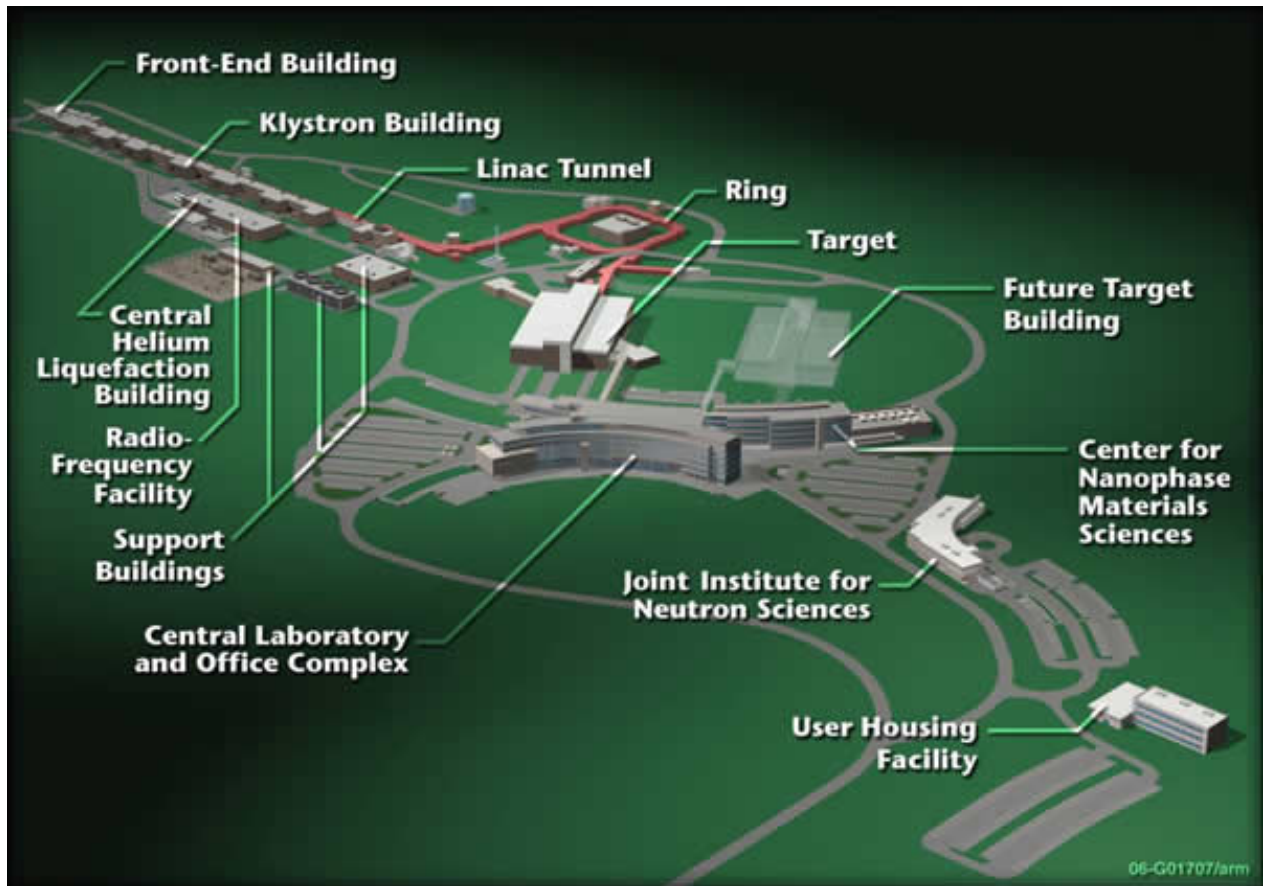


FIG. 17 The schematic of the Spallation Neutron Source facility in Oak Ridge National Laboratory (adapted from the reference [61])

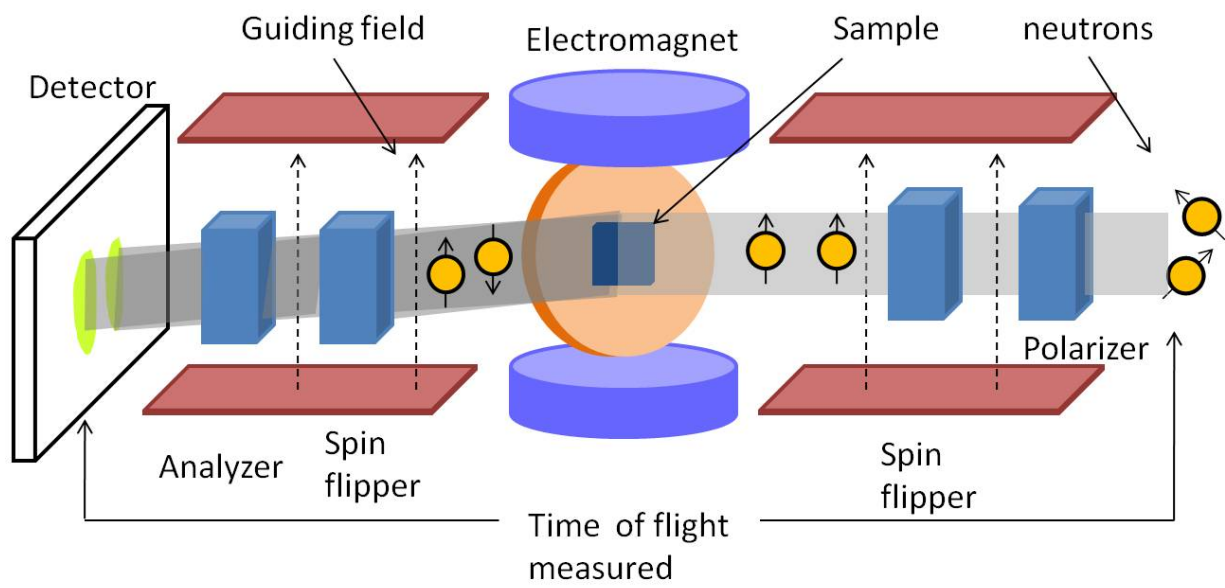


FIG. 18 The schematic of the polarized neutron reflectometry setup in the beam line.

## C. X-ray diffraction

### 1. High angle X-ray diffraction

High angle X-ray diffraction can be used to characterize the crystal structure of the materials. In a crystal structure, the scattering amplitude is the structure factor  $F$ . For high angle X-ray diffraction experiment, the polarization of X-ray electromagnetic wave is included in the scattering term. The polarization factor ( $P$ ) for unpolarized X-ray source is  $1/2(1 + \cos^2 \theta)$ . The scattered X-ray from thin film is detected for the specific angle position. In this case, the intensity of the scattered beam can be evaluated in the form of differential cross section ( $d\sigma / d\Omega$ ). For small parallelepipedon crystal which has the numbers  $N_1, N_2, N_3$  of the primitive cell with unit vector  $a_1, a_2, a_3$  at each x, y, z direction, the differential cross section for unpolarized X-ray source is written as in the equation (18) [49].

$$\frac{d\sigma}{d\Omega} = r_e^2 P |F|^2 \frac{\sin^2(1/2(k - k_0) \cdot N_1 a_1)}{\sin^2(1/2(k - k_0))} \frac{\sin^2(1/2(k - k_0) \cdot N_2 a_2)}{\sin^2(1/2(k - k_0))} \frac{\sin^2(1/2(k - k_0) \cdot N_3 a_3)}{\sin^2(1/2(k - k_0))} \quad (18)$$

In the actual diffraction experiment, the ideal detection of the diffracted beam which satisfies the exact Bragg diffraction condition is limited by the beam divergence for a large crystal, instrumental resolution, or the slight mosaic of crystal sample [62]. Thus, instead, the integrated intensity for a finite angular breath of the diffraction peak is often considered for a better comparison between theoretical and experimental results.

The integrated differential cross section  $(d\sigma/d\Omega)_{\text{Integrated}}$  and intensity  $I$  is expressed in the equation (19), (20) [49].

$$\left(\frac{d\sigma}{d\Omega}\right)_{\text{Integrated}} = r_e^2 P |F|^2 \frac{1}{\sin 2\theta} \frac{\lambda^3}{v_c} N_1 N_2 N_3 \quad (19)$$

$$I = I_0 \left(\frac{d\sigma}{d\Omega}\right) = I_0 r_e^2 P |F|^2 \frac{1}{\sin 2\theta} \frac{\lambda^3}{v_c} N_1 N_2 N_3 \quad (20)$$

Here, the term  $1/\sin 2\theta$  is the Lorentz term,  $I_0$ , the incident flux. Additionally, the temperature dependent term and thickness absorption by the sample is considered by the equation (21) [49].

$$A(\theta) = A_0 \left(1 - e^{-\frac{2\mu t}{\sin \theta}}\right) \quad (21)$$

Here,  $A_0$  is the constant,  $t$ , the thickness of the film and  $\mu$ , the absorption coefficient.

In the experiment, Philips X'Pert MPD system is used. The FIG. 19 shows the schematic of Philips X'Pert MPD system for thin film measurement with the parallel beam optics equipped [63]. In X-ray tube, electrons at a high voltage are accelerated on the metal target to generate X-ray, where a few percent (<1%) of the energy is transformed into X-ray. At a certain energy range, the intensive characteristic spectrum lines (named K, L, M) can be achieved and selectively taken. For Cu metal target applied in this experiment, the main characteristic spectrum line is  $K_{\alpha 1}$  (wavelength  $\lambda=1.54390\text{\AA}$ ) (strongest intensity),  $K_{\alpha 2}$  ( $1.540562\text{\AA}$ ) (less strong) and  $K_{\beta}$  ( $1.392218\text{\AA}$ ) (weak) [64]. In the experiment,  $K_{\beta}$  line is suppressed considerably

by  $\beta$ -filter on the primary optical beam path to take advantage of the unique wavelength ( $K_{\alpha 1}$  line) of X-ray. The generated divergent X-ray beam is well arranged by Soller slits where thin metal plates are placed inside parallel to the diffractometer rotational plane to obtain a line of several parallel beams perpendicular to the planes. Line focused X-ray beam is finally introduced to the sample through divergence slit and mask. The diffracted beam from the sample at a certain angle is guided by the parallel beam collimator to the detector with flat graphite monochromator where the background radiation and sample fluorescence are reduced. X-ray beam is detected by the proportional detector appropriate for Cu  $K_{\alpha}$ . In the normal XRD ( $2\theta$ - $\omega$ ) scan, the sample and the detector is rotated of z-axis on the x-y plane with the angle  $\omega=\theta$ . Before the measurement, the sample position is carefully calibrated for the translational x, y, z (sample height) and three different rotational offset.

## 2. Rocking curve scan

The quality of the epitaxial film can be checked by the rocking curve scan in XRD [65]. The schematic of the rocking curve scan is illustrated in FIG. 20. In the rocking curve scan, the initial angular position of the detector  $2\theta$  and the sample  $\omega$  is aligned along one Bragg peak position which is found in the normal  $2\theta$ - $\omega$  scan. Then, the sample is rocked around the initial angle while the detector position  $2\theta$  is kept fixed as seen in the figure.

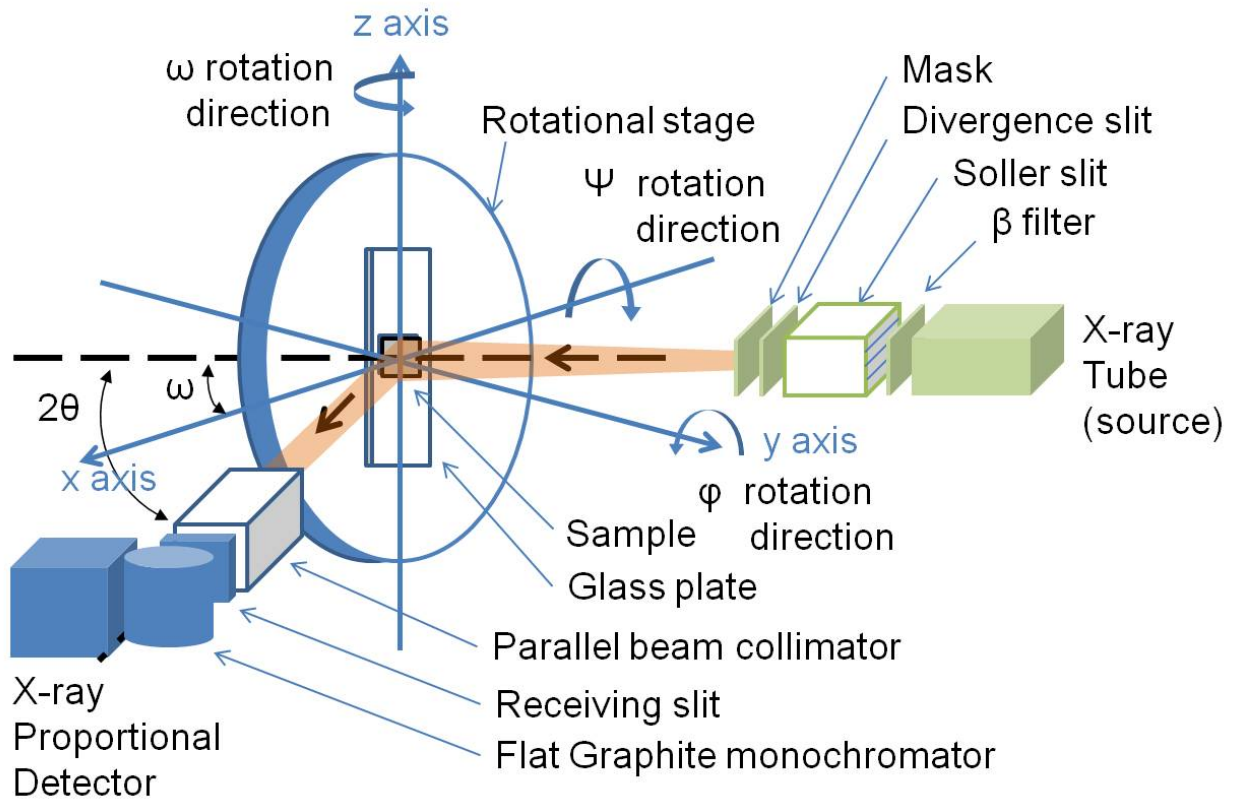


FIG. 19 The schematic of the X-ray diffraction Philips setup

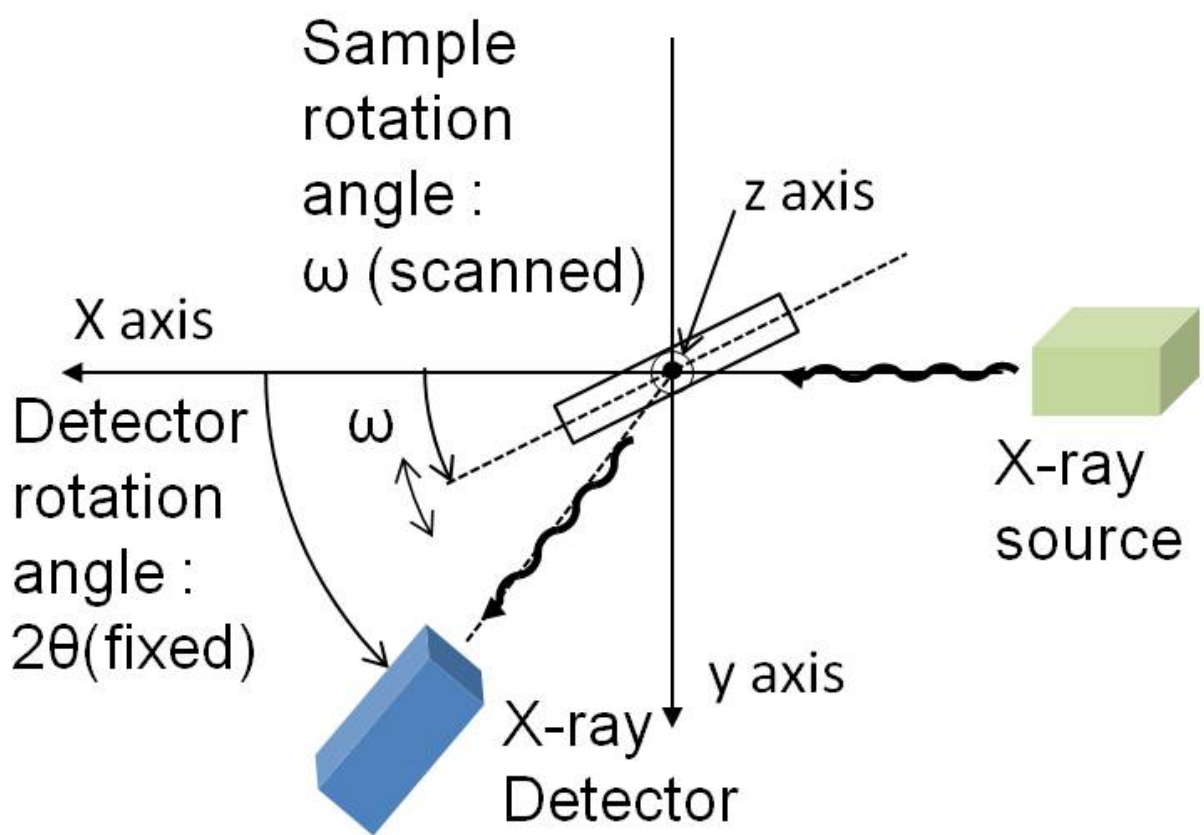


FIG. 20 The schematic of the rocking curve scan. The X-ray source and detector is placed on the XY plane.

The broadening of the measured intensity peak in the intensity versus  $\omega$  graph provides an estimation of the portion of the crystal oriented at the specific crystallographic direction in comparison with the case of the single crystal.

### 3. Pole figure measurement

In the normal XRD ( $2\theta$ - $\omega$ ) scan, the crystal orientation of the lattice plane is measured in the film plane direction. The crystallinity, or preferred orientation of the film texture can be checked by measuring diffraction at different angular directions of the found specified film orientation as shown in the FIG. 21. The existence of the pole configuration and its symmetry provides the information of the morphology of the crystalline structure or, the dominant existence of the preferably oriented crystallites. In experiment, the total pole configuration can be checked by the whole scan of the angle of all possible diffraction condition. In thin film research, often, the maximum intensity of the specific orientation is scanned and presented in the literature. In the measurement of the specific pole figure, the detector ( $2\theta$ ) and sample ( $\omega$ ) angular position is adjusted at the specific Bragg diffraction condition which is expected in the crystal structure at the specific angle other than the film plane direction. In the figure above, it is shown that the sample is tilted from the in-plane at the specific tilting angle  $\psi$ . Then, the film is rotated for the azimuthal angle to examine the specific diffraction peak (maximum intensity) and its repetition which account for the symmetry of the crystal structure.

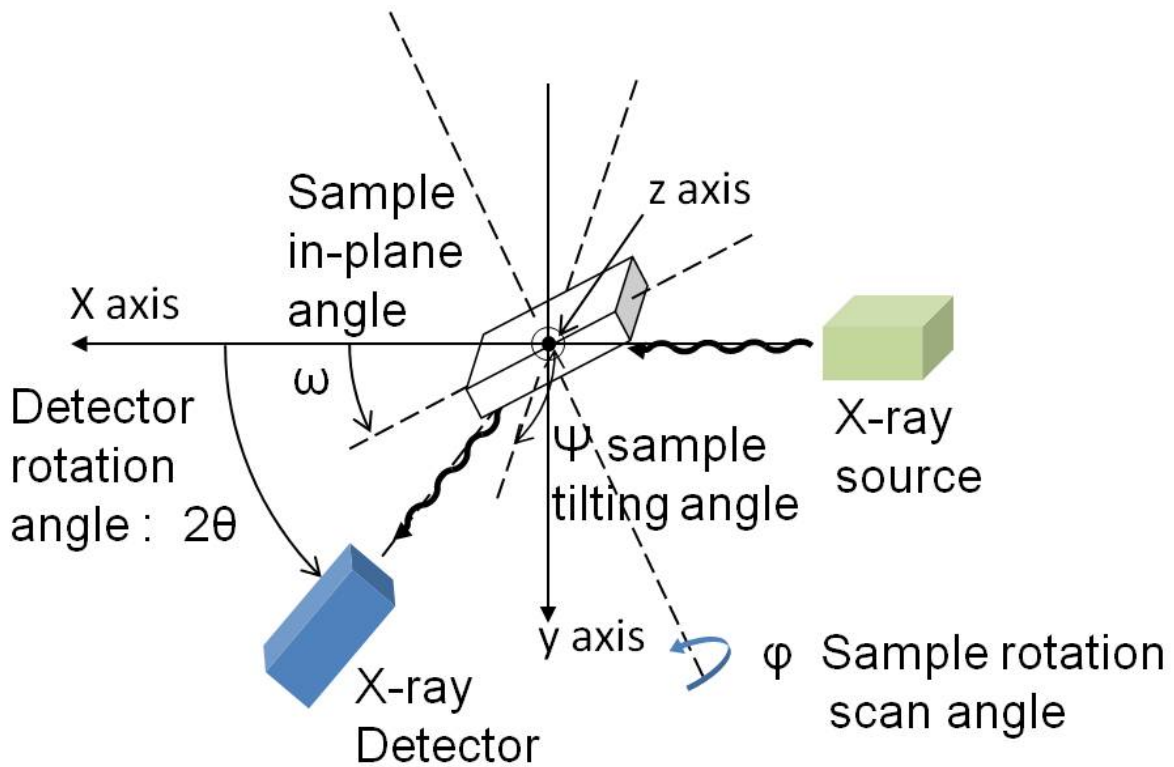


FIG. 21 The schematic of the X-ray setup for pole figure measurement. The dotted line indicates the rotational axis of the sample. While X-ray source and detector is placed on the XY plane, the sample plane is tilted at  $\psi$  angle from Z-axis.

## IV. FePtRh MULTILAYER SYSTEM

### A. Sample preparation

In the sample preparation, DC magnetron sputtering technique is applied. For the epitaxial film growth, the ultra high vacuum (UHV) pressure is prepared in ADAM system with the monitoring residual gas analyzer (RGA). Sputtering pressure under Ar gas input is measured by Pirani pressure gauge which operates within  $10^{-3}$  torr and higher pressure range. In film deposition, the cathode 50W power is applied. In vacuum chamber, a-plane sapphire substrate is mounted on the center of Tantalum sample holder. In heating the substrate, Halogen lamp (120V, 300W) is placed in the back of the Tantalum sample holder. The external input power to the lamp is adjusted by the variable transformer. The temperature of the sample holder is calibrated by the thermocouple (K type) at each applied external voltage. In this experiment, 8 period of  $[\text{Fe}_{50}\text{Pt}_{45}\text{Rh}_5(10\text{nm})/\text{Fe}_{50}\text{Pt}_{25}\text{Rh}_{25}(20\text{nm})]$  multi-layered superlattice samples are prepared on the  $\text{Al}_2\text{O}_3$  (11 $\bar{2}$ 0) (a-plane) substrate. For  $L1_0$  epitaxial growth, Cr 6nm and Pt 14nm buffer and seed layers are chosen. It has been already known that Cr and Pt buffer and seed layer improves the epitaxy of  $L1_0$  structure [4, 66, 67]. The substrate temperature was maintained at 600°C during film deposition. Additionally,  $[\text{Fe}_{50}\text{Pt}_{45}\text{Rh}_5(10\text{nm})/\text{Fe}_{50}\text{Pt}_{25}\text{Rh}_{25}(20\text{nm})]$  bilayered sample, two single layered  $\text{Fe}_{50}\text{Pt}_{45}\text{Rh}_5$  and  $\text{Fe}_{50}\text{Pt}_{25}\text{Rh}_{25}$  (50nm) samples are also prepared with the same Cr buffer, Pt seed and capping layers on the  $\alpha\text{-Al}_2\text{O}_3$  (11 $\bar{2}$ 0) to identify the epitaxial relation between layers.

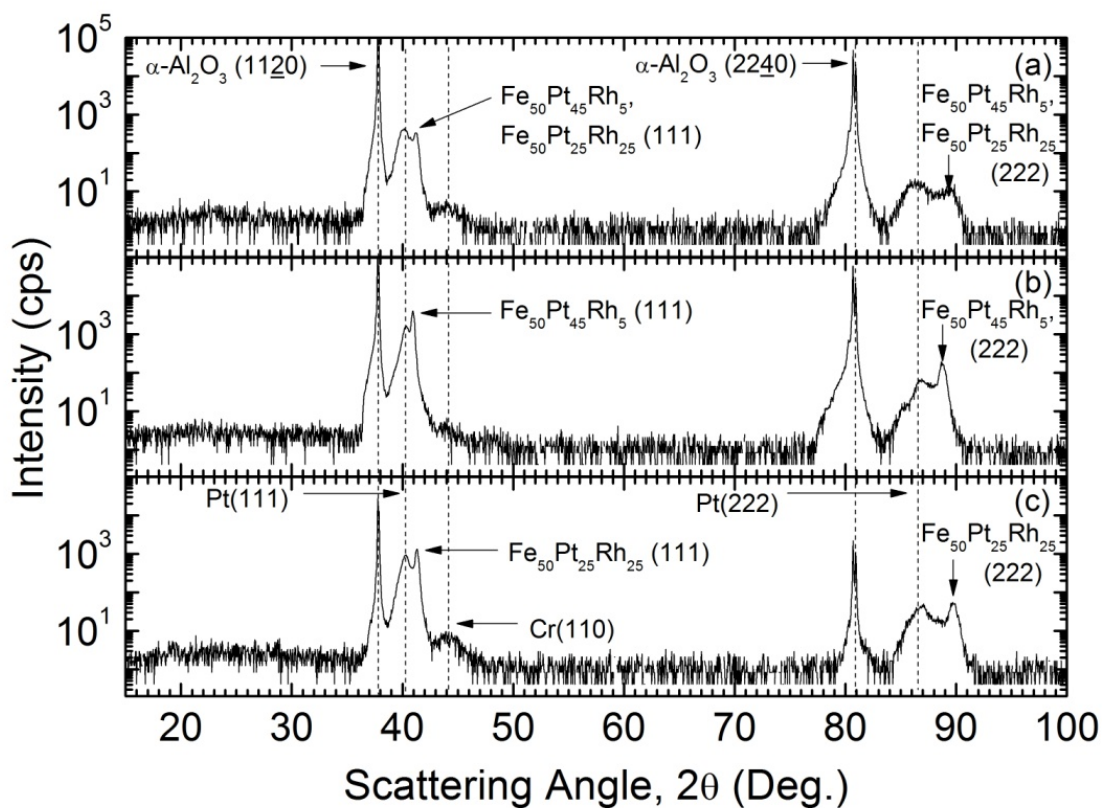


FIG. 22 XRD result for (a) Fe<sub>50</sub>Pt<sub>45</sub>Rh<sub>5</sub> (10nm)/Fe<sub>50</sub>Pt<sub>25</sub>Rh<sub>25</sub> (20nm) bilayer, (b) Fe<sub>50</sub>Pt<sub>45</sub>Rh<sub>5</sub> (50nm), (c) Fe<sub>50</sub>Pt<sub>25</sub>Rh<sub>25</sub> (50nm) single layered samples. The dotted line indicates the common peak observed for Pt(111), Cr(110), α-Al<sub>2</sub>O<sub>3</sub> (1120) and α-Al<sub>2</sub>O<sub>3</sub> (2240) from the common seed layer and the substrate. In (a), two (111) peaks from Fe<sub>50</sub>Pt<sub>45</sub>Rh<sub>5</sub> (10nm) and Fe<sub>50</sub>Pt<sub>25</sub>Rh<sub>25</sub> (20nm) appears as merged due to the close peak position.

The deposition flux of  $\text{Fe}_{50}\text{Pt}_{45}\text{Rh}_5$ ,  $\text{Fe}_{50}\text{Pt}_{25}\text{Rh}_{25}$  targets were 0.97 Å/s, 0.87 Å/s respectively and 0.49 Å/s, 1.00 Å/s for Cr and Pt.

#### B. X-ray characterization of FePtRh single - and bi-layered samples

To identify the FePtRh crystallographic orientation,  $\theta$ -2 $\theta$  XRD scan is performed for a single layered sample. Fig. 20 shows XRD measurement results of  $\text{Fe}_{50}\text{Pt}_{45}\text{Rh}_5$  (50nm),  $\text{Fe}_{50}\text{Pt}_{25}\text{Rh}_{25}$  (50nm) single-layered and  $\text{Fe}_{50}\text{Pt}_{45}\text{Rh}_5/\text{Fe}_{50}\text{Pt}_{25}\text{Rh}_{25}$  bilayered sample. In FIG. 22 (b) and (c),  $\text{Fe}_{50}\text{Pt}_{45}\text{Rh}_5$ ,  $\text{Fe}_{50}\text{Pt}_{25}\text{Rh}_{25}$  (111), (222) and Pt (111), (222) separate peak positions are shown in each single layered FePtRh sample. Due to the compositional and structural similarity between two  $\text{Fe}_{50}\text{Pt}_{45}\text{Rh}_5$ ,  $\text{Fe}_{50}\text{Pt}_{25}\text{Rh}_{25}$ , the peak positions appears closely in a merged form as in the FIG. 22 (a). In three samples, the common Pt (111), (222), and  $\alpha\text{-Al}_2\text{O}_3$  (11 $\bar{2}$ 0), (2240) substrate peaks are observed and noted with the dotted line in the FIG. 22. At  $2\theta=44.1$ , small Cr 110 peak is also clearly seen in FIG. 22 (a) and (c). The small Cr peak in the FIG. 22 (b) indicates that the improvement of the epitaxial Cr (110) growth is sensitive to the actual sputtering condition in the vacuum chamber. The film quality of the epitaxy is represented in the full width of half maximum (FWHM) of the rocking curve peak. For the identified  $2\theta$  position of  $\text{Fe}_{50}\text{Pt}_{45}\text{Rh}_5$ ,  $\text{Fe}_{50}\text{Pt}_{25}\text{Rh}_{25}$  (111) in high angle XRD measurement,  $\Omega$  scan is performed at the optimized  $\Omega$ ,  $\Psi$  angles. As shown in FIG. 23, the full width of half maximum (FWHM) of  $\text{Fe}_{50}\text{Pt}_{45}\text{Rh}_5$ ,  $\text{Fe}_{50}\text{Pt}_{25}\text{Rh}_{25}$  (111) peak are  $1.21^\circ$ ,  $1.25^\circ$ . The epitaxy of  $\text{Fe}_{50}\text{Pt}_{45}\text{Rh}_5$ ,  $\text{Fe}_{50}\text{Pt}_{25}\text{Rh}_{25}$  layer is examined in the measurement of the pole figure for FePtRh (111) plane direction.

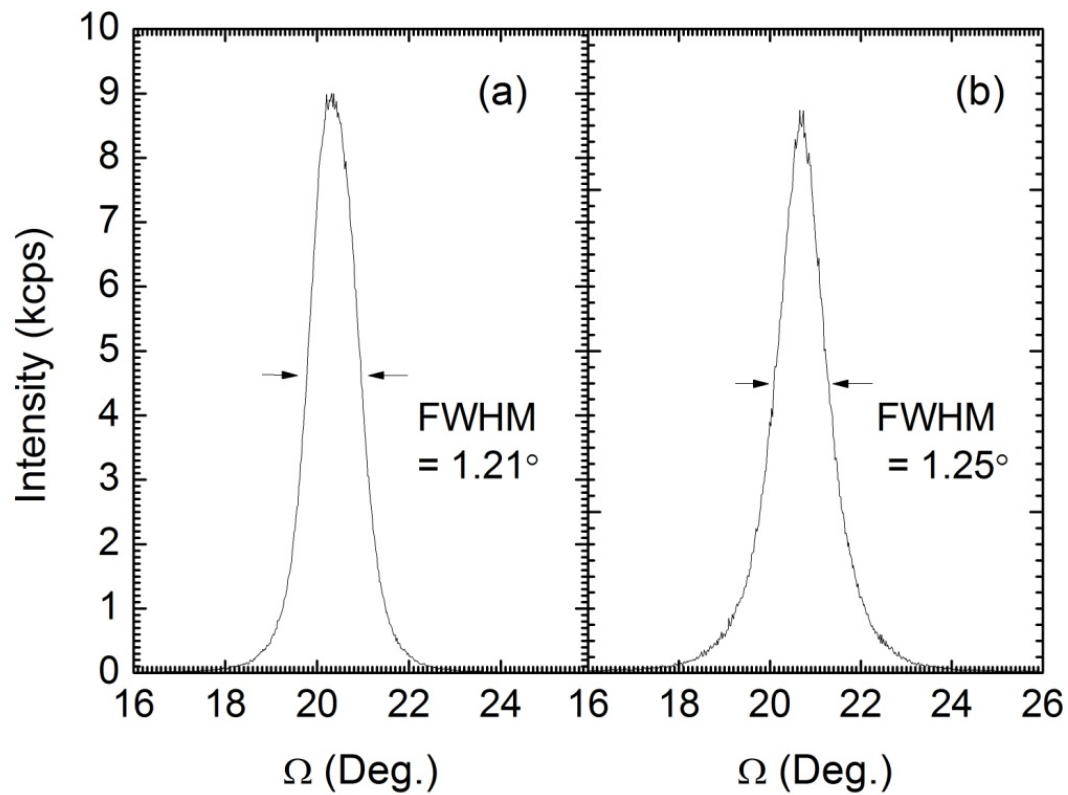


FIG. 23 Rocking curve scan for (111) peak of (a)  $\text{Fe}_{50}\text{Pt}_{45}\text{Rh}_5$  (50nm) and (b)  $\text{Fe}_{50}\text{Pt}_{25}\text{Rh}_{25}$  (50nm) sample. The full width of half maximum (FWHM) is indicated in the figure.

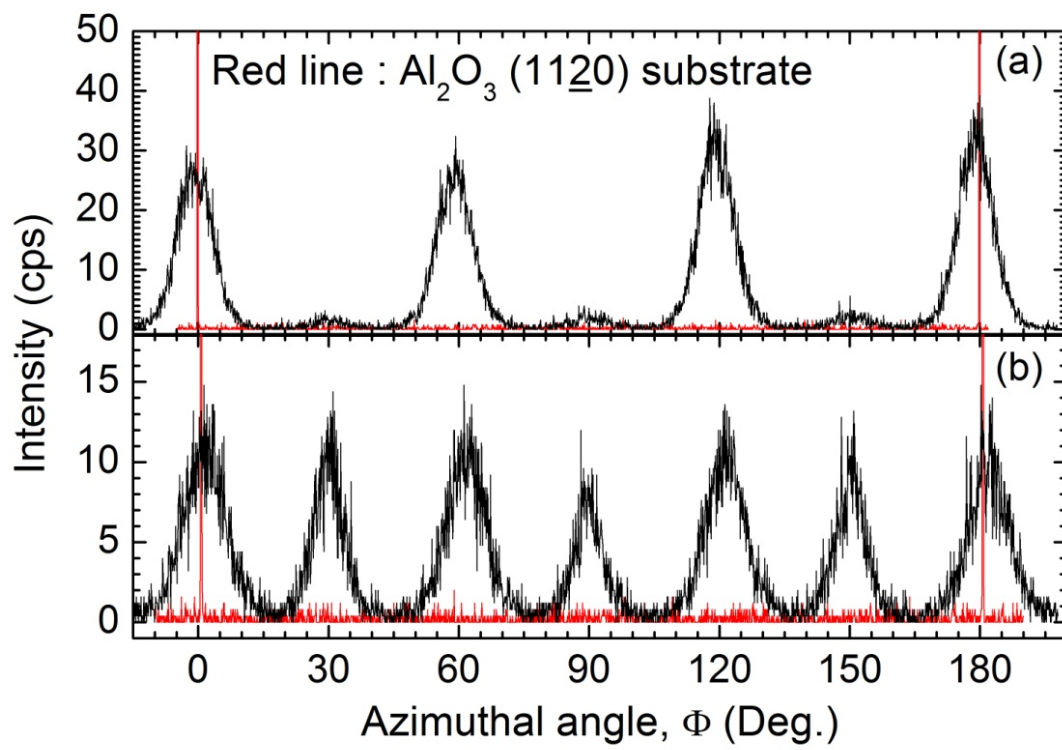


FIG. 24 The pole figure scan results for (111) of (a)  $\text{Fe}_{50}\text{Pt}_{45}\text{Rh}_5$  (50nm) and (b)  $\text{Fe}_{50}\text{Pt}_{25}\text{Rh}_{25}$  (50nm) sample. The  $\alpha\text{-Al}_2\text{O}_3$  (11 $\bar{2}$ 0) measured at the tilted angle  $\psi=60^\circ$  are plotted together in the red line.

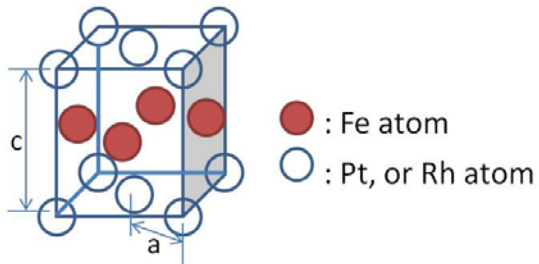
For  $\alpha$ -Al<sub>2</sub>O<sub>3</sub> (11 $\bar{2}$ 0) peak  $2\theta=37.777^\circ$ , the substrate is rotated at  $\Psi=60^\circ$  and scanned in the azimuthal angle direction. As expected in the hexagonal (110) plane, two fold symmetry is observed at around  $0^\circ$  and  $180^\circ$  in the red line in the FIG. 24.

In pole figure measurement, after first  $\Phi$  angle scan for  $\alpha$ -Al<sub>2</sub>O<sub>3</sub> (11 $\bar{2}$ 0),  $2\theta$  was re-adjusted at  $40.9412^\circ$  for FePt<sub>45</sub>Rh<sub>5</sub> (111) and  $40.3040^\circ$  for Fe<sub>50</sub>Pt<sub>25</sub>Rh<sub>25</sub> (111) without changing the sample position and at  $\Psi=70.53^\circ$ ,  $\Phi$  azimuthal angle is scanned. As seen in the FIG. 24, the 12-fold symmetric pole figure for Fe<sub>50</sub>Pt<sub>25</sub>Rh<sub>25</sub> (111) and the six fold symmetric pole for Fe<sub>50</sub>Pt<sub>45</sub>Rh<sub>5</sub> are observed. The observed six fold symmetry in (111) film growth for FCC (A1) structure is commonly observed for the twinning of the structure. The 12-fold peak in the 111 orientation is attributed to the existing domain structure rotated at  $30^\circ$  from the original six-fold symmetric position, which has been observed for other hexagonal plane [68]. The domain feature of Fe<sub>50</sub>Pt<sub>25</sub>Rh<sub>25</sub> peak is more profound than that of Fe<sub>50</sub>Pt<sub>45</sub>Rh<sub>5</sub> case where only the small peak between six fold symmetric peaks is observed.

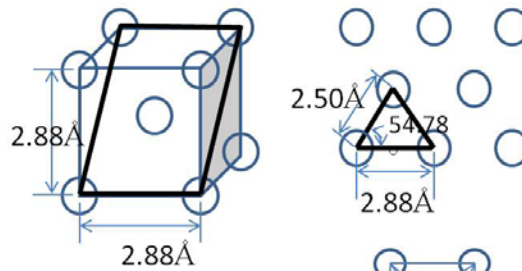
### C. The epitaxial relation between FePtRh, Cr, Pt and Al<sub>2</sub>O<sub>3</sub>

As studied in XRD experiment, the epitaxial film growth of FePtRh is confirmed. In XRD, the X-ray diffraction peak from all layers are observed and well characterized for the film quality and symmetric pole figure measurement. The epitaxy of each layer in the multilayered structure can be well understood under the consideration of the lattice spacing of each layer. The FIG. 25 shows the atomic structure of each layer -Pt, Cr seed layer, L1<sub>0</sub> FePtRh and substrate  $\alpha$ -Al<sub>2</sub>O<sub>3</sub> and the lattice spacing at each observed plane direction.

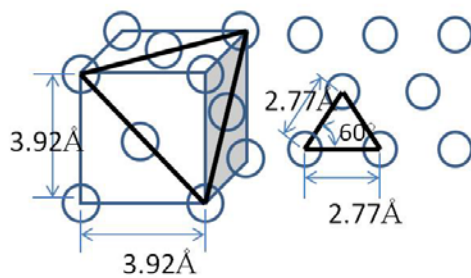
(a)  $\text{FePt}_{50-x}\text{Rh}_x$  L10 Structure



(c) Cr (110) plane



(b) Pt (111) plane



(d)  $\text{Al}_2\text{O}_3$   $[11\bar{2}0]$  plane

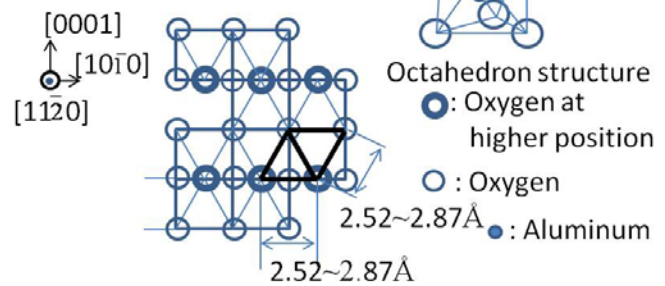


FIG. 25 The diagram for the lattice spacing of the plane of each layer (a)  $\text{L1}_0$  FePtRh, (b) Pt (111), (c) Cr (110) and (d)  $\alpha\text{-Al}_2\text{O}_3$   $[11\bar{2}0]$  plane.

In the FIG. 25 (d),  $\alpha$ - $\text{Al}_2\text{O}_3$  substrate plane is shown with oxygen atoms positioned in the  $[11\bar{2}0]$  direction [69].  $\alpha$ - $\text{Al}_2\text{O}_3$  structure can be understood as the assembly of the octahedron unit structure which is composed of aluminum on the center and three oxygen atoms on the top and bottom. In the  $[11\bar{2}0]$  direction, one side (triangle) of the octahedron is placed with slopes relative to the flat surface. Additionally, the shape of the triangle is distorted from that of a triangle of a hexagon due to the different oxygen spacing ( $2.52 \text{ \AA} \sim 2.87 \text{ \AA}$ ) inside the octahedron [69]. FIG. 25 (c) shows the body-centered cubic structure of Cr with (110) surface. In structure, Cr (110) surface has the distorted hexagonal atomic configuration where the lattice spacing and the angle between two atoms are  $2.50 \text{ \AA}$ ,  $2.88 \text{ \AA}$  and  $54.78^\circ$ . Therefore, Cr (110) is favored on  $\text{Al}_2\text{O}_3$  ( $11\bar{2}0$ ) in structure and lattice spacing. In the FIG. 25 (b), face-centered Pt cubic structure and Pt (111) plane is described. Pt (111) plane has the hexagonal structure which has  $2.77 \text{ \AA}$  atomic distance, which is close to the Cr (110) plane. The  $\text{L1}_0$  FePtRh structure shown in the FIG. 25 (a) is close to FCC (A1) Pt structure except the c axis direction is longer than the cubic lattice constant. Therefore, the epitaxial relation between layers is well understood.

#### D. X-ray diffraction for superlattice samples

In this work, the main interest is the interface property of the FePtRh multilayered structures which is only compositionally modulated for a different magnetic layer. The crystal structural property for the prepared  $[\text{Fe}_{50}\text{Pt}_{45}\text{Rh}_5 (10\text{nm})/\text{Fe}_{50}\text{Pt}_{25}\text{Rh}_{25} (20\text{nm})] \times 8$  film is first examined by XRD diffraction.

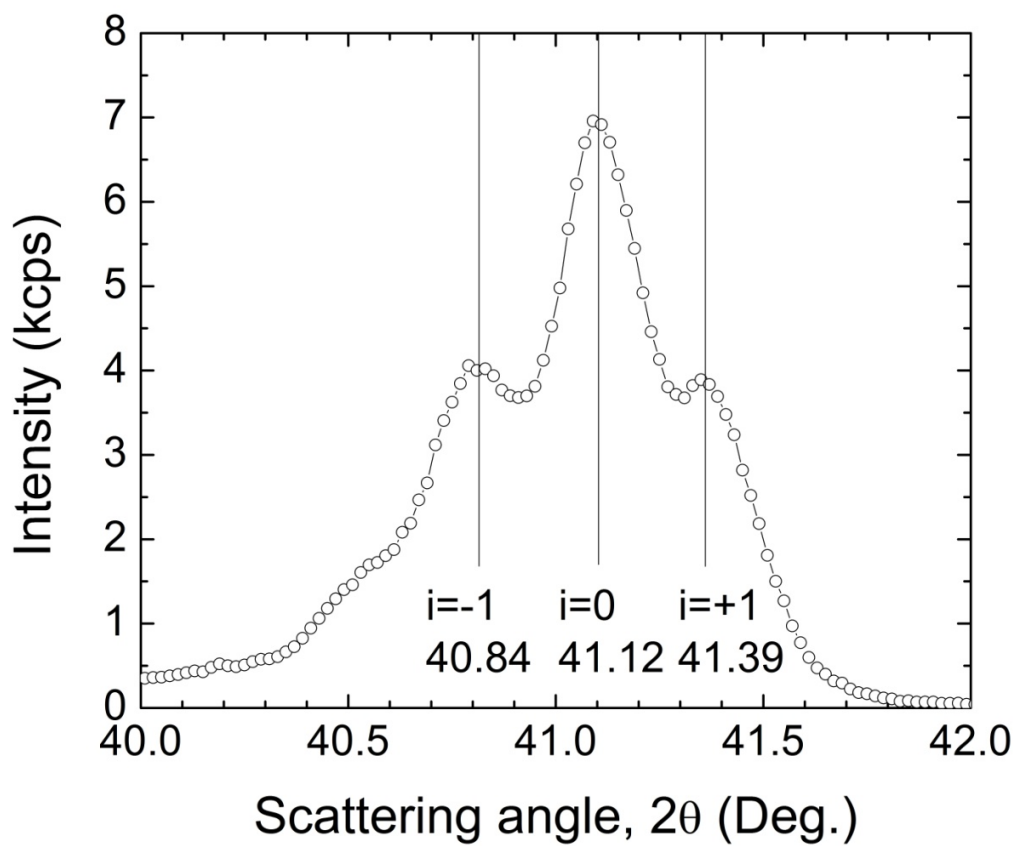


FIG. 26 The  $\theta$ - $2\theta$  scan results around FePtRh 111 position for superlattice  $[\text{Fe}_{50}\text{Pt}_{45}\text{Rh}_5$  (10nm)/ $\text{Fe}_{50}\text{Pt}_{25}\text{Rh}_{25}$  (20nm)]  $\times 8$  sample.

The main characteristic of XRD data of superlattice structure is the existence of the satellite peak appearance in  $\theta$  - $2\theta$  scan data. The FIG. 26 shows the averaged (111) peak of two Fe<sub>50</sub>Pt<sub>45</sub>Rh<sub>5</sub> (10nm) and Fe<sub>50</sub>Pt<sub>25</sub>Rh<sub>25</sub> (20nm) layers. Around the main peak of (111) direction, first-order two satellite peaks are indexed at 40.84° and 41.39°  $2\theta$  position. The satellite peak position in the XRD data is directly related to the periodicity of the modulated A-B superlattice structure. The periodicity of superlattice structure in XRD can be characterized by the following equation (22) [70, 71].

$$2 \frac{\sin\theta}{\lambda_x} = \frac{1}{\bar{d}} \pm \frac{n}{\Lambda} \quad (22)$$

In the equation (22),  $\theta$  is the main peak angle,  $\lambda_x$  is the x-ray wavelength,  $\bar{d}$  is the average lattice spacing of the superlattice,  $n$  is the order of the satellite peak and  $\Lambda$  is the modulation wavelength of the superlattice. The calculated period  $\Lambda$  of the superlattice from the satellite peak position is 34.9nm, 33.6nm respectively and it is consistent with the expected thickness 30nm which is calculated by the deposition flux rate. The observed satellite peak indicates the existence of the periodic bilayered structure. The chemical structure is more examined in transmission electron microscopy (TEM) experiment. The FIG. 27 shows the image measured by HAARF-STEM technique which provides the high atomic number ( $Z$ ) contrast. As seen in the FIG. 27, the clear image contrast between Fe<sub>50</sub>Pt<sub>45</sub>Rh<sub>5</sub> and Fe<sub>50</sub>Pt<sub>25</sub>Rh<sub>25</sub> layer indicates the separate Pt and Rh concentration for each layer and the well-defined interface. Therefore, the chemical interface between Fe<sub>50</sub>Pt<sub>45</sub>Rh<sub>5</sub> and Fe<sub>50</sub>Pt<sub>25</sub>Rh<sub>25</sub> layers are concluded here.

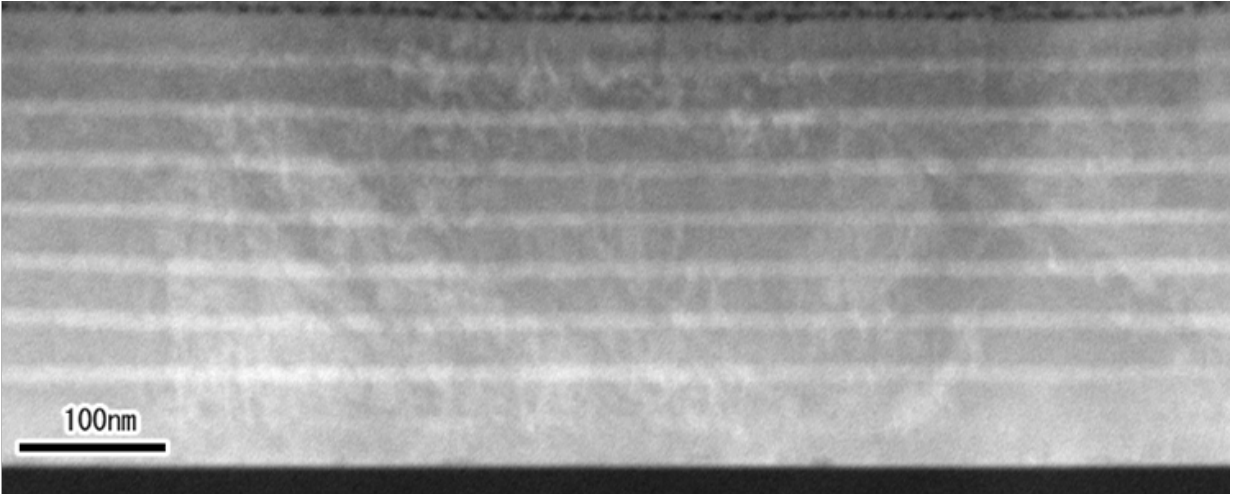


FIG. 27 Transmission electron microscopy image for superlattice FePtRh sample measured by HAADF

#### E. Magnetic property of FePtRh superlattice structure

With the observation of the well defined interface results, the magnetic property is investigated here. The FIG. 28 shows the SQUID magnetometry results for superlattice  $[\text{Fe}_{50}\text{Pt}_{45}\text{Rh}_5 (10\text{nm})/\text{Fe}_{50}\text{Pt}_{25}\text{Rh}_{25} (20\text{nm})] \times 8$  sample measured at 5K, 150K, 300K. At 300K, 150K, the measured hysteresis loops show the symmetric coercivity values – 3kOe, 4.8kOe and the magnetizations, 340emu/cc, 500emu/cc, respectively. On the other hand, 5K hysteresis loop shows the asymmetric values, -8.9kOe and 8.5kOe with 570emu/cc magnetization. The asymmetric coercivity indicates the exchange coupling between ferromagnetic and antiferromagnetic FePtRh layers. In hysteresis loop, the saturation magnetic field is increasing and the abrupt magnetization change also appears around zero applied magnetic field region as the temperature decreases, which indicates the reduced thermal effect of FePtRh ferromagnetic layer and the enhanced exchange coupling at the interface between ferromagnetic and antiferromagnetic layers of FePtRh. The magnetic modulation feature of the superlattice structure is well justified in the polarized neutron reflectivity where the separate magnetic contribution is distinguished in the reflectivity data. FIG. 29 shows the polarized neutron reflectivity results measured at 250K temperature with 1.15T applied field. As shown in FIG. 29, two strong Bragg peaks are clearly observed in the reflectivity for spin++ channels while the small Bragg peak intensity exists in the reflectivity of spin - - channels, which implies the existence of the modulated magnetic structure in superlattice. The existence of the repetitive ferromagnetic layers FePtRh is well described in the scattering length density (SLD) depth profiles which is estimated from the fitting by Parratt recursion relation for two spin channels as seen in the FIG. 30. The periodic oscillatory profile of SLD difference between two spin

channels represents the existing ferromagnetic FePtRh layers. The period of the oscillation is 32nm which is a consistent value as the previous XRD result. The nuclear and magnetic SLD in the FIG. 30 is roughly estimated in the fitting as the less value than the expected value from the bulk FePtRh which is attributed to the deformed lattice structure and the present domain structure observed in the XRD result.

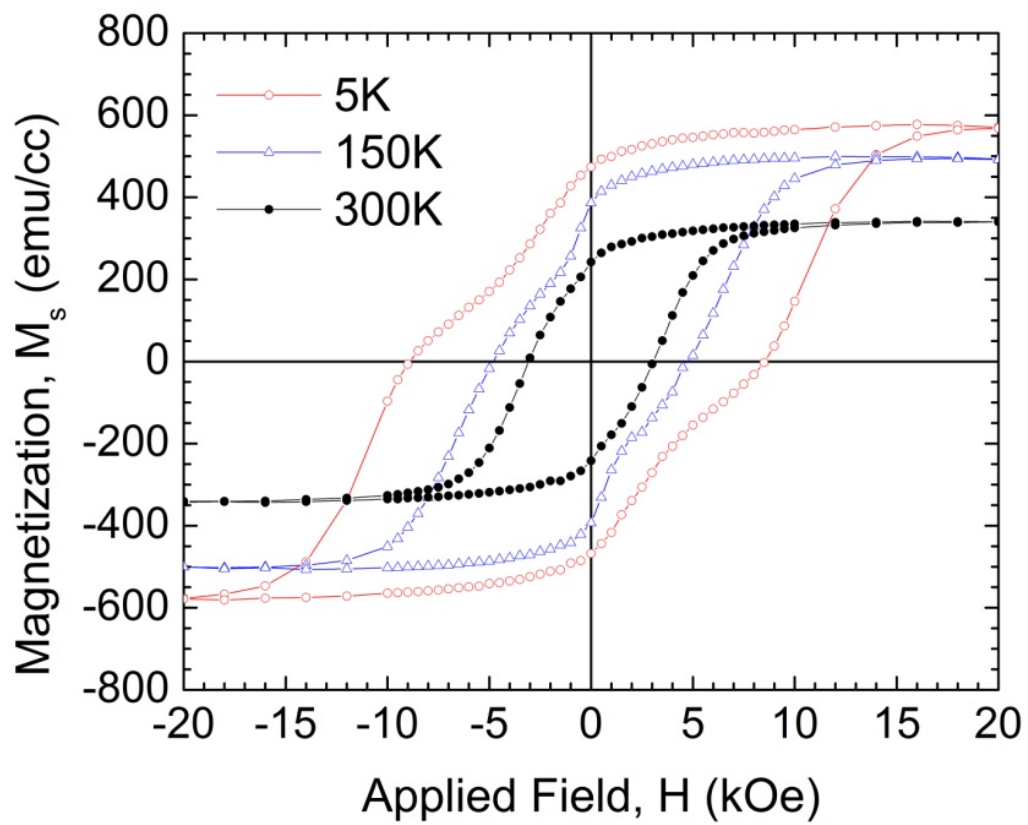


FIG. 28 SQUID result for superlattice  $[\text{Fe}_{50}\text{Pt}_{45}\text{Rh}_5 (10\text{nm})/\text{Fe}_{50}\text{Pt}_{25}\text{Rh}_{25} (20\text{nm})] \times 8$  sample measured at 5K, 150K, 300K.

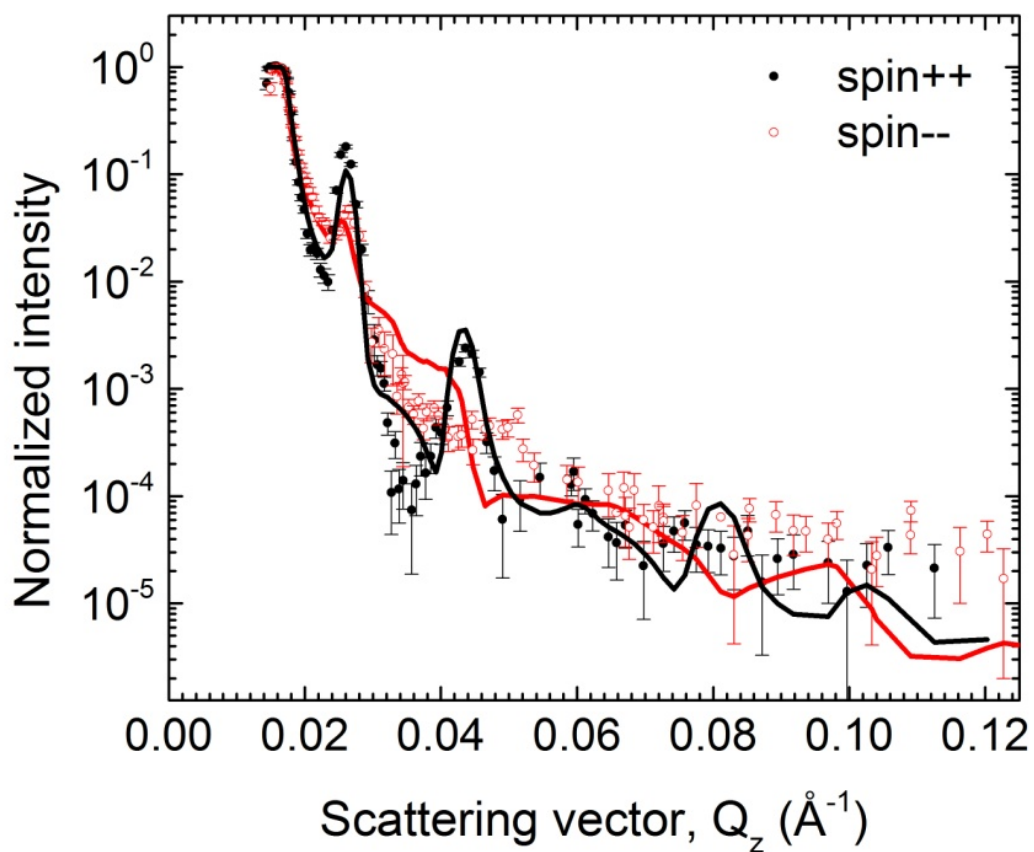


FIG. 29 The polarized neutron reflectivity of  $[\text{Fe}_{50}\text{Pt}_{45}\text{Rh}_5$  (10nm)/  $\text{Fe}_{50}\text{Pt}_{25}\text{Rh}_{25}$  (20nm)]  $\times 8$  measured at 250K with 1.15T applied field during field cooling for two spin channels.

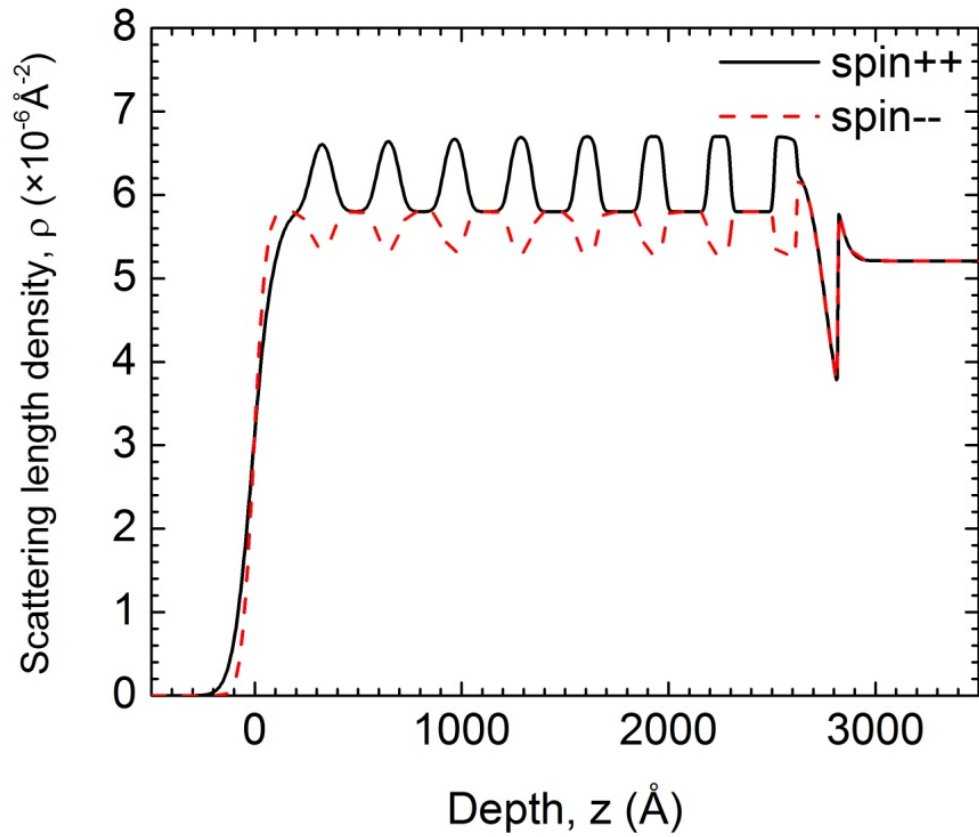


FIG. 30 Scattering length density obtained from the fitting of the polarized neutron reflectivity of FePtRh superlattice structure for two spin channels.

## V. FeRhPd MULTILAYERED SYSTEM

### A. EXPERIMENTAL DETAILS

All films are prepared by DC magnetron sputtering techniques with a base pressure less than  $1 \times 10^{-8}$  torr in ultra high vacuum (UHV) condition. For epitaxial thin film growth, the crystallographic relation between seed layer and the film is very critical. For the epitaxial thin film growth in the (111) FCC (A1)-orientation, the new buffer layer rhodium on sapphire substrate is studied and applied. To verify the epitaxial relation of Rh with sapphire, Rh (20nm) was grown on a-plane  $\alpha$ -Al<sub>2</sub>O<sub>3</sub> (11 $\bar{2}$ 0), c-plane  $\alpha$ -Al<sub>2</sub>O<sub>3</sub> (0001), m-plane  $\alpha$ -Al<sub>2</sub>O<sub>3</sub> (10 $\bar{1}$ 0) substrates. During deposition, the sapphire substrate is heated at 600°C. The deposition flux rate is adjusted to 0.146Å/s. Additionally, Rh (20nm) at 500°C, Rh (40nm, 80nm) at 600°C on a-plane  $\alpha$ -Al<sub>2</sub>O<sub>3</sub> (11 $\bar{2}$ 0) are prepared to examine the thickness and temperature dependence. For the prepared Rh samples, X-ray reflectivity (XRR), X-ray diffraction (XRD)  $\theta$ -2 $\theta$  scan are performed. In this work, all XRD related measurements are performed by Philips instrument equipped with Cu K $\alpha_{1,2}$  source. For the observed Rh (111) peak, rocking curve, pole figure are measured to confirm ordering and epitaxy. For FeRhPd thin film growth, Fe<sub>46</sub>Rh<sub>48</sub>Pd<sub>6</sub> alloy target is sputtered with the substrate at the elevated growth temperature. The epitaxial FeRhPd (50nm) films are prepared with Pt (10nm) seed and Pt(6nm) capping layers on Rh (10nm)/ a-plane  $\alpha$ -Al<sub>2</sub>O<sub>3</sub> (11 $\bar{2}$ 0), at four different 400°C, 500°C, 600°C, 700°C growth temperatures to investigate the structural ordering influence on the magnetic phase transition. For the reduced dimensional effect on the magnetic phase transition, various thicknesses (10nm, 20nm, 30nm, 40nm, 50nm) of FeRhPd samples are also prepared with the same seed and capping layers as

above at 600°C. In this work, one concern is the magnetic phase transition of magnetically coupled multilayer structures. To investigate any magnetic coupling effect on FeRhPd magnetic phase transition, the epitaxial [FeRhPd(25nm) / Pt(0.5nm) / FeRhPd(25nm)] tri-layered structure is selected and prepared as in the same seed and capping layers at 600°C growth temperature. For all prepared FeRhPd samples, the film structure is examined by X-ray diffraction  $\theta$ - $2\theta$  specular scan and off-specular (rocking curve) scan. For tri-layered FeRhPd, additional pole figure measurements are performed for the observed diffraction peak. The temperature dependent magnetization of all FeRhPd samples are evaluated by quantum design magnetic property measurement system (MPMS) integrated with superconducting quantum interference device (SQUID) within 5K~350K temperature range. In SQUID, the field dependent feature is examined by cooling and heating with different applied magnetic field. For the measurement, the sample is cooled down to 5K with zero applied magnetic field to distinguish any field dependent feature [72, 73]. Then, with the applied 1T field, the sample is heated up to 350K and cooled down to 5K. All the background signals from the substrate are subtracted after measurement with the consideration of the substrate weight. For the tri-layered FeRhPd sample, polarized neutron reflectivity technique is applied to identify the magnetic depth profile of each FeRhPd layer during metamagnetic phase transition. The polarized neutrons which have 1~5Å wavelength from the Spallation Neutron Source are introduced to the sample which is mounted on the Cu sample stage equipped with the closed cycle cooling system isolated under vacuum. The reflected two spin-polarized neutrons with non-spin flip are measured respectively at three different low angles. The measured reflectivity data are integrated for the broadened transverse component, compared to the direct beam profile to differentiate the reflected beam, normalized for the total reflection near the critical scattering vector and combined together with three data

sets measured at different scattering vector range. In the measurement, several temperatures - 450K, 350K, 300K, 5K are selected based on the information of the previously measured thermal hysteresis of magnetization with respect to temperature for FeRhPd tri-layered sample. Each temperature is reached according to the cooling and heating hysteresis with the constant applied external field of 1T. The additional PNR is measured at 350K with 0.005T applied field to verify any field dependent effect in magnetic phase transition.

## B. RESULTS AND DISCUSSION

### 1. Rh seed layer growth and characterization

For rhodium thin films prepared on sapphire substrate, the crystal structure is examined by X-ray diffraction technique. Previously, the crystallographic 111 orientation of Rh on a-plane sapphire case has been observed and studied for 100nm thick Rh film grown at the relatively low growth temperature  $T (\leq 500^{\circ}\text{C})$  region at the base pressure  $P < 5 \times 10^{-8}$  torr [74, 75]. In FIG. 31, X-ray diffraction  $\theta$ - $2\theta$  scan results are presented for thin Rh 20nm films grown on m-plane (10 $\bar{1}$ 0), a-plane (11 $\bar{2}$ 0), c-plane (0001)  $\alpha$ -Al $_2$ O $_3$  substrates at 600 $^{\circ}$ C which is close to the optimal temperature (580 $^{\circ}$ C ~ 590 $^{\circ}$ C ) for the epitaxial Pt film growth [35, 36]. For m-Al $_2$ O $_3$  (10 $\bar{1}$ 0) substrate case, no peak was observed as in the first graph. On the other hand, strong Rh (111), (222) peaks are seen for a-Al $_2$ O $_3$  (11 $\bar{2}$ 0), c-aAl $_2$ O $_3$  (0001) substrates with additional Laue oscillatory peak besides the main peak, which indicates the high quality of epitaxy. As verified in Pt case which has the same FCC (A1) structure and the close lattice spacing as Rh, c-plane of  $\alpha$ -Al $_2$ O $_3$  provides the good epitaxial relation with (111)-oriented FCC structure.

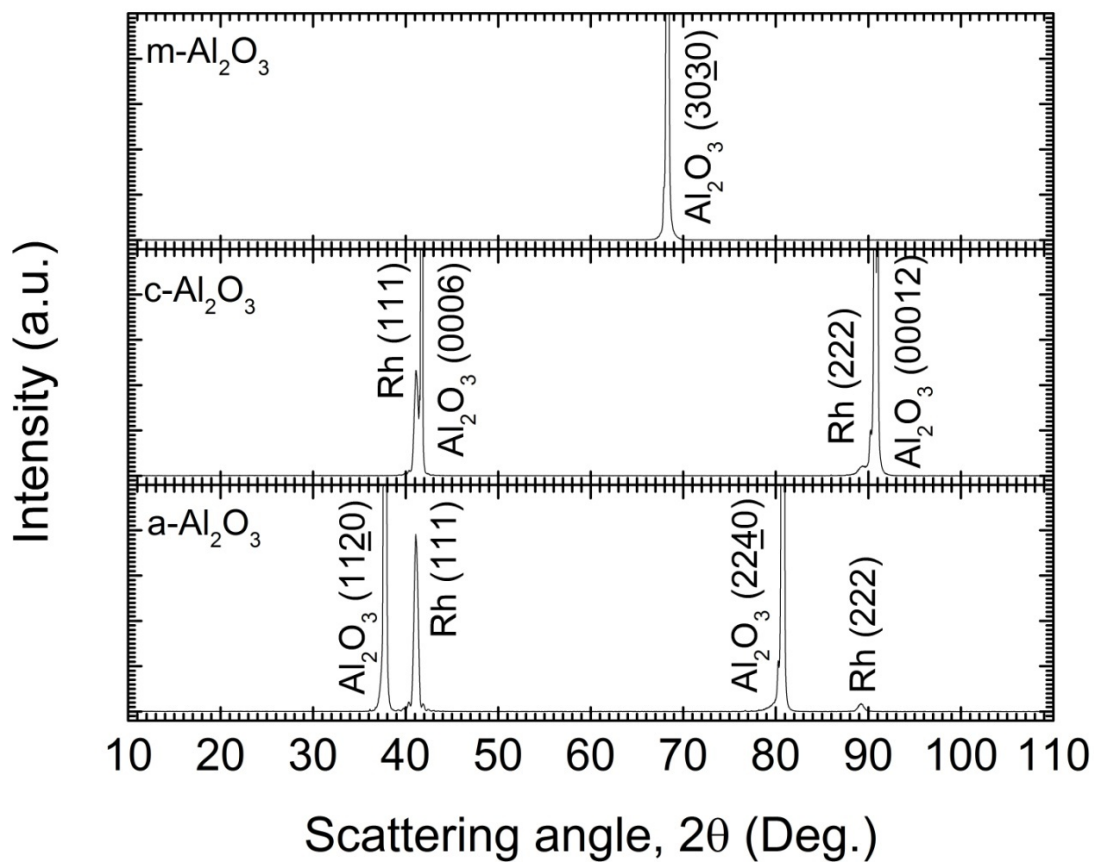


FIG. 31 X-ray diffraction  $\theta$ - $2\theta$  scan for Rh(20nm) grown on m-plane  $\alpha$ - $\text{Al}_2\text{O}_3$  (10 $\bar{1}$ 0), c-plane  $\alpha$ - $\text{Al}_2\text{O}_3$  (0001), and a-plane  $\alpha$ - $\text{Al}_2\text{O}_3$  (11 $\bar{2}$ 0) substrate at 600°C.

The roof top structure of a-plane of  $\alpha$ -Al<sub>2</sub>O<sub>3</sub> also shows the close lattice spacing as the hexagonal shape of (111)-oriented FCC (A1) Rh. On the other hand, in m-plane  $\alpha$ -Al<sub>2</sub>O<sub>3</sub>, Al ions are located in the rectangular position which supports the preferred 110-orientation for MgO case [76]. Thus, the observed XRD results in the FIG. 31 are well understood in the crystallographic orientation relation between Rh layer and  $\alpha$ -Al<sub>2</sub>O<sub>3</sub> substrate.

The film structural depth profile is well justified in X-ray reflectivity (XRR). FIG. 32 shows the XRR results for Rh (20nm) grown at 600°C, 500°C on a-plane (11 $\bar{2}$ 0) and m-plane (10 $\bar{1}$ 0), c-plane (0001)  $\alpha$ -Al<sub>2</sub>O<sub>3</sub> substrates at 600°C. In case of Rh on c-plane (0001), a-plane (11 $\bar{2}$ 0)  $\alpha$ -Al<sub>2</sub>O<sub>3</sub> in the FIG. 32, clear Kiessig oscillation are observed up to higher angle region, which represents the smoother film surface at the film boundary while XRR for Rh on a-Al<sub>2</sub>O<sub>3</sub> (11 $\bar{2}$ 0) at 500°C shows less oscillatory behavior, which implies the relatively rougher surface than 600°C case. For Rh 20nm thin layer on m-Al<sub>2</sub>O<sub>3</sub> (10 $\bar{1}$ 0), Kiessig oscillation quickly decreases after the first Bragg peak which reflects relatively rougher surface than those of c-, m-plane  $\alpha$ -Al<sub>2</sub>O<sub>3</sub> cases. The roughness and thickness information is estimated quantitatively in XRR fitting. In case of (2), (3) in the FIG. 32, the Rh layer thickness is ~18nm, ~17.3nm, and the roughnesses are ~0.48nm, ~0.4nm at the interface between Al<sub>2</sub>O<sub>3</sub> and Rh film, and ~0.23nm, ~0 nm at the boundary of Rh and air, respectively. In case of (4), the Rh thickness is ~17.9nm, and the interface roughness is ~0.61nm between Al<sub>2</sub>O<sub>3</sub> and Rh and ~0 nm between Rh and air. On the other hand, m-plane  $\alpha$ -Al<sub>2</sub>O<sub>3</sub> (10 $\bar{1}$ 0) substrate case plotted in (1) shows the higher roughness ~3.5nm between Rh and air with 16.5nm thickness.

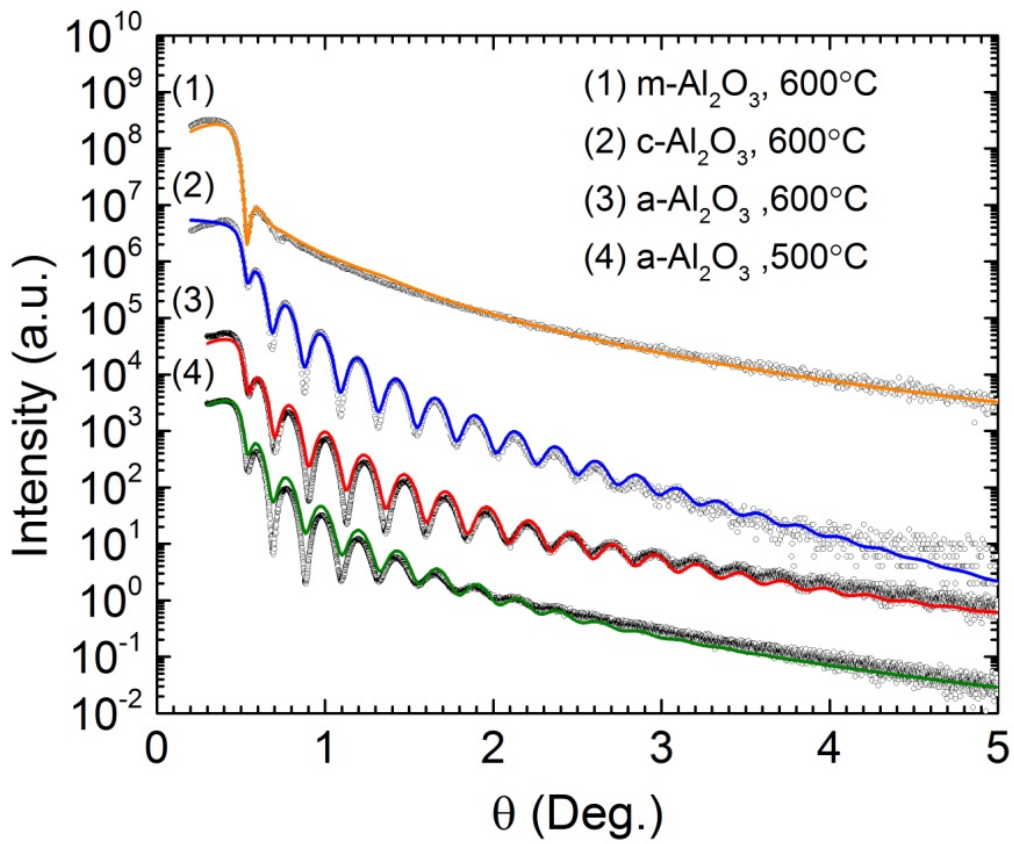


FIG. 32 X-ray reflectivity of Rh (20nm) on (1) m-plane  $\alpha\text{-Al}_2\text{O}_3(0001)$  grown at  $600^\circ\text{C}$  (2) c-plane  $\alpha\text{-Al}_2\text{O}_3(0001)$  grown at  $600^\circ\text{C}$  , (3) on a-plane  $\alpha\text{-Al}_2\text{O}_3(11\bar{2}0)$  grown at  $600^\circ\text{C}$  and (4)  $500^\circ\text{C}$

Therefore, smoother Rh (20nm) is achieved on a-plane (11 $\bar{2}$ 0), c-plane  $\alpha$ -Al<sub>2</sub>O<sub>3</sub> (0001) substrate at 600°C growth temperature than the case of 500°C.

The epitaxial feature of Rh (20nm) grown on a-plane and c-plane  $\alpha$ -Al<sub>2</sub>O<sub>3</sub> is examined in the pole figure measurement. The FIG. 33 shows the azimuthal angle scan results in XRD for the highly symmetric Rh (111) peak and substrate  $\alpha$ -Al<sub>2</sub>O<sub>3</sub> peak for the Rh (20nm) grown on (a) a-plane and (b) c-plane  $\alpha$ -Al<sub>2</sub>O<sub>3</sub> at 600°C growth temperature. In FIG. 33 (a), the Rh 111 shows the six-fold symmetric sharp poles repeated with 60° interval which is commonly observed for 111-oriented FCC (A1) structure due to the twinning of the stacking. The 2-fold symmetric peaks for a-plane Al<sub>2</sub>O<sub>3</sub> (11 $\bar{2}$ 0) indicates the relative orientation between Rh (111) and a-plane Al<sub>2</sub>O<sub>3</sub> (11 $\bar{2}$ 0). The narrow width of Rh peaks also represents the high quality of 111-oriented epitaxy of Rh film. For the case of Rh(111) on c-plane  $\alpha$ -Al<sub>2</sub>O<sub>3</sub>, the additional peaks between six-fold symmetric poles are observed in the FIG. 33 (b). The appearance of the additional small peak which provides the 12-fold symmetry has been interpreted as the present domain structure which is rotated at 30° for the original six-fold symmetric position, which was observed in case of FePtRh (111) growth in the previous chapter [68]. As indicated in the In FIG. 31, the existence of the high quality of epitaxy was observed as a form of the oscillatory behavior of Rh (111) peak in XRD measurement. In the logarithmic scale, Laue oscillatory behavior of Rh 111 peak is observed more profoundly. FIG. 34 (a) shows the  $\theta$ -2 $\theta$  scan results plotted for Rh (111) on a-plane and c-plane  $\alpha$ -Al<sub>2</sub>O<sub>3</sub> substrates in the logarithmic scale about Rh (111) peak with respect to the scattering vector in the perpendicular direction to the film. The observed Laue oscillation around Rh (111) peak represents the coherent scattering of an appreciable small crystal.

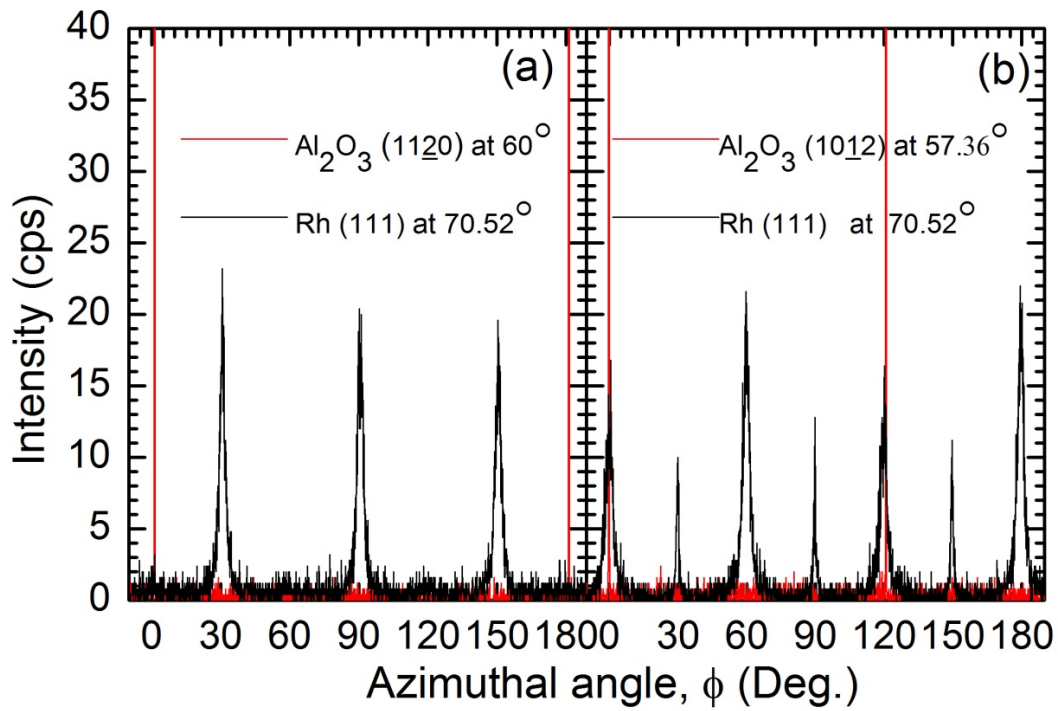


FIG. 33 The pole figure of Rh (20nm) sample grown on (a) a-plane and (b) c-plane  $\alpha\text{-Al}_2\text{O}_3$ . Each peak is measured in the azimuthal angle scan for Rh (111) and  $\text{Al}_2\text{O}_3$  (a) (1120), (b) (1012) at the tilted angle  $\psi$  with respect to the perpendicular direction to the film plane as designated in the graph.

The Laue oscillation around the diffraction peak has been observed in several samples which were prepared usually by molecular beam epitaxy (MBE) methods. In the FIG. 34 (a), the period of the oscillation can be approximated to obtain the contributing portion of the film. For Rh on a-plane  $\alpha$ -Al<sub>2</sub>O<sub>3</sub> case (1) in the FIG. 34 (a), the estimated thickness 17.1nm shows the consistent value as the film thickness of Rh layer 17.3nm in XRR, which indicates that the main mechanism of the Laue oscillation is dominant over the film.

The off-specular diffraction (rocking curve) was measured for Rh (111) diffraction peak as shown in the FIG. 34 (b). The rocking curve scan ( $Q_x$ ) shows the two components –sharp and broad peaks in c-plane and a-plane  $\alpha$ -Al<sub>2</sub>O<sub>3</sub> cases. The sharp peak in the rocking curve has been considered as the indication of the existence of the coherent portion of thin film with  $\alpha$ -Al<sub>2</sub>O<sub>3</sub> substrate plane. Especially, this kind of feature has been known for many thin film systems on sapphire substrate which is an issue to grow the high quality epitaxial film growth in the thin film research [32, 77, 78]. Near the high quality epitaxy, the broadened additional peak profile has been attributed to the misfit dislocation in the translational direction to the surface.

Theoretically, there has been an effort to model the exact profiles of the existing misfit dislocation [79-81]. The intensity profile can be approximately fitted by Gaussian shape. For the narrow peak, the full width of half maximum (FWHM) of a-plane  $\alpha$ -Al<sub>2</sub>O<sub>3</sub> case is 0.040° in  $\Delta$ , (0.0194nm<sup>-1</sup> in  $\Delta Q_x$ ), and 0.72 in  $\Delta$ (0.36nm<sup>-1</sup> in  $\Delta Q_x$ ) for the broad peak. For c-Al<sub>2</sub>O<sub>3</sub> case,  $\Delta$  is 0.041° (0.020nm<sup>-1</sup> for  $\Delta Q_x$ ) for the narrow peak and the broad part has 0.78° in  $\Delta$ (0.39nm<sup>-1</sup> in  $\Delta Q_x$ ). To study the behavior of the narrow peak, two more different thicknesses 40nm, 80nm of Rh sample was prepared at the same growth condition as 20nm sample.

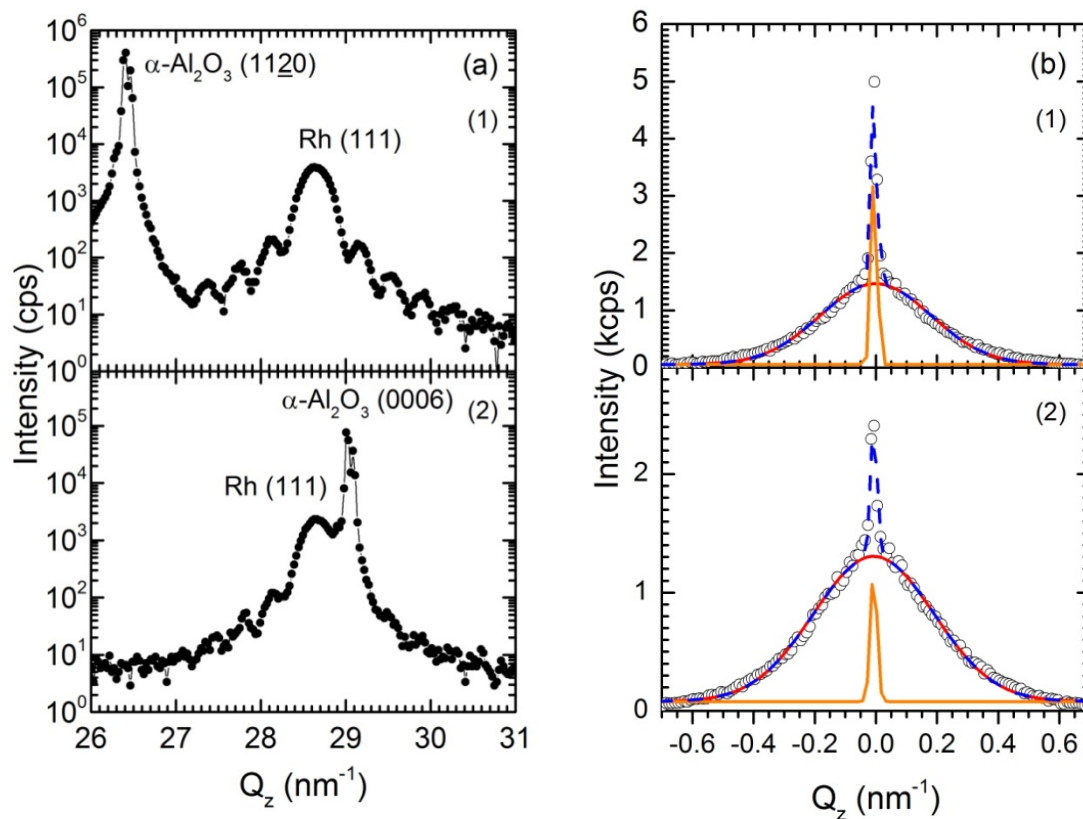


FIG. 34 (a) X-ray diffraction (plotted in logarithmic scale) and (b) off-specular (rocking curve) scan result for Rh(111) of Rh (20nm) on (1) a-plane  $\alpha\text{-Al}_2\text{O}_3$ (1120) and (2) c-plane  $\alpha\text{-Al}_2\text{O}_3$ (0001) planes grown at 600°C. The dotted blue line in (b) is the integrated fitting line by two Gaussians (red and orange line)

The FIG. 35 (a) shows the rocking curve scan results for Rh (111) peak. As the Rh layer becomes thicker, the narrow peak portion is reduced and at 80nm, it disappears totally. At the same time, the full width of half maximum (FWHM) of the broad part of rocking curve approaches the finite value as seen in the FIG. 35 (b), as the film thickness increases. The disappearance of the coherent sharp peak with the increasing film thickness is consistent with the theoretical explanation of the misfit dislocation mechanism in the epitaxial film, where the increase in dislocation density causes loss of correlation as the film thickness increases and finally, the Gaussian shape of the broad peak dominates and the coherent peak disappears [82]. Therefore, it is concluded that the high quality of the epitaxial 111-oriented Rh thin film on a-plane  $\text{Al}_2\text{O}_3$  (11 $\bar{2}$ 0) at 600°C growth temperature are achieved with the minimum roughness and misfit dislocation defect.

## 2. Single layer FeRhPd

The chemical structure and ordering in the epitaxial film growth is strongly dependent on the growth temperature. The structural characteristic of thin film on the magnetic phase transition can be examined by varying the growth temperature during the epitaxial film growth. Epitaxially-grown FeRhPd films on Pt(10nm) / Rh(10nm) / a-plane  $\alpha\text{-Al}_2\text{O}_3$  (11 $\bar{2}$ 0) at various growth temperatures are investigated by X-ray diffraction experiment. The FIG. 36 shows XRD results for FeRhPd (50nm) films grown at 400°C, 500°C, 600°C, 700°C temperatures.

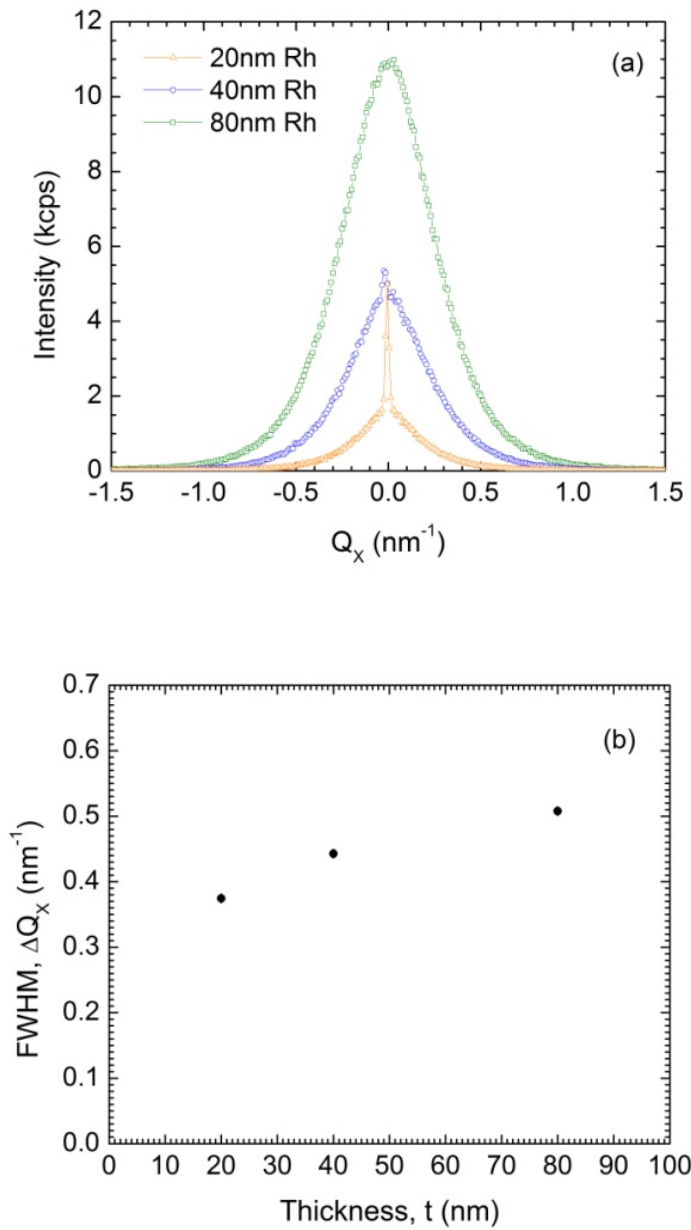


FIG. 35 (a) Off-specular (rocking curve) scan result for Rh(111) of Rh (20nm, 40nm, 80nm) on a-plane  $\alpha\text{-Al}_2\text{O}_3(11\bar{2}0)$  grown at  $600^\circ\text{C}$  (X-ray source :  $\text{Cu K}\alpha_{1,2}$ ) and (b) full width of half maximum of the broad peak in figure (a) with respect to Rh film thickness.

All diffraction peaks are observed around  $38\sim 44^\circ$ ,  $83\sim 95^\circ$   $2\theta$  scattering angle regions. Due to the close lattice spacing between Pt, Rh, FeRhPd, all diffracted intensities are closely located and shows the merged feature. Each diffraction peak originated from FeRhPd layer is identified by Gaussian multi-peak fitting and the fitting result is summarized in Table I. Separate diffraction peak is more distinguishable for the superstructure peak around  $83\sim 95^\circ$   $2\theta$  region as indicated in the inset of FIG. 36. Three diffraction peaks of FeRhPd are clearly observed in addition to FCC(A1) Pt (222), Rh(222) peaks for the case of  $600^\circ\text{C}$ ,  $700^\circ\text{C}$  growth temperature. In case of FeRh system, it has been noted that the FeRh film has  $\alpha'$ ,  $\gamma$  two phases when Rh ratio is within 49 ~59 at.% range [21]. Three diffraction peaks of FeRhPd are clearly observed in addition to FCC(A1) Pt (222), Rh(222) peaks for the case of  $600^\circ\text{C}$ ,  $700^\circ\text{C}$  growth temperature. In case of FeRh system, it has been noted that the FeRh film has  $\alpha'$ ,  $\gamma$  two phases when Rh ratio is within 49 ~59 at.% range [21]. In bulk Pd-doped FeRh case, two separate B2,  $L1_0$  structures in the phase diagram with respect to the temperature and compositions [11], or the coexisting phase of B2, FCC(A1) for as cast FeRhPd sample has been reported before [25]. Three diffraction peaks in the inset of FIG. 36 are interpreted as one  $L1_0$  close to FCC (A1) (222) and two B2 (220) peaks, one of which has slightly different lattice spacing (labeled by B2' in the inset), and they are all discussed with XRD results for film growth condition and the thickness dependence. The proportional dependence of the diffraction intensity with respect to the growth temperature suggests the developing structural formation in epitaxy for all layers of films. .At  $400^\circ\text{C}$ , the least intensive peak of Rh, Pt seed layers represents the relatively rough and partially-ordered 111-oriented seed layer as well as the less mobility of atoms during epitaxial film growth which results in the partially ordered structure of FeRhPd layers as seen with the small intensity for B2 FeRhPd peak.

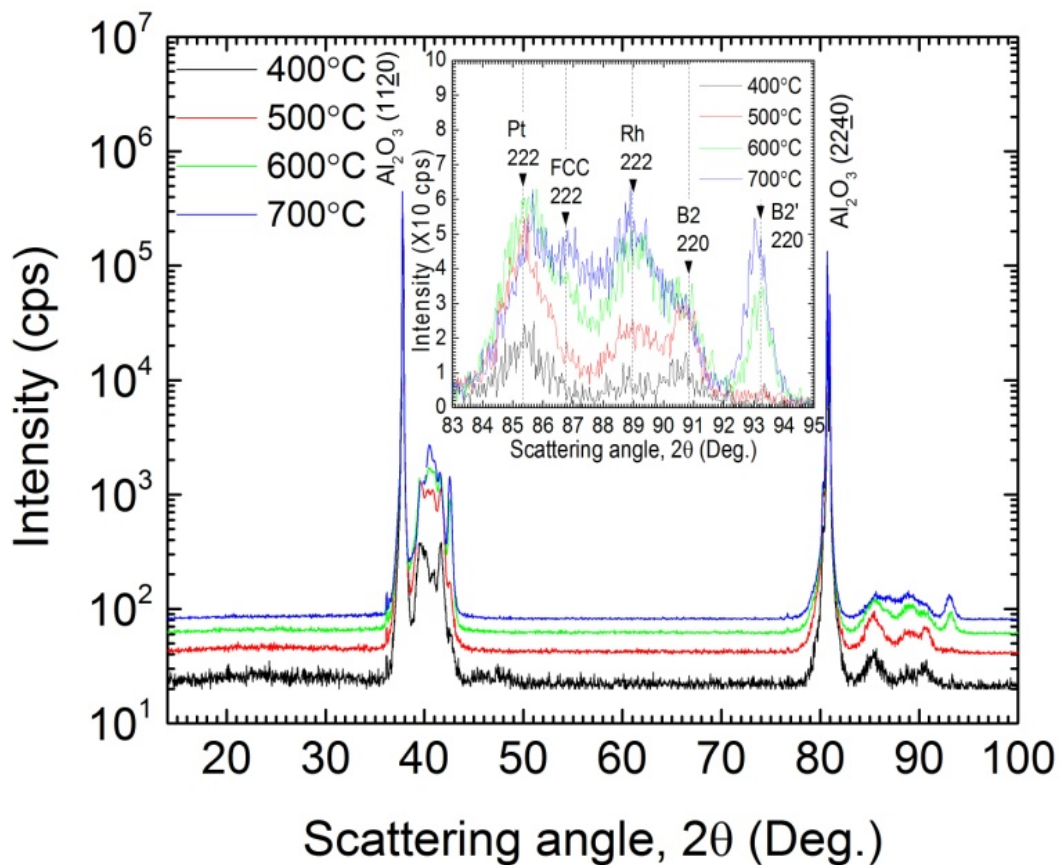


FIG. 36 X-ray diffraction  $\theta$ - $2\theta$  scan for FeRhPd(50nm) films on Pt(10nm)/Rh(10nm)/ $\alpha$ -Al<sub>2</sub>O<sub>3</sub>(1120) substrate with Pt(6nm) capping grown at 400°C, 500°C, 600°C, 700°C. Each plot is shifted to clarify each diffraction pattern. The inset inside the figure shows the linear-scale plot of each diffraction peak at 83°~95° angle.

As the growth temperature is elevated up to 500°C, B2 peak becomes more intensive with stronger Pt, Rh peaks. At 600°C, new FeRhPd B2 peak which has the slightly different lattice constant appears with distinguishable FeRhPd FCC (A1) peaks between Pt (222) and Rh (222) peaks together. Finally, all diffraction peaks are maximized at 700°C growth temperature. In Table I, the calculated lattice constant of FeRhPd from the diffraction peaks are 3.05Å ~3.07Å, 3 Å for B2, B2' and 3.87~3.89Å for FCC(A1)-like L1<sub>0</sub> and all the values are consistent for all samples. For 400° C, 500° C cases, L1<sub>0</sub> FeRhPd (111) peak was still observed while FeRhPd L1<sub>0</sub> (222) disappeared. The observed (111), (222) peak which is considered from L1<sub>0</sub> FeRhPd 600°C, 700°C cases must be distinguished from that of the disordered phase FCC(A1) at 400° C, 500° C cases. The different magnetic states between two cases are clearly observed in the magnetometry data in the FIG. 39 where the dominant high ferromagnetic moment due to the disordered structure are seen over the 5K~350K temperature range in case of 400° C, 500° C while those magnetic moments are significantly reduced in the ordered FCC structure at 600° C, 700° C. At 700° C growth temperature, all the diffraction intensities reach the highest values, which represent the highly-ordered BCC, L1<sub>0</sub> structures and well agree with the magnetometry result presented in FIG. 39. From the observed results and discussion, it is concluded that 110-oriented B2 structure of FeRhPd thin film is epitaxially grown with FCC(A1)-like L1<sub>0</sub> structure on the highly quality of 111-oriented Pt seed layer at 600~700°C. In thin film, the reduced dimensional effect, or the surface contribution on the magnetic phase transition can be studied in the thickness dependence.

FeRhPd Thickness (nm)	T <sub>growth</sub> (°C)	Around 38°~44° 2θ region						Around 83°~95° 2θ region					
		2θ <sub>1</sub> (°)	2θ <sub>2</sub> (°)	2θ <sub>3</sub> (°)	a <sub>1</sub> (=c) (CT) (Å)	a <sub>2</sub> (B2) (Å)	a <sub>3</sub> (B2') (Å)	2θ <sub>4</sub> (°)	2θ <sub>5</sub> (°)	2θ <sub>6</sub> (°)	a <sub>4</sub> (=c) (CT) (Å)	a <sub>5</sub> (B2) (Å)	a <sub>6</sub> (B2') (Å)
10	600	40.24	41.46	-	3.88	3.08	-	86.64	-	-	3.89	-	-
20	600	40.30	41.50	-	3.87	3.07	-	86.84	90.98	-	3.88	3.05	-
30	600	40.44	41.58	42.56	3.86	3.07	3.00	86.95	90.92	93.18	3.88	3.06	3.00
40	600	40.46	41.53	42.56	3.86	3.07	3.00	86.77	90.82	93.13	3.88	3.06	3.00
50	600	40.49	41.63	42.60	3.89	3.06	3.00	87.03	90.83	93.20	3.87	3.06	3.00
50	700	40.53	41.54	42.56	3.85	3.07	3.00	87.16	90.68	93.10	3.87	3.06	3.00
50	500	40.29	41.67	42.46	3.87	3.06	3.01	-	90.75	-	-	3.06	-
50	400	40.22	41.65	-	3.88	3.06	-	-	90.55	-	-	3.07	-

Table I Scattering angle for each FeRhPd peak identified by Gaussian fitting of X-ray diffraction results and the calculated lattice constants for the centered tetragonal (CT) and B2. Each scattering angle and the corresponding calculated lattice constant are labeled with the same subscript number.

Also, in the epitaxial film growth, the film morphology and structural formation of the film is strongly related to the film thickness due to the growth mode. The FIG. 37 shows the XRD results for the prepared FeRhPd film which has the varied thickness (10nm, 20nm, 30nm, 40nm, 50nm) grown on Pt(10nm) / Rh(10nm) on a-plane  $\alpha$ -Al<sub>2</sub>O<sub>3</sub> at 600°C, capped with Pt (6nm). As discussed in the FIG. 37 case, all diffraction peaks are observed around 38~44°, 83~95° 2 $\theta$  scattering angle regions and identified by Gaussian multi-peak fitting method.

Also, all fitting results and the calculated lattice constants are summarized in Table I. The superstructure peak region (83~95°) is plotted in the linear scale in the inset of FIG. 37 for clarity. In the inset, the decreased Pt, Rh peak intensity at the thicker film is ascribed to the diffusive characteristics of the interface between thin film layers at the high growth temperature, which is proportional to the film growth time. In all samples here, FeRhPd FCC (A1)-like L1<sub>0</sub> (222) peak are observed, which is related to the epitaxial film growth supported by the seed layers. At 10nm, only FeRhPd L1<sub>0</sub> (222) peak is observed though B2 (110) peak still exists around 38~44° 2 $\theta$  region, which indicates that only partially ordered B2 structure exists. As the film thickness increases, FeRhPd B2 (220) peak begins to appear at 20nm, new B2' (220) peak becomes noticeable at 30nm FeRhPd films and finally, all strong L1<sub>0</sub> (222), B2 (220), B2'(220) peaks are observed at 50nm. Thickness dependence of the structure in epitaxial film growth suggests that on 111-oriented seed layer, the coexisting L1<sub>0</sub>, B2 structure of FeRhPd is energetically favored and grows together and even this is valid at higher growth temperature 700°C as discussed previously. The thickness dependent growth of B2 structure is well observed in the in the FIG. 38 where the integrated B2, B2'(220) peak area is plotted with respect to the FeRhPd film thickness. The increasing B2 peak area at a thicker film indicates the growing B2 structural phase of the FeRhPd film.

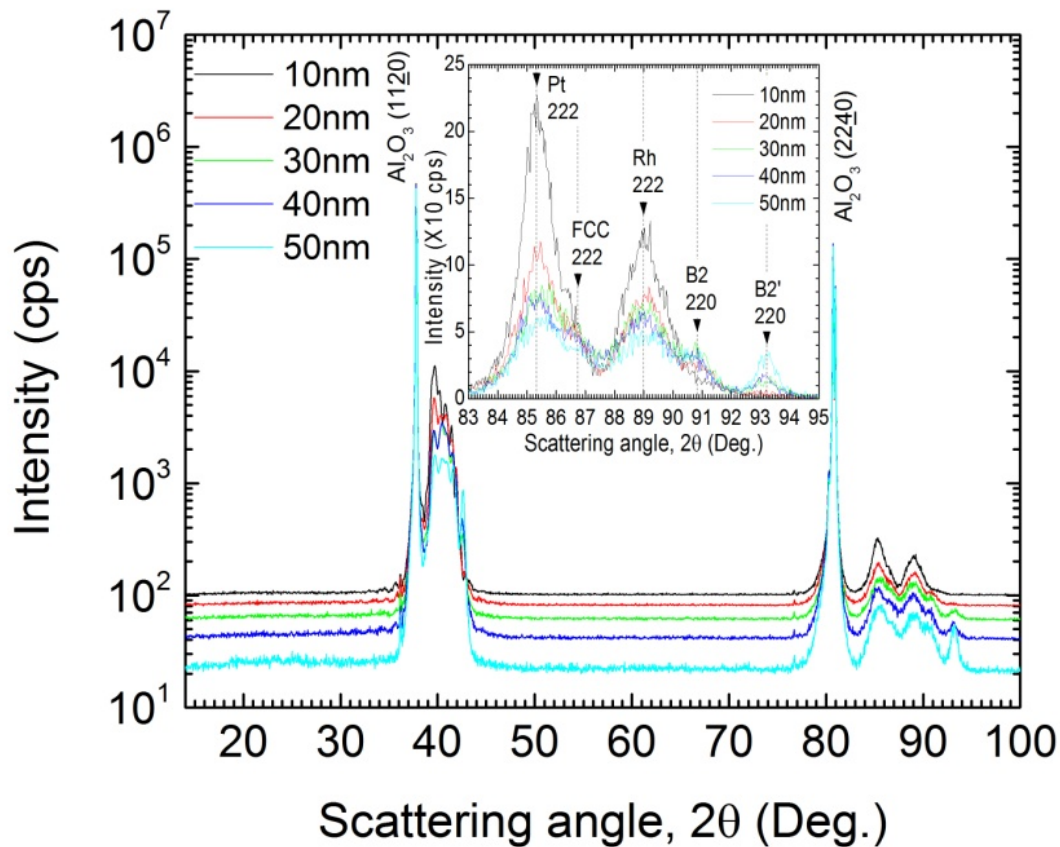


FIG. 37 X-ray diffraction  $\theta$ - $2\theta$  scan for FeRhPd (10nm, 20nm, 30nm, 40nm, 50nm) films on Pt(10nm) / Rh (10nm) on a-plane  $\alpha\text{-Al}_2\text{O}_3$  (1120) substrate grown at  $600^\circ\text{C}$ . All samples are capped with Pt (6nm). Each plot is shifted in intensity to clarify each diffraction pattern. The inset inside the figure shows the linear-scale plot of each diffraction peak at  $83^\circ\sim 95^\circ$  angle.

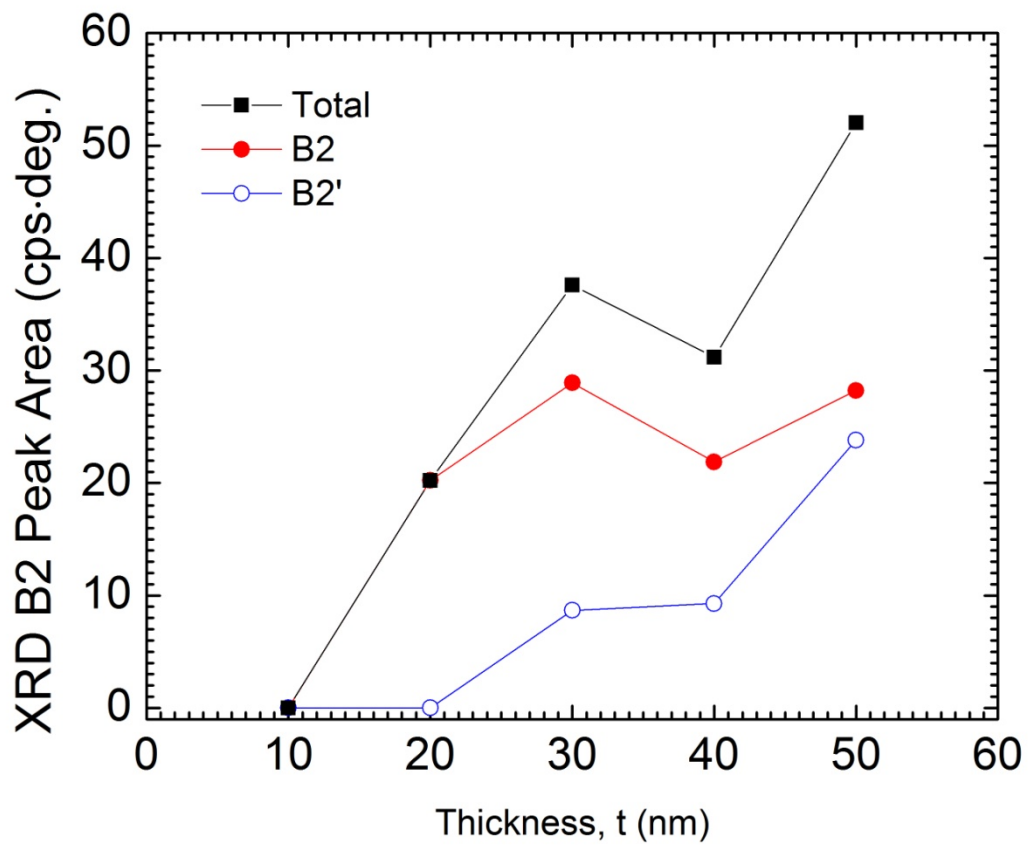


FIG. 38 The integrated B2, B2'(220) peak area of XRD result (FIG. 37) plotted with respect to the thickness of FeRhPd. The total is the sum of the integrated B2 and B2' peak area.

For the prepared samples, the temperature dependent magnetic property is examined by SQUID. The FIG. 39 shows SQUID measurement results for FeRhPd (50nm) samples grown at various temperatures. In SQUID measurement, first, the film is cooled down to 5K with zero applied magnetic field (ZFC). Then, SQUID signal is measured with 1T applied magnetic field during the heating and cooling procedure. For 400°C growth temperature case, the dominant portion of ferromagnetic phase and small portion magnetic phase transition is observed during the heating and cooling procedure. The dominant ferromagnetic phase and magnetic phase transition portion is attributed to the disordered structural state of the film and B2 structure, respectively, which is consistent with the observation of XRD result. In the FIG. 39, the magnetic phase transition portion is significantly increased at 600°C and maximized at 700°C while the dominant ferromagnetic phase is reduced at the same time. In XRD, FeRhPd B2 peak with new B2' peak appears with the increased L1<sub>0</sub> intensity at 600°C and all intensity is increased more at 700°C. The B2 structure of FeRhPd is mainly responsible for the magnetic phase transition of the film. The ordered L1<sub>0</sub> structure of FeRhPd is known to have the antiferromagnetic phase at low temperature. Highly ordered B2 structure at 700°C case shows the largest magnetization increase while it has the same constant magnetization as 600°C case at the temperature below the transition temperature. For the magnetic phase transition temperature, the well-ordered structure at a higher growth temperature shows the narrower and sharp magnetic phase transition. Thickness dependence of FeRhPd in M-T curve provides the information of the reduced dimensional effect and the surface contribution of the magnetic state of the film.

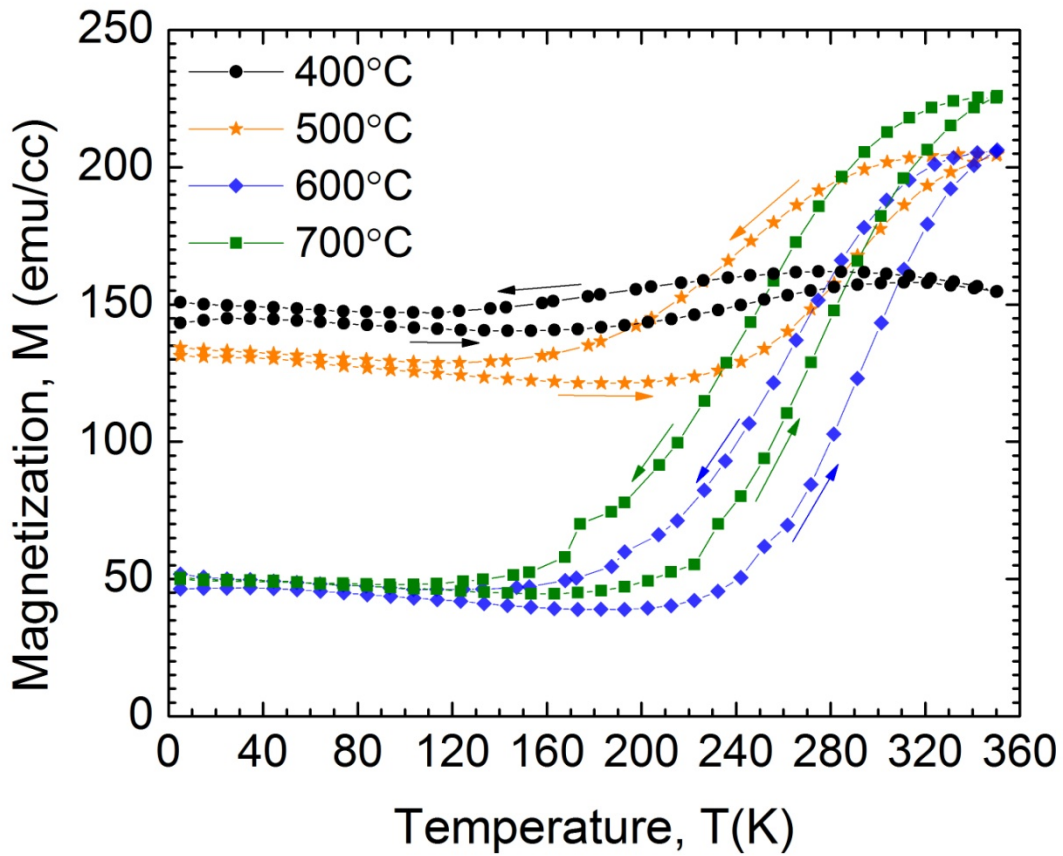


FIG. 39 SQUID measurement result of magnetization  $M$  versus temperature  $T$  for FeRhPd (50nm) films grown at 400°C, 500°C, 600°C, 700°C. 1T external magnetic field is applied during the measurement.

The FIG. 40 shows the SQUID results of magnetization versus temperature for the thickness varied FeRhPd (50nm, 30nm, 10nm) samples during heating and cooling process with 1T field. As the thickness of FeRhPd layer is reduced, the magnetic phase transition portion is significantly reduced with the increasing ferromagnetic state in the overall temperature region. 10nm FeRhPd sample shows mostly dominant ferromagnetic phase with the increasing magnetization at lower temperature, which is the typical ferromagnetic behavior. For 30nm FeRhPd case, the magnetic phase transition behavior is noticeable with the reduced the ferromagnetic moment and finally, it becomes the primary property of the film for 50nm FeRhPd. The reduced magnetization in the thicker film is related to the epitaxial film growth of the structure as examined in XRD.

The previous XRD result for 10nm FeRhPd film showed mostly  $L1_0$  structural phase which is known to have the antiferromagnetic phase for bulk FeRhPd at low temperature. As seen in the FIG. 40, the increased ferromagnetic phase of 10nm FeRhPd layer at lower temperature represents the energetically favored ferromagnetic state with the reduced dimension of  $L1_0$  structure of the film. For the well-ordered B2 structured FeRh thin film case, all stable anti-ferromagnetic phase even at 10, 20nm cases or, thin ferromagnetic phase at the surface has been reported recently [2, 27]. In the XRD result of 30nm FeRhPd film case, the B2, B2' structure which is responsible for the magnetic phase transition begins to appear with  $L1_0$  structural phase, which is consistent with the observed appearance of the magnetic phase transition portion in the FIG. 40.

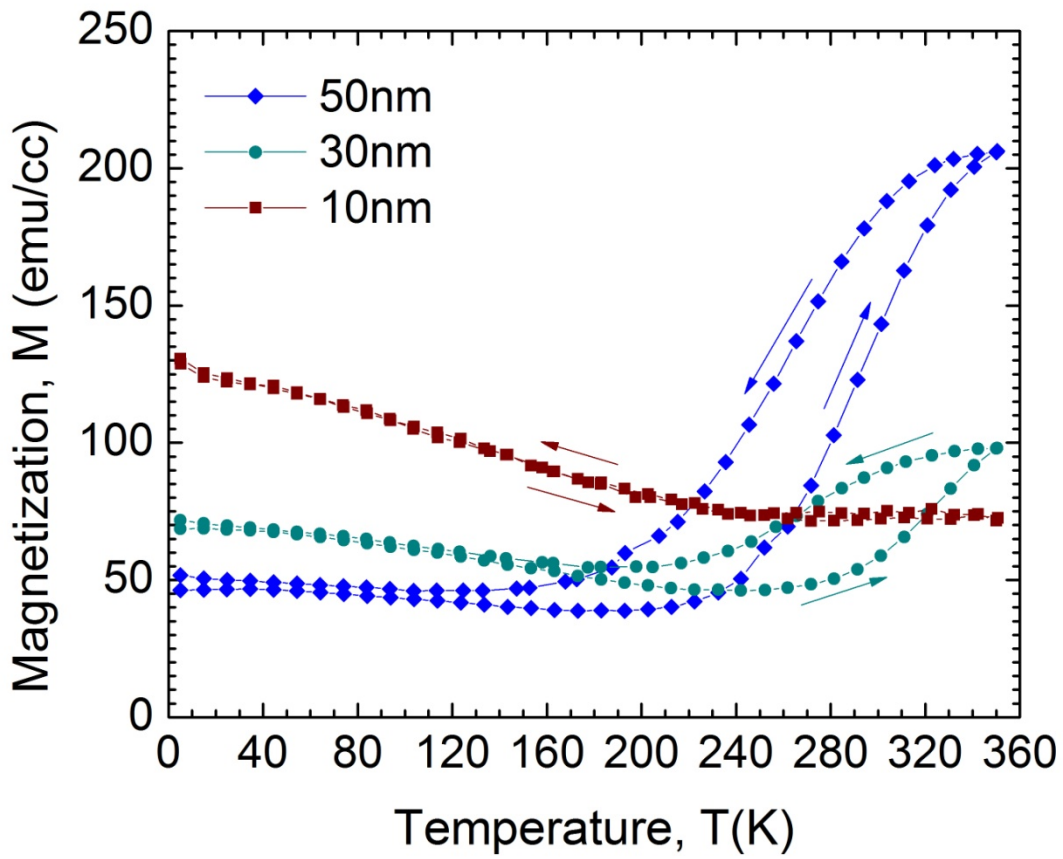


FIG. 40 SQUID measurement result of magnetization  $M$  versus temperature  $T$  for FeRhPd (50nm, 30nm, 10nm) grown at  $600^{\circ}\text{C}$ . The small arrow designates the heating and cooling direction. 1T external magnetic field is applied during the measurement.

At the same time, the increasing volume of the film with B2, L1<sub>0</sub> structures reduces the role of the interface magnetic moment in the magnetization, which explains the lowered magnetization at low temperature region. For 50nm FeRhPd film, the large magnetic phase transition is dominated with all profound B2, B2' structure growth with L1<sub>0</sub> structure in the XRD result. Thus, all the observed SQUID measurement result is well understood with the epitaxial film structure studied in XRD measurement.

In SQUID measurement for all FeRhPd films, the external magnetic field was applied along the zero field cooling (ZFC) and field cooling (FC) protocols, which provides the information of the interaction between the frozen magnetic moments [73]. In a close look of the previous SQUID results near the lowest temperature region, the reduced magnetic moment with the decreasing temperature was observed for some FeRhPd films. In the FIG. 41 and FIG. 42, the lowest temperature region of M-T curve is magnified at the smaller scales to examine the thermal hysteretic effect by field cooling. As seen in the the FIG. 41 and FIG. 42, the magnetization saddle point on the curve for the zero-field cooled (ZFC) state is observed around 20K for 400°C, 600°C cases while 1T field cooled (FC) curve shows the field induced magnetic moment. The decreasing magnetization below the freezing temperature  $T_f$ , in ZFC state represents the frozen randomly oriented magnetic moments. When the ZFC sample is warmed up for the measurement, the randomly frozen magnetic moments begin to be aligned along the external magnetic field during heating. On the other hand, in FC state, all aligned magnetic moments are frozen as in that state due to the weak interaction between magnetic moments. This glassy-like magnetic state is known as “spin glass”.

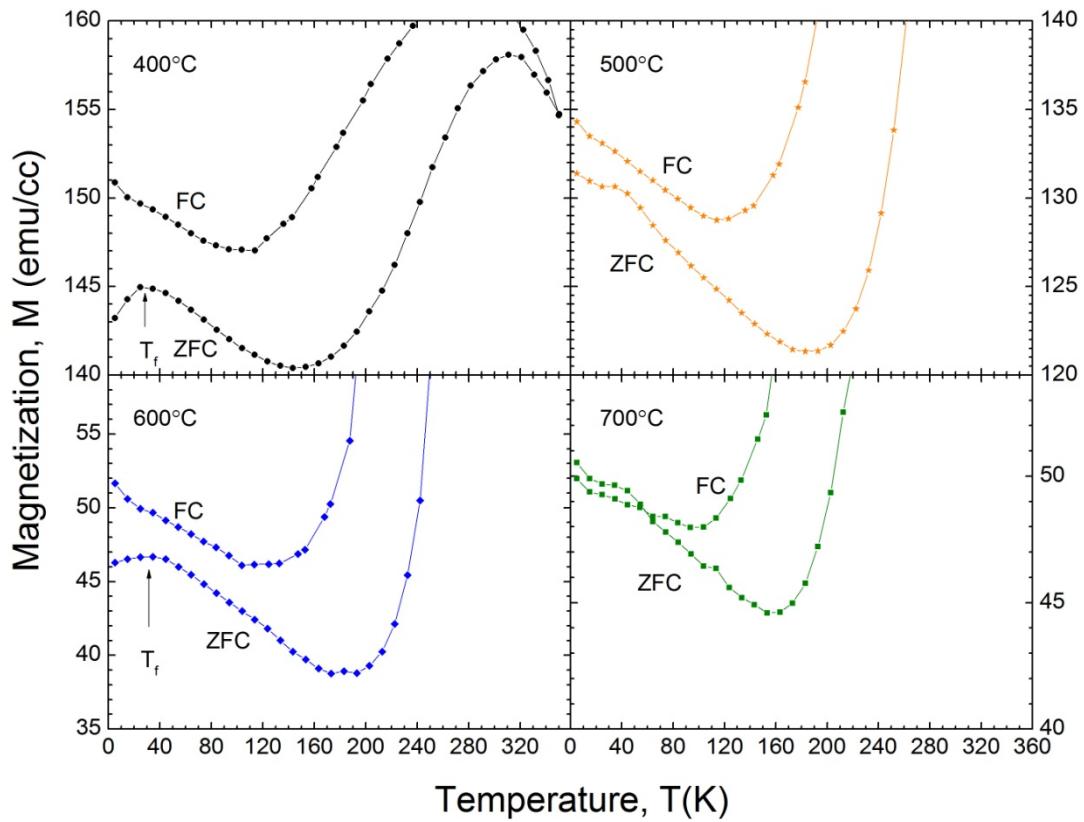


FIG. 41 SQUID measurement results re-plotted in the smaller scales of magnetization for FeRhPd (50nm) films grown at 400°C, 500°C, 600°C, 700°C. In the figure, ZFC represents the zero field cooling and FC, 1T field cooling. The freezing temperature ( $T_f$ ) is indicated with arrows.

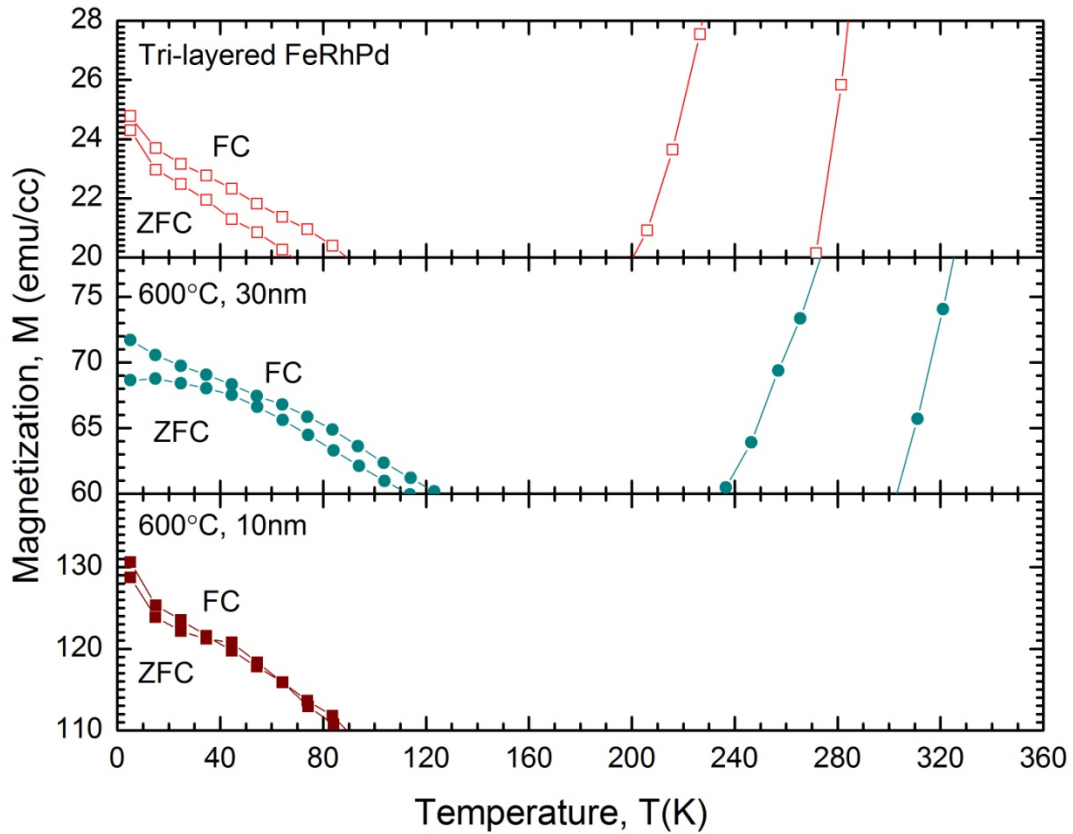


FIG. 42 SQUID measurement results re-plotted in the smaller scales of magnetization for FeRhPd (30nm, 10nm) and [FeRhPd(25nm)/ Pt(0.5nm)/ FeRhPd(25nm)] tri-layered film. In the figure, ZFC represents the zero field cooling and FC, 1T field cooling.

In the metal alloy system, the spin-glass-like feature has been reported for the FCC  $\gamma$  phase FeRh [83-85] and some other alloy system [86]. In FeRh, the presence of the spin-glass-like behavior indicates the existence of the portion of the meta-stable  $\gamma$  phase. Therefore, as discussed in XRD result previously, the observed FCC (A1)-like  $L1_0$  structure must be carefully judged for the possible involvement of the disordered FCC state shown in some samples.

### 3. Trilayer FeRhPd

Further property of FeRhPd thin film is studied for the multilayered structure which is commonly concerned in the future technology. The magnetic coupling effect of magnetic phase transition is studied for the epitaxial [ FeRhPd (25nm) / Pt (0.5nm) / FeRhPd (25nm) ] structure where thin Pt spacer is chosen to preserve the epitaxial film growth for the entire structure.

The FIG. 43 shows XRD results of trilayered FeRhPd structures. All the same kinds of peaks as in the FeRhPd single layered case are identified from the Gaussian multi-peak fitting in the inset of FIG. 43. For the film thickness and roughness, the smooth film morphology and the expected thickness of each layer are configured in the fitting of X-ray reflectivity (XRR) in the FIG. 44. The blunt Kiessig oscillation in XRR indicates some interdiffusion feature at the interface of each layer. The epitaxy of each layer is confirmed in the pole figure measurement result in the FIG. 45 (a). As seen in the graph, 6-fold symmetric Pt (111), FeRhPd (111) peaks were measured at the tilted angle  $70.52^\circ$ , while two-fold symmetric a-plane  $\alpha\text{-Al}_2\text{O}_3$  ( $11\bar{2}0$ ) was measured at  $60^\circ$ . The highly ordered structure (111) was observed in the rocking curve scan result for each FeRhPd (111) in FIG. 45 (b). The well-defined Pt seed layer in 111-direction provides the good epitaxial relation to FeRhPd layer.

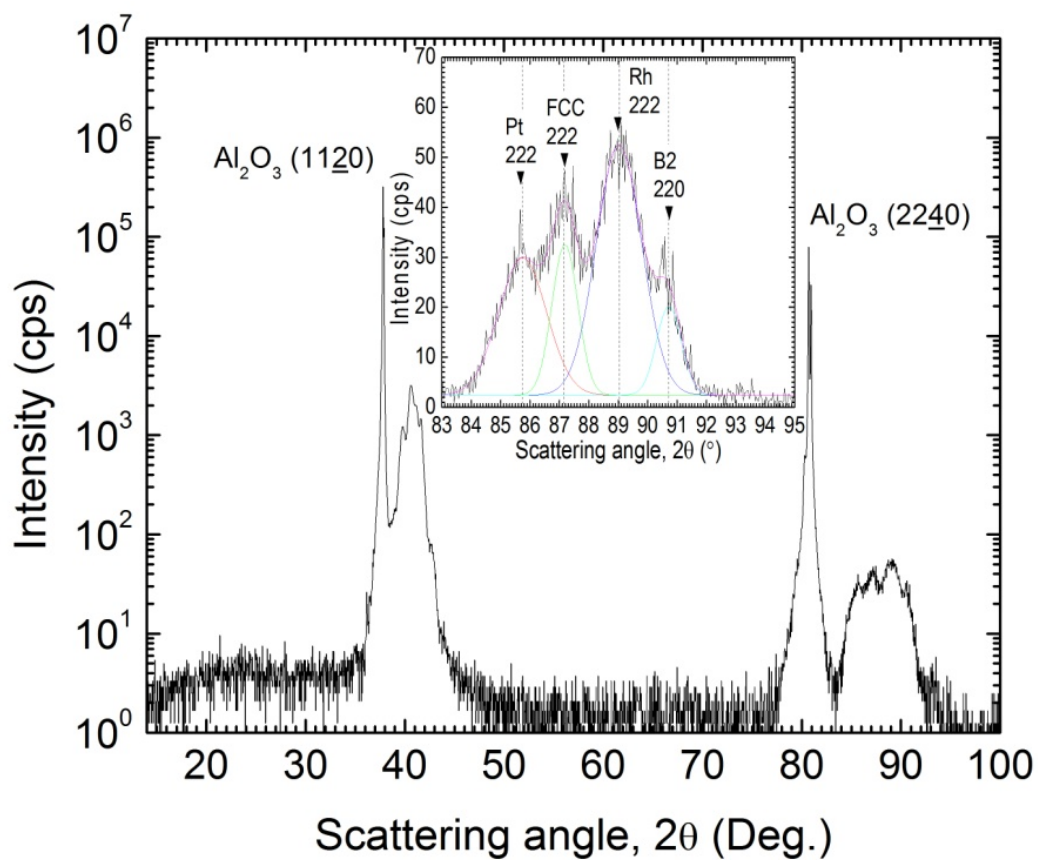


FIG. 43 X-ray diffraction  $\theta$ - $2\theta$  scan for FeRhPd (25nm) / Pt (0.5m) / FeRhPd (25nm) films on Pt (10nm) / Rh (10nm) / a-plane  $\alpha$ -Al<sub>2</sub>O<sub>3</sub> (1120) substrate grown at 600°C with Pt (6nm) capping layer. The inset in (a) shows the linear plot of the diffraction peak at the angle 83~95°

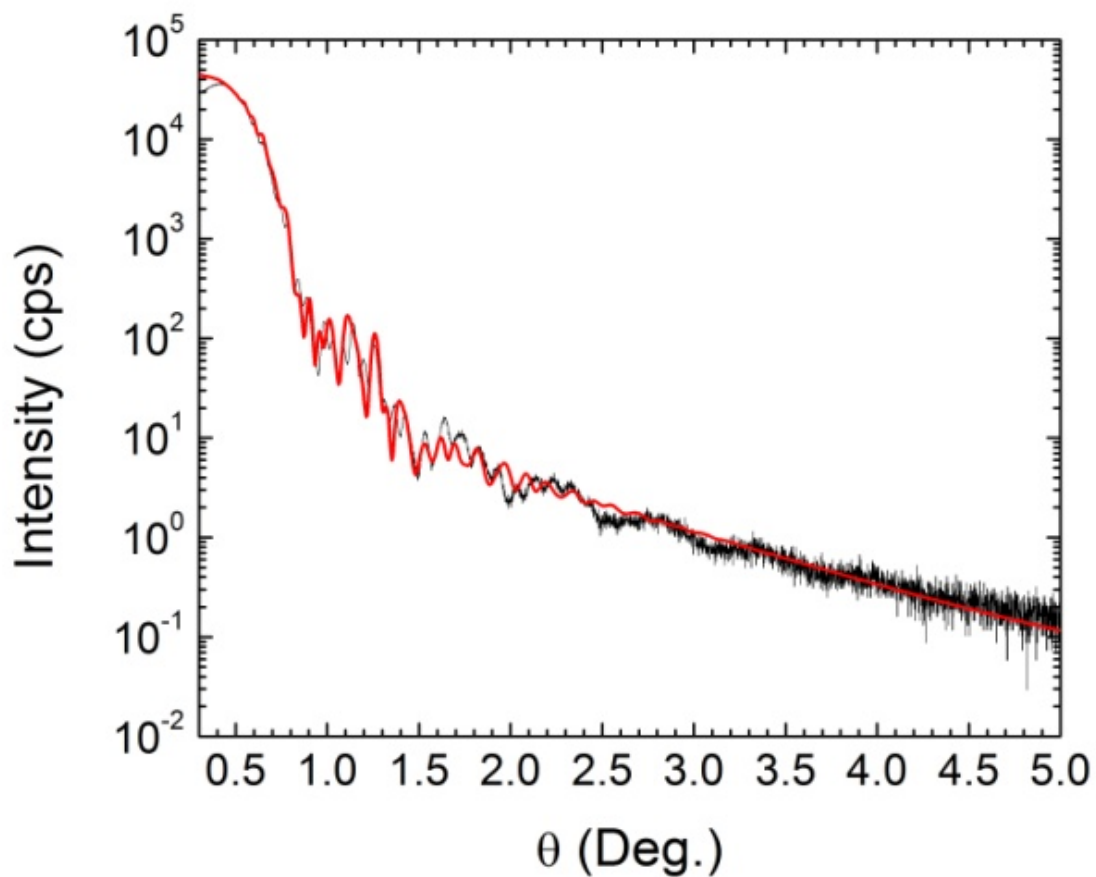


FIG. 44 X-ray reflectivity and fitting (red line) results for FeRhPd (25nm) / Pt (0.5m) / FeRhPd (25nm) films on Pt (10nm) / Rh (10nm) / a-plane  $\alpha$ -Al<sub>2</sub>O<sub>3</sub> (11 $\bar{2}$ 0) substrate grown at 600°C with Pt (6nm) capping layer.

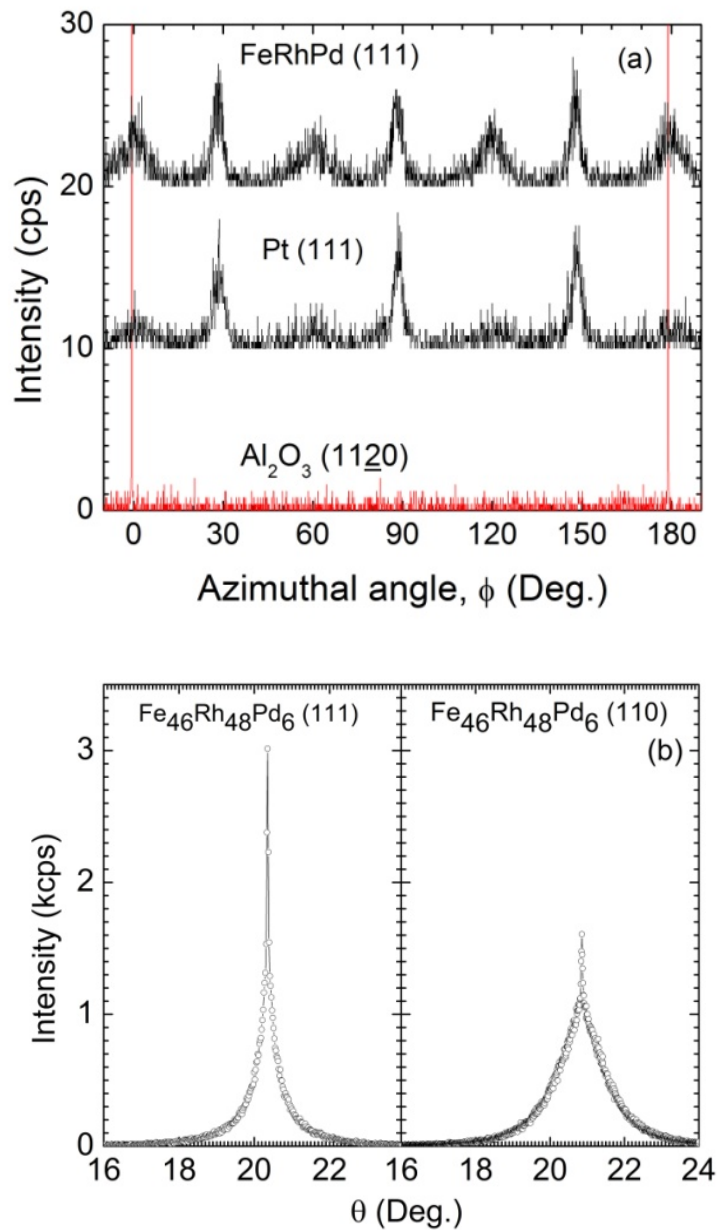


FIG. 45 (a) Pole figure measured for  $\alpha$ - $\text{Al}_2\text{O}_3$ (1120) at the tilted angle  $60^\circ$  and Pt (111), FeRhPd (111) at the tilted angle  $70.5^\circ$ , (b) rocking curve measured for FeRhPd (111), FeRhPd (110). In (a), each pole figure of Pt and FeRhPd is shifted by 10 counts per second for clarity.

The dominating narrow sharp peak in the FIG. 45 (b) indicates the highly ordered  $L1_0$  structure portion of FeRhPd layer in the 111 orientation. On the other hand, B2 structured FeRhPd portion has two different configuration of sharp and broad parts in the rocking curve, which represents the highly ordered layers and misfit dislocation defects as in Rh on  $\alpha$ - $\text{Al}_2\text{O}_3(11\bar{2}0)$  case. Therefore, it is concluded that the highly ordered epitaxial coexisting thin films were grown.

The magnetic property of the FeRhPd film at room temperature is examined by Vibrating sample magnetometer (VSM). The hysteresis loop of FeRhPd tri-layered sample in the FIG. 46 shows the magnetization 90emu/cc and the coercivity, 700 Oe. The thermal dependent property for the magnetization is also examined by SQUID measurement and compared with the single layered FeRhPd structure. In the FIG. 47, the measured M-T behavior for tri-layered FeRhPd is compared to the single-layered FeRhPd (30nm, 50nm) results which are taken from the FIG. 40 and re-plotted together here. In comparison, first, tri-layered FeRhPd (25nm) can be regarded as the sum of two separate FeRhPd (25nm) layers. In the FIG. 47, M-T curve for tri-layered structure is clearly distinguished from that of FeRhPd 30nm result for the magnetization, magnetic phase transition and the low temperature behavior. As in the FIG. 47, tri-layered FeRhPd has the slightly higher saturated magnetization at 350K, and the significantly reduced magnetization for the ferromagnetic phase of the sample. In another perspective, tri-layered FeRhPd can be considered as FeRhPd (50nm) broken by thin Pt (0.5nm) spacer in the middle. Compared to 50nm FeRhPd case, tri-layered FeRhPd shows approximately half of the magnetization of FeRhPd (50nm) layer for all temperature range.

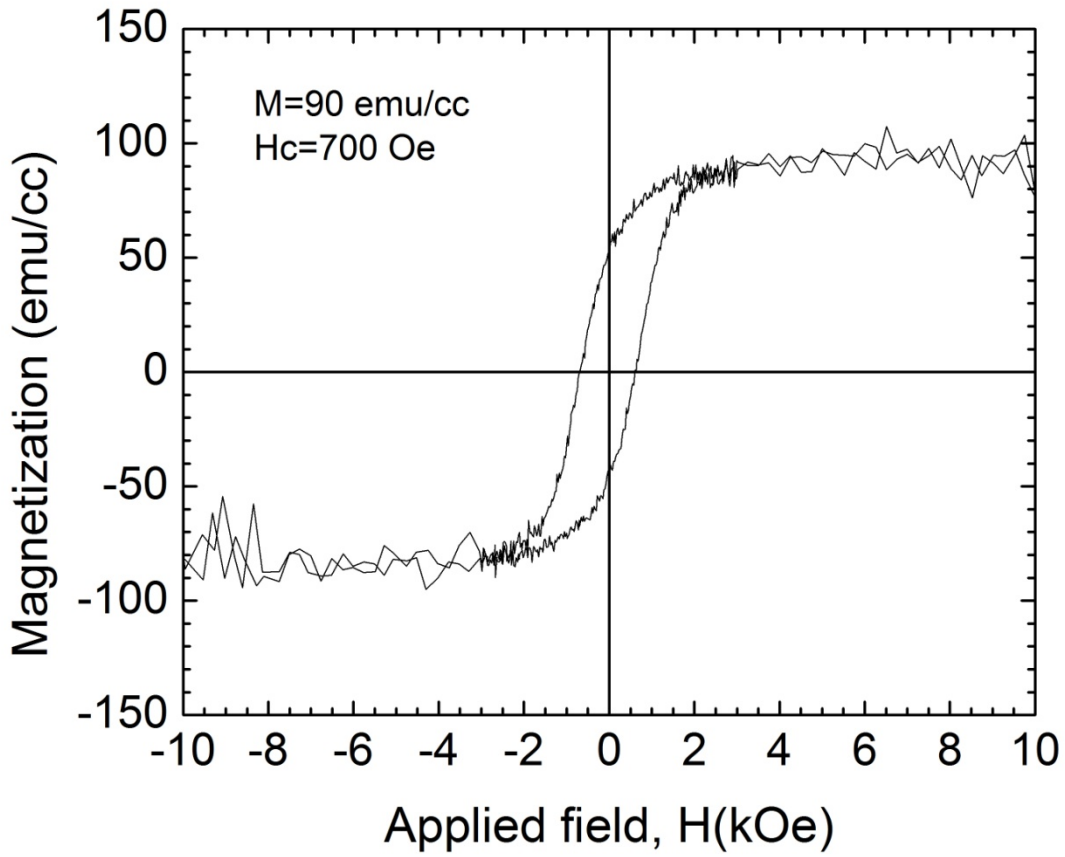


FIG. 46 The magnetization hysteresis loop of FeRhPd tri-layered sample measured by VSM.

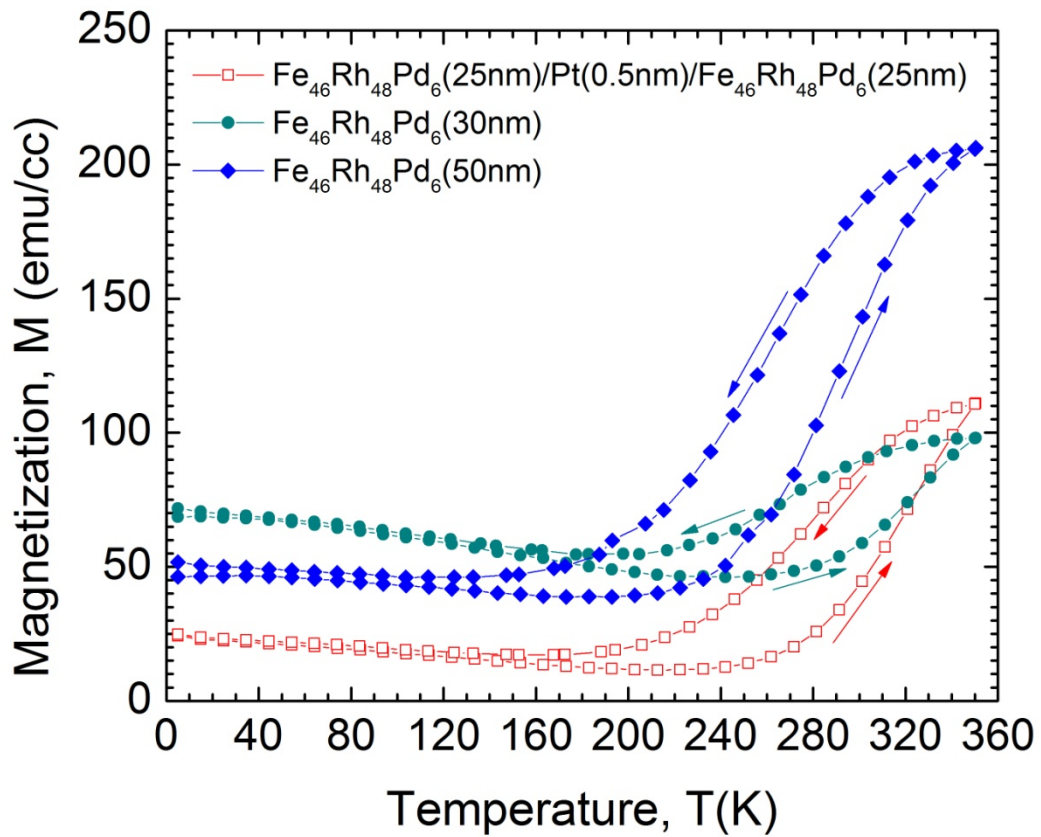


FIG. 47 SQUID measurement results of  $[\text{FeRhPd}(25\text{nm})/\text{Pt}(0.5\text{nm})/\text{FeRhPd}(25\text{nm})]$  tri-layered film plotted with  $\text{FeRhPd}(50\text{nm}, 30\text{nm})$  previous results for comparison. During the measurement, 1T external magnetic field is applied.

This thickness proportionality of the magnetization of FeRhPd differs from the single-layered FeRhPd case demonstrated in the FIG. 40 where the FeRhPd single layer with a reduced thickness shows the increasing ferromagnetic portion of the thin film. For the thin Pt spacer layer, the interlayer exchange coupling between ferromagnetic layers has been reported in multilayered structure before [87-89]. At 600°C high growth temperature, the interdiffusion at the interface is also expected in multilayered structure [90]. The difference between three cases shown in the FIG. 47 suggests that the coupling through Pt spacer layer reduces the ferromagnetic phase of the film while the magnetic phase transition part is almost conserved.

#### 4. Polarized neutron reflectivity

For the magnetic multilayered structure, polarized neutron reflectivity (PNR) has the advantage to detect the magnetic state of individual magnetic layer. For tri-layered FeRhPd sample, PNR experiment was performed in the beam line 4A of Spallation Neutron Source in Oak Ridge National Laboratory.

In PNR experiment, the pulsed neutrons sources operated at 60Hz frequency are employed. The continuous wavelength spectrum of the pulsed neutrons is resolved by time-of-flight (TOF) method. For the detection of the magnetic property of the sample, PNR is measured for two non-spin-flip channel (spin++, spin--) at each angle, where spin polarizations of neutrons are interchanged by spin-flipper. To measure the field dependent property, the in-plane magnetic field 1T, 0.005T are applied to the sample by electromagnet. In PNR experiment, the polarized neutron is scattered by the nucleus and magnetic induction. In the multilayered thin film scheme, the scattering potential is expressed of the film thickness as the combination of the nuclear potential  $V_N$  and magnetic induction  $B$  as discussed in the previous chapter [56]. In the optical

approximation, the magnetization contribution term in the potential is treated as the additional sum of the scattering length density. The scattering length densities ( $\rho_+$ ,  $\rho_-$ ) in two spin channels are represented by  $\rho_n + \rho_m$ ,  $\rho_n - \rho_m$ , respectively, where  $\rho_n$  is the nuclear scattering length density,  $\rho_m$ , the magnetic contribution to the scattering length density. The magnetization of the magnetic film is distinguished by comparing the scattering length densities between two spin channel cases. Then, the magnetization is calculated as in the equation (23) [51].

$$\rho_m = (2.9109 \times 10^{-9}) \times M \text{ \AA}^{-2}\text{m/kA} \quad (23)$$

The PNR data is fitted by the Parratt recursion relation to obtain the scattering length profile which is plotted by the following equation (24) with respect to the depth of the sample under the assumption of Fick's second law of thin film interface diffusion with the same Gaussian variance as the Gaussian roughness in the specular reflectivity [51, 52, 54, 91].

$$\rho(z) = \sum_{i=1}^N \frac{\rho_i - \rho_{i+1}}{2} \left(1 + \operatorname{erf}\left(\frac{z - z_i}{\sqrt{2}\sigma_i}\right)\right) \quad (24)$$

In the equation (24),  $N$  is the total number of layers,  $\rho_i$ , the scattering length density of  $i$ -th layer,  $z_i$ , the interface position in the film,  $\sigma_i$ , Gaussian roughness. To reduce the number of fitting parameters, the thicknesses and roughnesses are taken from XRR fitting results. The FIG. 48 shows the reflectivity results measured at 450K, 350K, 300K, 5K temperature during field cooling procedure and its respective scattering length density profile plotted by the equation (24). Before the measurement, the temperature is elevated up to 450K with 1T field. As shown in the

result of SQUID magnetometry measurement, tri-layered FeRhPd shows ferromagnetic phase at 350K, 450K and as the temperature decreases, the magnetic phase transition occurs around 300K. In the FIG. 48, the splittings of the reflectivity between two spin channels are obvious at 450K, 350K, 300K, which explains the existence of the magnetic moment in the film. The final result of each reflectivity fitting is represented by the scattering length density profiles in the FIG. 48. The splitting of the scattering length densities (SLD) ( $\rho_+$ ,  $\rho_-$ ) between two spin channels (spin++, spin--) reveals the magnetization of the film. In the FIG. 48, it is shown that the SLD splitting for FeRhPd layers are decreased, as the temperature of the sample decreases. In addition, the unexpected asymmetric SLD splitting between two FeRhPd layers is obtained in 450K, 350K, 300K cases, which implies the different magnetization. For 350K, the obtained magnetizations by the equation (23) for two FeRhPd layers from the equation are  $\sim 181$  kA/m,  $\sim 5$  kA/m, respectively, which is consistent with the overall magnetization 110kA/m measured by SQUID result at 350K on the field cooling curve. The consistent overall magnetization of the film are also observed at 300K, 5K temperature cases where the magnetizations are 90 kA/m (300K), 24 kA/m (5K) for SQUID,  $\sim 150$  kA/m,  $\sim 10$ kA/m (300K), the same  $\sim 31$  kA/m (5K) for PNR. The observed asymmetric distribution of magnetization between two FeRhPd layers is closely related to its structural formation of the film with respect to the film thickness. As observed in the previous thickness dependence of FeRhPd single-layered film in the FIG. 37 and FIG. 38, the thickness dependent growth of B2 structure indicates the existing inhomogeneous distribution of magnetic moment in the film. To verify the exact configuration of the magnetization, further research will be continued.

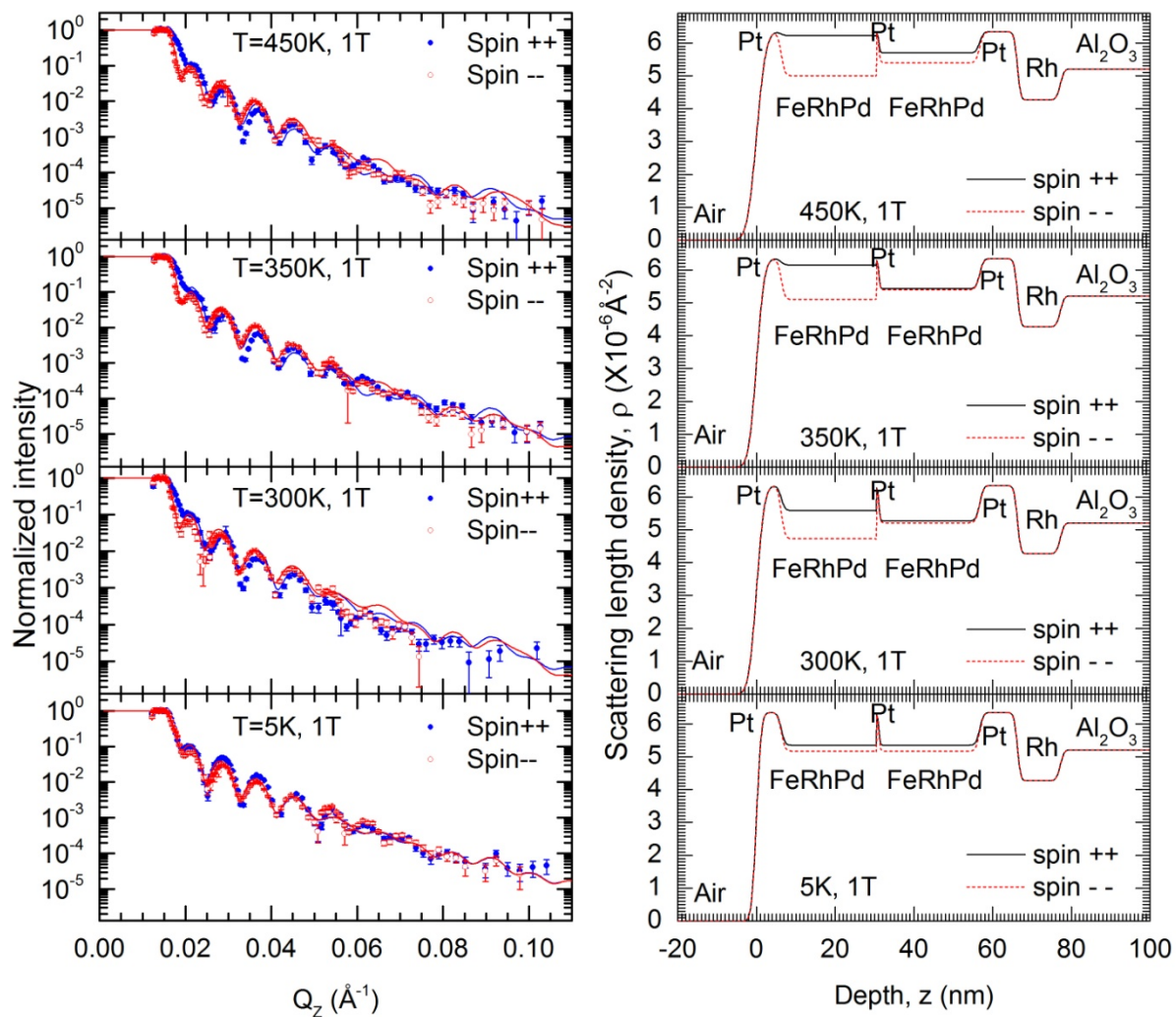


FIG. 48 PNR (left) measured for non-spinflip channels at 450K, 350K, 300K, 5K with 1T applied field along the cooling and its scattering length density depth profile (right) obtained from fitting by Parratt recursion relation.

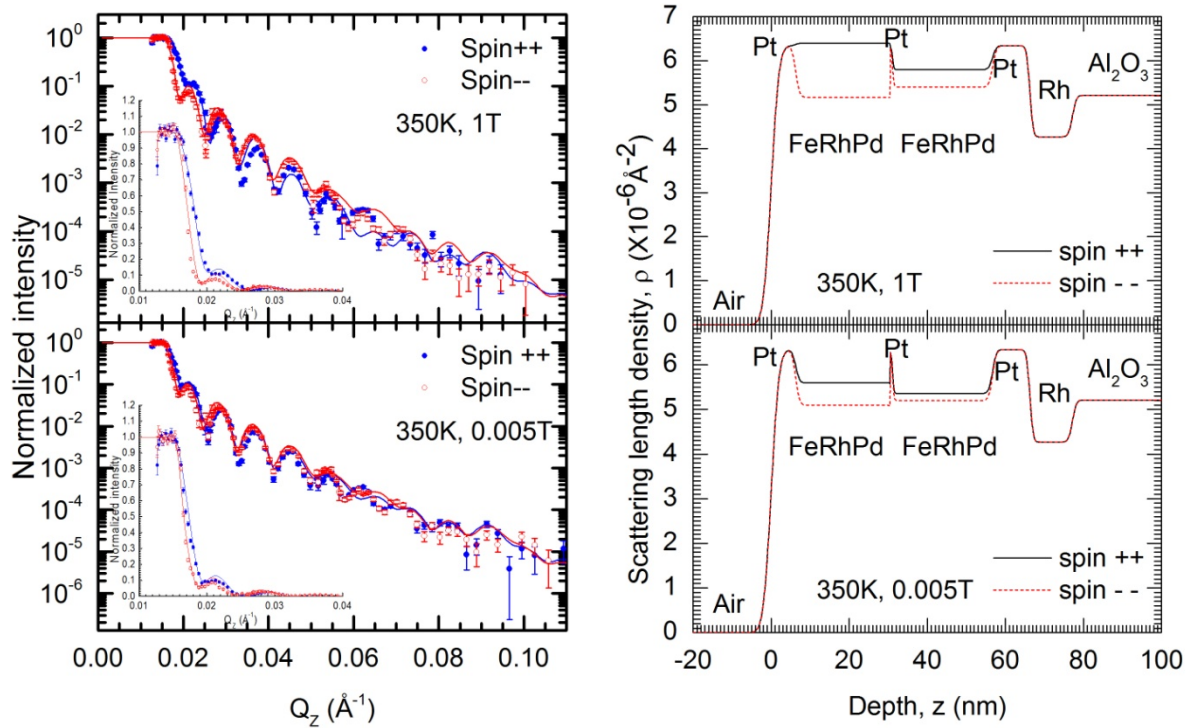


FIG. 49 PNR (left) measured for non-spinflip channels at 350K with 1T, 0.005T applied field along the heating and its scattering length density depth profile (right) obtained from fitting by Parratt recursion relation. The inset (right) is the linear plot of PNR around the critical scattering vector.

The FIG. 49 shows PNR data and the scattering length profile at 350K temperature with 1T, 0.005T applied magnetic fields during heating in the thermal hysteresis. In PNR, the different splitting of two spin channels with respect to applied field around the critical scattering vector region is clearly observed in the linear plot in the inset of the FIG. 49. In the scattering length profile in FIG. 49, the SLD difference between two spin channels with 1T field is higher than 0.005T case in two FeRhPd layers, which shows that the magnetic moment during magnetic phase transition is induced by the external magnetic field in both FeRhPd layers, regardless of the asymmetric magnetic state of each layer.

## VI. CONCLUSION

In this work, we studied the epitaxial FePtRh film on Pt (111) and compositionally-modulated FePtRh FM/AFM bilayers. With Pt, Cr seed and buffer layers, the epitaxial growth and crystallographic orientation is well understood by X-ray diffraction in the single and bilayered FePtRh. In  $[\text{Fe}_{50}\text{Pt}_{45}\text{Rh}_5 \text{ (FM)}/ \text{Fe}_{50}\text{Pt}_{25}\text{Rh}_{25} \text{ (AFM)}] \times 8$ , the compositional contrast between  $\text{Fe}_{50}\text{Pt}_{45}\text{Rh}_5$  and  $\text{Fe}_{50}\text{Pt}_{25}\text{Rh}_{25}$  is confirmed in X-ray diffraction, transmission electron microscopy. The magnetic contrast between FM and AFM is also well observed in the polarized neutron reflectivity, which is consistent with compositional modulation.

In [FM/AFM], the negligible exchange bias was observed at room temperature while the slight increase in exchange coupling appeared at lower temperature. Therefore, the well-defined structural interface and the magnetic property are confirmed.

For FeRhPd, we studied 111-oriented epitaxial  $\text{Fe}_{46}\text{Rh}_{48}\text{Pd}_6$  thin film grown on the high quality of Pt seed layer. The revealed strong epitaxial relation between Rh and a-plane  $\alpha\text{-Al}_2\text{O}_3$  (11 $\bar{2}$ 0) provided the good buffer layer for 111-oriented epitaxial film growth. XRD experiment revealed that co-existing stable AF FCC(A1)-like  $L1_0$  (111), B2 (110) structures of the epitaxially-grown FeRhPd films at Fe-deficient composition where the coexisting meta-stable FCC(A1)  $\gamma$  phase and B2  $\alpha'$  phase are expected in FeRh alloy case. The highly ordered structure and clear magnetic phase transition were observed for FeRhPd films grown at 600°C, 700°C temperature while the disordered state of FeRhPd showed the dominant ferromagnetic state over 5K~350K temperature. In the thickness dependence of FeRhPd single layered films grown at 600°C, the reduced portion of magnetic phase transition and increased ferromagnetic phase at thinner film in SQUID results suggested the energetically favored ferromagnetic state of the film

interface. In the field dependent M-T curve, the freezing magnetic moment around 30K for some samples showed the existence of small portion of the meta-stable spin-glass-like state up to 600°C growth temperature while disordered states completely disappears at 700°C. The SQUID result for the tri-layered FeRhPd with Pt spacer showed the stabilized magnetic phase transition and the reduced ferromagnetic phase. Magnetic depth profiles of tri-layered FeRhPd from PNR showed the asymmetric magnetization between two FeRhPd layers along the thermal hysteresis. The asymmetric magnetic profile of FeRhPd tri-layered structure in PNR indicates the inhomogeneous distribution of the magnetization inside the FeRhPd film and the further research is required to verify the exact configuration of the magnetization of FeRhPd film.

## REFERENCES

- [1] N. T. Nam, W. Lu, and T. Suzuki, *J. Appl. Phys.* **105**, 07D708 (2009).
- [2] I. Suzuki, T. Koike, M. Itoh, T. Taniyama, and T. Sato, *J. Appl. Phys.* **105**, 07E501 (2009).
- [3] S. Yuasa, H. Miyajima, and Y. Otani, *J. Phys. Soc. Jpn.* **63**, 3129 (1994).
- [4] D. Lott, J. Fenske, A. Schreyer, P. Mani, G. J. Mankey, F. Klose, W. Schmidt, K. Schmalzl, and E. V. Tartakovskaya, *Phys. Rev. B* **78**, 174413 (2008).
- [5] T. Hasegawa, J. Miyahara, T. Narisawa, S. Ishio, H. Yamane, Y. Kondo, J. Ariake, S. Mitani, Y. Sakuraba, and K. Takanashi, *J. Appl. Phys.* **106**, 103928 (2009).
- [6] W. Lu, N. T. Nam, and T. Suzuki, *J. Appl. Phys.* **105**, 07A904 (2009).
- [7] K. Uchida, S. Takahashi, K. Harii, J. Ieda, W. Koshibae, K. Ando, S. Maekawa, and E. Saitoh, *Nature* **455**, 778 (2008).
- [8] I. L. Prejbeanu, M. Kerekes, R. C. Sousa, H. Sibuet, O. Redon, B. Dieny, and J. P. Nozieres, *Journal of Physics: Condensed Matter* **19**, 165218 (2007).
- [9] H. Shiino, M. Kawana, E. Miyashita, S. Watanabe, and N. Hayashi, *J. Appl. Phys.* **105**, 07B906 (2009).
- [10] M. Hatami, G. E. W. Bauer, Q. Zhang, and P. J. Kelly, *Phys. Rev. B* **79**, 174426 (2009).
- [11] S. Yuasa, H. Miyajima, Y. Otani, and A. Sakuma, *J. Phys. Soc. Jpn.* **64**, 4906 (1995).
- [12] J.-U. Thiele, S. Maat, and E. E. Fullerton, *Appl. Phys. Lett.* **82**, 2859 (2003).
- [13] L. Theil Kuhn, N. Pryds, C. R. H. Bahl, and A. Smith, *J. Phys.* **303**, 012082 (2011).
- [14] V. K. Pecharsky, K. A. Gschneidner, Jr., A. O. Pecharsky, and A. M. Tishin, *Phys. Rev. B* **64**, 144406 (2001).
- [15] G. Ju, J. Hohlfeld, B. Bergman, R. J. M. van de Veerdonk, O. N. Mryasov, J.-Y. Kim, X. Wu, D. Weller, and B. Koopmans, *Phys. Rev. Lett.* **93**, 197403 (2004).
- [16] P. H. L. Walter, *J. Appl. Phys.* **35**, 938 (1964).

- [17] M. P. Annaorazov, K. A. Asatryan, G. Myalikhgulyev, S. A. Nikitin, A. M. Tishin, and A. L. Tyurin, *Cryo* **32**, 867 (1992).
- [18] S. Maat, J. U. Thiele, and E. E. Fullerton, *Phys. Rev. B* **72**, 214432 (2005).
- [19] I. Suzuki, T. Naito, M. Itoh, T. Sato, and T. Taniyama, *J. Appl. Phys.* **109**, 07C717 (2011).
- [20] T. Naito, I. Suzuki, M. Itoh, and T. Taniyama, *J. Appl. Phys.* **109**, 07C911 (2011).
- [21] J. van Driel, R. Coehoorn, G. J. Strijkers, E. Bruck, and F. R. de Boer, *J. Appl. Phys.* **85**, 1026 (1999).
- [22] S. Yuasa, H. Miyajima, Y. Otani, G. Masada, N. Wakabayashi, and K. Tajima, *J. Phys. Soc. Jpn.* **64**, 3153 (1995).
- [23] M. E. Gruner, E. Hoffmann, and P. Entel, *Phys. Rev. B* **67**, 064415 (2003).
- [24] C. Stamm, J. U. Thiele, T. Kachel, I. Radu, P. Ramm, M. Kosuth, J. Minar, H. Ebert, H. A. Durr, W. Eberhardt, and C. H. Back, *Phys. Rev. B* **77**, 184401 (2008).
- [25] P. Kushwaha, A. Lakhani, R. Rawat, and P. Chaddah, *Phys. Rev. B* **80**, 174413 (2009).
- [26] J. W. Kim, P. J. Ryan, Y. Ding, L. H. Lewis, M. Ali, C. J. Kinane, B. J. Hickey, C. H. Marrows, and D. A. Arena, *Appl. Phys. Lett.* **95**, 222515 (2009).
- [27] R. Fan, C. J. Kinane, T. R. Charlton, R. Dorner, M. Ali, M. A. de Vries, R. M. D. Brydson, C. H. Marrows, B. J. Hickey, D. A. Arena, B. K. Tanner, G. Nisbet, and S. Langridge, *Phys. Rev. B* **82**, 184418 (2010).
- [28] M. Manekar, C. Mukherjee, and S. B. Roy, *Europhys. Lett.* **80**, 17004 (2007).
- [29] S. M. Durbin, J. E. Cunningham, M. E. Mochel, and C. P. Flynn, *J. Phys. F: Met. Phys.* **11**, L223 (1981).
- [30] M. B. Salamon, S. Sinha, J. J. Rhyne, J. E. Cunningham, R. W. Erwin, J. Borchers, and C. P. Flynn, *Phys. Rev. Lett.* **56**, 259 (1986).
- [31] J. Mayer, C. P. Flynn, and M. Rühle, *Ultramicroscopy* **33**, 51 (1990).
- [32] P. M. Reimer, H. Zabel, C. P. Flynn, and J. A. Dura, *Phys. Rev. B* **45**, 11426 (1992).
- [33] R. F. C. Farrow, G. R. Harp, R. F. Marks, T. A. Rabedeau, M. F. Toney, D. Weller, and S. S. P. Parkin, *J. Cryst. Growth* **133**, 47 (1993).
- [34] G. R. Harp, and S. S. P. Parkin, *Thin Solid Films* **288**, 315 (1996).

- [35] T. J. Minvielle, R. L. White, M. L. Hildner, and R. J. Wilson, *Surf. Sci.* **366**, L755 (1996).
- [36] M. L. Hildner, T. J. Minvielle, and R. J. Wilson, *Surf. Sci.* **396**, 16 (1998).
- [37] F. Garcia-Sanchez, O. Chubykalo-Fesenko, O. N. Mryasov, R. W. Chantrell, and K. Y. Guslienko, *J. Appl. Phys.* **97**, 10J101 (2005).
- [38] Y. Yokoyama, M. Usukura, S. Yuasa, Y. Suzuki, H. Miyajima, and T. Katayama, *J. Magn. Magn. Mater.* **177-181**, 181 (1998).
- [39] J. A. Thornton, *J. Vac. Sci. Technol., A* **4**, 3059 (1986).
- [40] J. W. Matthews, *Epitaxial Growth* (Academic Press, 1975).
- [41] M. A. Herman, W. Richter, and H. Sitter, *Epitaxy : Physical Foundation and Technical Implementation* (Springer, 2004).
- [42] M. Ohring, *Materials science of thin films* (Academic Press, 2001).
- [43] J. F. O'Hanlon, *A User's Guide to Vacuum Technology* (Wiley-Interscience, 2003).
- [44] *Magnetic Property Measurement System Manual* (QUANTUM DESIGN INC., 1987).
- [45] A. Barone, *Principles and applications of superconducting quantum interference devices* (World Scientific Publishing Company, 1992).
- [46] M. McElfresh, *Fundamentals of Magnetism and Magnetic Measurements (Application note)* (Quantum Design Inc., 1994).
- [47] B. Fultz, and J. M. Howe, *Transmission Electron Microscopy and Diffractometry of Materials* (Springer, 2007).
- [48] B. T. M. Willis, and C. J. Carlile, *Experimental Neutron Scattering* (Oxford University Press, 2009), p. 352
- [49] J. Als-Nielsen, and D. McMorrow, *Elements of Modern X-ray Physics* (Wiley, 2001).
- [50] X.-L. Zhou, and S.-H. Chen, *Phys. Rep.* **257**, 223 (1995).
- [51] Y. Zhu, *Modern Techniques for Characterizing Magnetic Materials* (Springer, 2005).
- [52] L. G. Parratt, *Phys. Rev.* **95**, 359 (1954).
- [53] J. Daillant, and A. Gibaud, *X-ray and Neutron Reflectivity : Principles and Applications* (Springer, 2008).

- [54] S. S. P. Parkin, V. R. Deline, R. O. Hilleke, and G. P. Felcher, *Phys. Rev. B* **42**, 10583 (1990).
- [55] G. P. Felcher, R. O. Hilleke, R. K. Crawford, J. Haumann, R. Kleb, and G. Ostrowski, *Rev. Sci. Instrum.* **58**, 609 (1987).
- [56] F. Ott, *C.R. Phys.* **8**, 763 (2007).
- [57] S. K. Sinha, E. B. Sirota, S. Garoff, and H. B. Stanley, *Phys. Rev. B* **38**, 2297 (1988).
- [58] R. Pynn, *Phys. Rev. B* **45**, 602 (1992).
- [59] L. Nevot, and P. Croce, *Rev. Phys. Appl.* **15**, 761 (1980).
- [60] D. K. G. de Boer, *Phys. Rev. B* **49**, 5817 (1994).
- [61] <http://neutrons.ornl.gov/facilities/SNS/works.shtml>, (SNS facility neutron sciences in Oak Ridge National Laboratory).
- [62] B. E. Warren, *X-Ray Diffraction* (Dover Publications 1990).
- [63] Philips, *X'Pert-MPD system user guide*.
- [64] B. D. Cullity, and X. R. Stock, *Elements of X-ray diffraction* (Prentice Hall, 2001).
- [65] M. Birkholz, *Thin film analysis by X-ray scattering* (Wiley-VCH, 2006).
- [66] J. U. Thiele, L. Folks, M. F. Toney, and D. K. Weller, *J. Appl. Phys.* **84**, 5686 (1998).
- [67] A.-C. Sun, P. C. Kuo, J.-H. Hsu, H. L. Huang, and J.-M. Sun, *J. Appl. Phys.* **98**, 076109 (2005).
- [68] R. Springell, B. Detlefs, G. H. Lander, R. C. C. Ward, R. A. Cowley, N. Ling, W. Goetze, R. Ahuja, W. Luo, and B. Johansson, *Phys. Rev. B* **78**, 193403 (2008).
- [69] E. R. Dobrovinskaya, L. A. Lytvynov, and V. Pishchik, *Sapphire: Material, Manufacturing, Applications* (Springer, 2009).
- [70] E. E. Fullerton, I. K. Schuller, H. Vanderstraeten, and Y. Bruynseraede, *Phys. Rev. B* **45**, 9292 (1992).
- [71] U. Pietsch, V. Holy, and T. Baumbach, *High-resolution X-ray scattering from thin films to lateral nanostructures* (Springer, 2004), pp. 75.

- [72] B. Ghosh, S. Kumar, A. Poddar, C. Mazumdar, S. Banerjee, V. R. Reddy, and A. Gupta, *J. Appl. Phys.* **108**, 034307 (2010).
- [73] D. Peddis, C. Cannas, G. Piccaluga, E. Agostinelli, and D. Fiorani, *Nanotechnol.* **21**, 125705 (2010).
- [74] K. Kato, K. Sasaki, and Y. Abe, *Jpn. J. Appl. Phys.* **45**, 2731 (2006).
- [75] K. Kato, K. Sasaki, and Y. Abe, *Jpn. J. Appl. Phys.* **45**, 7097 (2006).
- [76] P. A. Stampe, M. Bullock, W. P. Tucker, and J. K. Robin, *J. Phys. D-Appl. Phys.* **32**, 1778 (1999).
- [77] D. McMorrow, R. Cowley, A. Gibaud, R. Ward, and M. Wells, *Appl. Phys. Lett.* **63**, 2195 (1993).
- [78] G. Song, A. Remhof, K. Theis-Bröhl, and H. Zabel, *Phys. Rev. Lett.* **79**, 5062 (1997).
- [79] V. M. Kaganer, R. Köhler, M. Schmidbauer, R. Opitz, and B. Jenichen, *Phys. Rev. B* **55**, 1793 (1997).
- [80] E. Wintersberger, N. Hrauda, D. Kriegner, M. Keplinger, G. Springholz, J. Stangl, G. Bauer, J. Oswald, T. Belytschko, C. Deiter, F. Bertram, and O. H. Seeck, *Appl. Phys. Lett.* **96**, 131905 (2010).
- [81] V. M. Kaganer, and K. K. Sabelfeld, *Phys. Status Solidi A*, 1 (2011).
- [82] V. M. Kaganer, O. Brandt, H. Riechert, and K. K. Sabelfeld, *Phys. Rev. B* **80**, 033306 (2009).
- [83] E. Navarro, M. Multiger, A. R. Yavari, and A. Hernando, *Europhys. Lett.* **35**, 307 (1996).
- [84] A. Hernando, E. Navarro, M. Multigner, A. R. Yavari, D. Fiorani, M. Rosenberg, G. Filoti, and R. Caciuffo, *Phys. Rev. B* **58**, 5181 (1998).
- [85] A. R. Yavari, E. Navarro, H. Mori, H. Yasuda, A. Hernando, and W. J. Botta F, *Philos. Mag. A* **80**, 1779 (2000).
- [86] J. A. De Toro, M. A. López de la Torre, J. M. Riveiro, R. Sáez Puche, A. Gómez-Herrero, and L. C. Otero-Díaz, *Phys. Rev. B* **60**, 12918 (1999).
- [87] G. Suciú, J. C. Toussaint, and J. Voiron, *J. Magn. Magn. Mater.* **240**, 229 (2002).
- [88] J. Moritz, and et al., *Europhys. Lett.* **65**, 123 (2004).
- [89] S. S. Lee, J. G. Choi, S. W. Kim, D. G. Hwang, and J. R. Rhee, *J. Mag.* **10**, 44 (2005).

- [90] N. Zotov, J. Feydt, A. Savan, and A. Ludwig, *J. Appl. Phys.* **100**, 073517 (2006).
- [91] S. Singh, S. Basu, D. Bhattacharya, and A. K. Poswal, *J. Appl. Phys.* **107**, 123903 (2010).